Energy Loss Analysis of Tandem PV Modules under Realistic Operating Conditions

Youri Blom

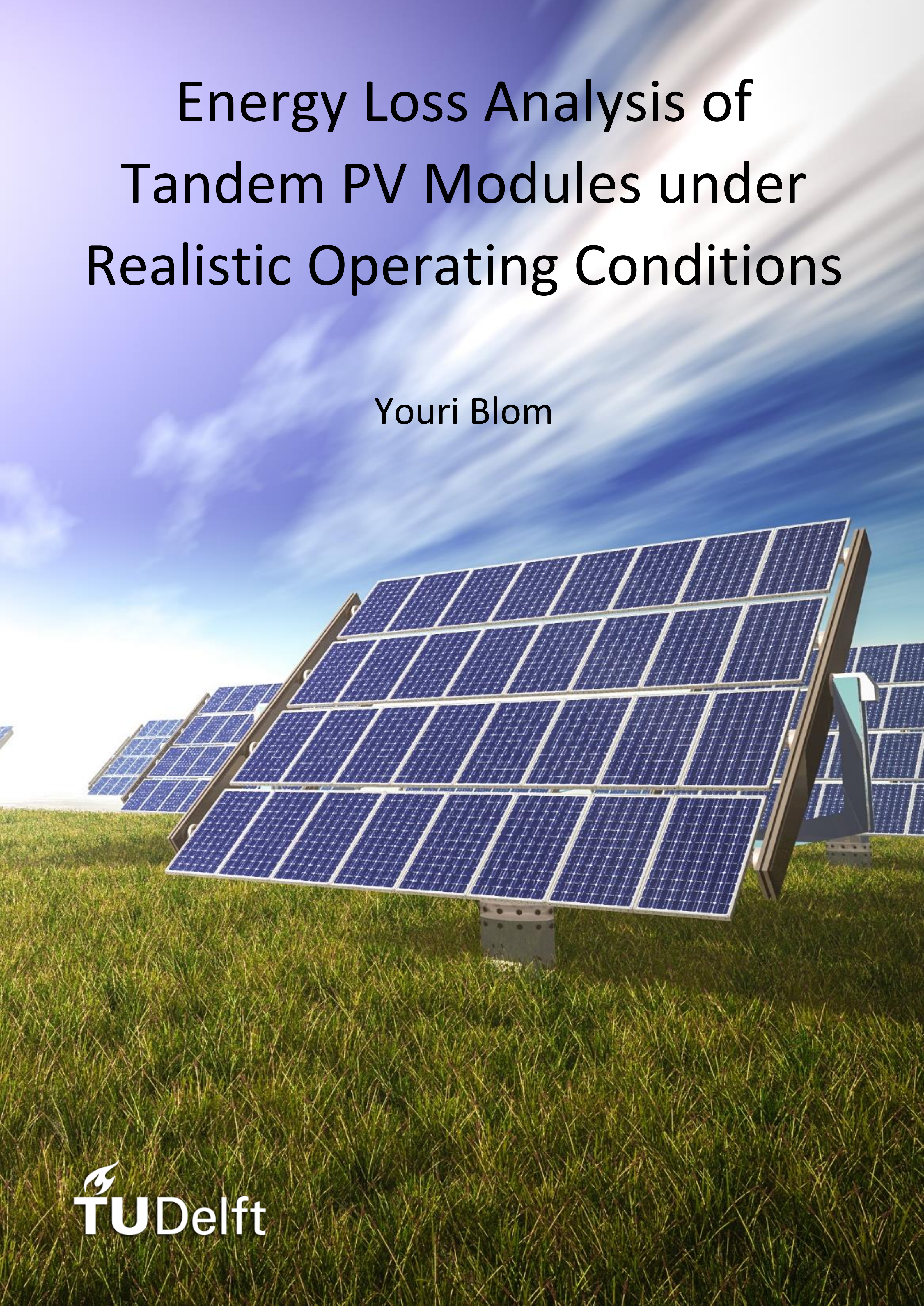

TU Delft

Energy loss analysis of tandem PV modules under realistic operating conditions

by

Youri Blom
4694147

In partial fulfilment of the requirements for the degree of

Master of Science
Electrical Engineering

Supervisors:

Dr. M.R. Vogt
Dr. R. Santbergen

To be defended publicly on Friday August 5, 2022 at 9:00 AM

Thesis committee:
Dr René van Swaaij
Dr. Rudi Santbergen
Dr. Laura Ramirez Elizondo
Dr. Malte Vogt

This thesis is confidential and cannot be made public until February 5, 2023

Delft University Of Technology
Faculty of Electrical Engineering, Mathematics and Computer Science
Electrical Engineering Programme

Abstract

To complete the energy transition, a high efficiency for photovoltaic (PV) modules is desirable to reduce the needed material and surface area (per unit of generated electrical energy). The tandem PV technology has the potential to increase the efficiency of PV modules over 30%. In order to design efficient solar cells, a quantification of the different losses is important. Moreover, research in the losses of PV system has resulted in important insights for PV technology.

This work introduces a comprehensive model for quantifying the different loss mechanisms in a PV system with tandem cells. The loss analysis model will be added to the PVMD Toolbox, which is a software developed at Photovoltaic Materials and Devices group at Delft University of Technology. This software can be used to simulate the energy yield of a PV system at any given location. In the loss analysis model, 17 losses are defined and divided into four categories (fundamental, optical, electrical and system losses).

The developed model will be used to analyse the loss distribution under different operating conditions for four different PV modules. These different modules are a mono-facial crystalline silicon, a bifacial crystalline silicon, a two-terminal perovskite/silicon tandem, and a three-terminal perovskite/silicon tandem module. The design of these modules is based on a >29% efficient perovskite/silicon tandem cell, fabricated by HZB.

The loss distribution of every module is simulated for Standard Test Conditions (STC) and for real word conditions at four geographical locations. Generally, we find that modules operating in tropical high irradiance climates have the lowest efficiency. For all locations, the difference in losses compared to STC follow similar trends. When the two-terminal perovskite/silicon module is simulated at STC, the loss distribution of the fundamental, optical, electrical, and system losses are 54.8%, 8.9%, 8.5%, and 0.1%, leaving a DC module efficiency of 27.7%.

At real-world operating conditions, various differences can be found. The most significant differences are the thermalization, reflection, and recombination losses, which increase with 1.4%, 1.1%, and 0.5% respectively for the two terminal perovskite/silicon tandem module. Furthermore, the simulated two-terminal module has a higher efficiency than the three-terminal modules for all operating conditions due to lower mismatch losses.

Additionally, this study was able to quantify the fill factor gain for two-terminal devices. Due to spectral variations, there can be a mismatch between the absorbed current in the top cell and bottom cell, which can lead to losses. However, this loss is partially compensated by an increase in fill factor. For example, a current mismatch of 7.0% is reduced to a power mismatch loss of 1.2%, due to an increase in fill factor. Therefore, the power mismatch should be used as an indicator for mismatch losses instead of the current mismatch.

Finally, this study simulated different improvements on operating conditions. The results show that solar tracking does not only increase the in-plane irradiance of the PV system, but can also increase the efficiency. For example, dual-axis tracking can increase the efficiency with 1.1%. Also, the gain of active cooling is simulated and quantified. The increase of efficiency when cooling at 20°C compared to a PV system without cooling is around 0.4%, mostly caused by decrease in emission and recombination losses. Furthermore, the optimal perovskite thickness for real world conditions is found, by simulating different thicknesses for the perovskite layer. The results shows that the optimal thickness under STC (575 nm) is also optimal under real-world operating conditions. Finally, the optimal bandgap energies for reducing the fundamental losses are found for tandem cells. For all conditions (including STC), the optimal bandgap energies for the top and bottom cell are 1.73 and 0.94 eV respectively.

Acknowledgement

This thesis is the result of my Master End Project for a duration of eight months. This work is a combination of modelling and theoretical work at the Photovoltaic Material and Devices (PVMD) research group at the Technical University of Delft. I want to thank everyone in this group for the professional environment and guidance during my project.

I especially want to thank my supervisors Dr. Malte Vogt and Dr. Rudi Santbergen. Without them, I would not have been able to fulfil this project. During the eight months, they were always available to share their knowledge, answer my questions, and provide useful feedback to me. Also, they were able to inspire me and keep me motivated throughout the project.

I'm very grateful for the possibilities I received for presenting my work at other places. Thanks to the PVMD group, I was able to visit the "TandemPV International Workshop" in Freiburg and the "Energy Challenge Event" in Delft, where I could present a poster with my work. Furthermore, I received the opportunity to write and submit a paper to "SolarRRL". I learned a lot from all these experiences, and I really want to thank everyone for making this possible.

Furthermore, I want to thank Dr. Carlos Ruiz Tobon for helping with the simulations in ASA software. He provided me the resources and knowledge for this software, allowing me to use this software for my project.

I'm also very grateful to Dr. René van Swaaij and Dr. Laura Ramirez Elizondo for being part of my thesis committee.

And finally, I want to thank my family and friends for being very supportive in the last eight months, but also for the last two years of completing my master degree. They shared the excitement with me on the good days, but also supported me on the moments when things went different than planned. The last two years are definitely worth to remember for a long time, and I want to thank everyone for this!

Contents

Nomenclature **1**

1 Motivation/ background **4**
- 1.1 Introduction to PV . . . 4
- 1.2 Tandem technology . . . 8
- 1.3 The PVMD Toolbox . . . 10
- 1.4 Loss analysis . . . 11
- 1.5 Knowledge gap and objective . . . 12
- 1.6 Thesis outline . . . 13

2 Development of model **14**
- 2.1 Current version Toolbox . . . 14
- 2.2 Order of calculation . . . 16
- 2.3 Fundamental losses . . . 18
- 2.4 Optical losses . . . 22
- 2.5 Electrical losses . . . 24
- 2.6 System losses . . . 27
- 2.7 Validation of implementation . . . 28
- 2.8 Numerical deviations . . . 32
- 2.9 Conclusion . . . 34

3 Loss analysis STC **35**
- 3.1 The design of the cells . . . 35
- 3.2 The design of the modules . . . 43
- 3.3 Results and comparison . . . 48
- 3.4 Conclusion . . . 53

4 Loss analysis outdoors **54**
- 4.1 The irradiance model . . . 54
- 4.2 The different climates . . . 55
- 4.3 Results mono-facial module . . . 57
- 4.4 Results bifacial module . . . 59
- 4.5 Results 2T tandem module . . . 60
- 4.6 Results 3T tandem module . . . 63
- 4.7 Comparison of modules . . . 64
- 4.8 Conclusion . . . 67

5 Optimisations on system **68**
- 5.1 Solar tracking . . . 68
- 5.2 Fixing the temperature . . . 72
- 5.3 Thickness perovskite layer . . . 74
- 5.4 Different bandgap energies . . . 76
- 5.5 Conclusion . . . 78

6 Conclusion **80**
- 6.1 Conclusion . . . 80
- 6.2 Recommendations . . . 82

A Implementation **85**
A.1 Derivation of the optimal voltage . . . 85
A.2 Implementation tandem . . . 86
A.3 Results different methods . . . 89
A.4 Difference spectra . . . 90

B Appendix losses STC **92**
B.1 The comprehensive model for the reverse connection . . . 92
B.2 Parameter dependence . . . 92
B.3 Optical difference 3T cell . . . 95
B.4 Results reverse connection . . . 96

C Appendix outdoor losses **97**
C.1 Assuming equal irradiance for every cell . . . 97
C.2 Irradiance model bifacial . . . 97
C.3 Monofacial module detailed . . . 101
C.4 Bifacial module detailed . . . 102
C.5 2T tandem module detailed . . . 104
C.6 3T tandem module detailed . . . 105
C.7 The module temperature at different locations . . . 108
C.8 Optimal voltage outdoors . . . 109

D Appendix optimisations **110**
D.1 ASA simulations . . . 110
D.2 The results for tracking . . . 112
D.3 The results for active cooling . . . 113
D.4 The results for thickness . . . 115

Nomenclature

Symbols

AOI Angle of Incidence.

A_{mod} The area of the module [m^2].

EQE external quantum efficiency [%].

ERE external radiative efficiency [%].

E_g bandgap energy [eV].

FF fill factor [-].

I_0 saturation current [A].

I_{in} Spectral irradiance per wavelength of the incoming spectrum [W·m^{-2} · nm^{-1}].

I_{mpp} maximum power point current [V].

I_{ph} photo generated current [A].

I_{sc} short circuit current [A].

P_{AC} AC output power [W].

P_{Carnot} Carnot limit losses [W].

P_{NRRI} current losses due to non-radiative recombination [W].

P_{NRRV} voltage losses due to non-radiative recombination [W].

$P_{abs,par}$ parasitic absorption losses [W].

P_{angle} angle mismatch losses [W].

P_{below} losses due to below bandgap non absorption [W].

P_{cable} cable losses [W].

$P_{cell-spacing}$ losses due to cell spacing [W].

$P_{electrical}$ electrical losses [W].

$P_{emission}$ emission losses [W].

P_{fund} fundamental losses [W].

$P_{intercon}$ losses due to cell interconnection [W].

$P_{inverter}$ inverter losses [W].

$P_{metallization}$ losses due to metallization [W].

$P_{mismatch}$ mismatch losses [W].

P_{mpp} maximum power [W].

$P_{optical}$ optical losses [W].

$P_{ref,trans}$ reflection and transmission losses [W].

P_{series} Ohmic losses due to series resistance [W].

P_{shunt} Ohmic losses due to shunt resistance [W].

P_{system} system losses [W].

P_{term} thermalization losses [W].

R_s series resistance [Ω].

R_{sh} shunt resistance [Ω].

SF shading factor [-].

T_A ambient temperature [°C].

V_{Carnot} Carnot voltage difference [V].

V_{angle} angle mismatch voltage difference [V].

V_{mpp} maximum power point voltage [V].

V_{oc} open circuit voltage [V].

Ω Solid angle [sr].

λ_g wavelength corresponding to the bandgap energy [m].

μ chemical potential [V].

ϕ_E flux density per energy [J^{-1} · m^{-2} · s^{-1}].

ϕ_λ flux density per wavelength [m^{-2} · nm^{-1} · s^{-1}].

ϕ_{in} flux density per wavelength of the incoming spectrum [m^{-2} · nm^{-1} · s^{-1}].

n ideality factor [-].

p_{mpp} maximum power density [W·m^{-2}].

2T two terminal.

3T three terminal.

4T four terminal.

A

AM air mass.

ASA Advanced Semiconductor Analysis.

C

CLEM calibrated lumped element method.

G

GHI Global Horizontal Irradiance [kWh·m^{-2}].

K

KGPV Köppen-Geiger-Photovoltaic.

N

NRR non-radiative recombination.

P

PV photovoltaic.

PVMD Photovoltaic Materials and Devices.

S

SQ Shockley-Quiesser.

STC standard test conditions.

W

WS wind speed [m·s^{-1}].

1. Motivation and background

Currently, humanity is making a transition from fuel energy to renewable energy. The reason for this is the goal of the European Union to become climate neutral in 2050, which is stated in the European Green Deal [1] and the Paris Agreement [2]. One of the renewable energy sources is photovoltaic (PV) technology, which is growing rapidly. The installed PV capacity worldwide has increased from around 73 GWp in 2011 to 940 GWp in 2021 [3].

To achieve these goals, it is important for PV modules to become as efficient as possible to reduce the number of needed PV systems. A loss analysis can help to make solar cells more efficient, as it provides an overview of the different losses that are present. A quantification of the different loss mechanisms is very important for the development of PV technology [4]. Because it is desirable to have solar cells with a high efficiency, it is useful to know which factors affect this efficiency. A loss analysis can help to understand and to quantify these effects for different materials and different types of solar cells [5]. Furthermore, research in loss analysis has resulted in important insights for the design of a solar cell [6].

Another aspect that needs to be considered, is that most solar cells are tested under standard test conditions (STC). This is important, such that the performance of different solar cells can be compared with each other. However, it is also crucial to optimise the performance under various climate conditions because different conditions affect the performance of solar cells [7].

This chapter discusses the most important topics that are analysed during the literature study of this project. Also, this chapter presents background knowledge regarding the loss analysis of tandem PV modules. First, a brief introduction to photovoltaic (PV) technology will be given, including the IV-curve and the five-parameter model. After this, the tandem technology is explained. This technology can be used to increase the efficiency of a solar cell. Then, an analysis on the PVMD Toolbox will be given. This toolbox can be used to simulate certain aspects of a PV system. This is followed by an overview of the different losses that are considered. Finally, the knowledge gap that this project tries to overcome is explained and the goals of this thesis are presented.

1.1 Introduction to photovoltaic technology

PV technology creates electricity from light. Light, which normally comes from the sun, is absorbed by a solar cell, and can be used to generate electrical energy. This section discusses several aspects to give a short introduction about PV technology.

1.1.1 Energy from the sun

The most important source of energy for the earth is the sun [8]. Every day 60,000 EJ is radiated towards the earth and around 50% of this energy actually reaches the surface of the earth. In comparison, the total energy consumption per year is around 550 EJ for the last decade [9, 10]. This means that approximately 20,000 times more energy reached the earth than is consumed by humankind.

The energy from the sun comes in the form of light, where light consists of photons. The energy of a single photon can be calculated by using the Planck equation, written as

$$E_{photon} = \frac{h \cdot c}{\lambda}, \tag{1.1}$$

where h is the plank constant, c is the speed of light, and λ is the wavelength of the photon. Light can be characterized with its total power, its wavelength spectrum, its position, and the direction of travel. The AM1.5 spectrum is defined by the International IEC and is based on the irradiance received on a cloudless day on the earth's surface [11, 12]. The AM1.5 spectrum is shown in Figure 1.1.

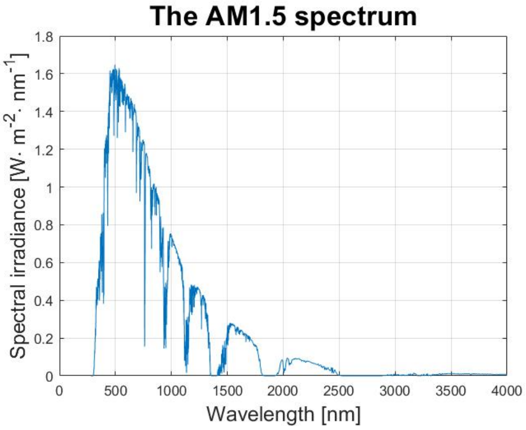

Figure 1.1: The AM1.5 spectrum as defined by the International IEC. It shows the amount of energy that is radiated on earth's surface for every wavelength.

1.1.2 Working principle of a solar cell

A solar cell converts the energy of a photon into electricity by creating an electron-hole pair, which is the called the photovoltaic effect [10]. A solar cell usually consists of a semiconductor material. In a semiconductor, there are two energy bands in which electrons can be located. These two bands are the conduction band and the valence band [13]. The energy difference between these two bands is called the bandgap energy (E_g), as shown in Figure 1.2a. A photon can transfer its energy to an electron in the valence band such that it can move to the conduction band, as shown in Figure 1.2b.

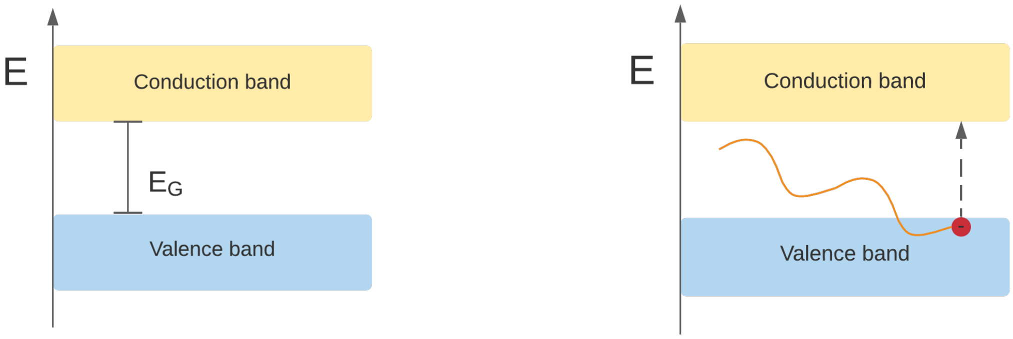

(a) The different energy bands in a semiconductor. The difference between the conduction and valance band is the bandgap energy.

(b) If the energy of the photon has more energy than the bandgap energy, its energy is transferred to the electron. This causes the electron to move to the conduction band.

Figure 1.2: The energy bands in a semiconductor.

The amount of energy that can be transferred from a photon to the solar cell is dependent on the material. Photons that have an energy larger than the bandgap energy of the solar cell are able to generate an electron-hole pair, thus creating electricity. The difference between the energy of the photon and the bandgap energy cannot be used for normal solar cells and is considered as a loss. This loss is called the thermalization loss [14]. All the photons that have less energy than the bandgap energy cannot generate an electron-hole pair and are therefore also considered as losses. This loss is called the below bandgap loss. These losses, together with radiative recombination, give an upper limit for the efficiency for a single junction solar cell. This limit is 30% for a general single junction solar cell, famously known as the Shockley-Quiesser limit [15], and 29.4% for crystalline silicon solar cells [16].

1.1.3 The IV-curve of a solar cell

If the two poles of a solar cell are connected, the absorbed photons can create a current. This current will depend on the voltage over the solar cell. If the current from the solar cell is measured for different voltages, an IV (current/voltage) curve can be made. By multiplying the voltage with the current for every point, the output power of each voltage can be calculated, thus creating a PV (power/voltage) curve. A typical IV curve and PV curve are shown in Figure 1.3.

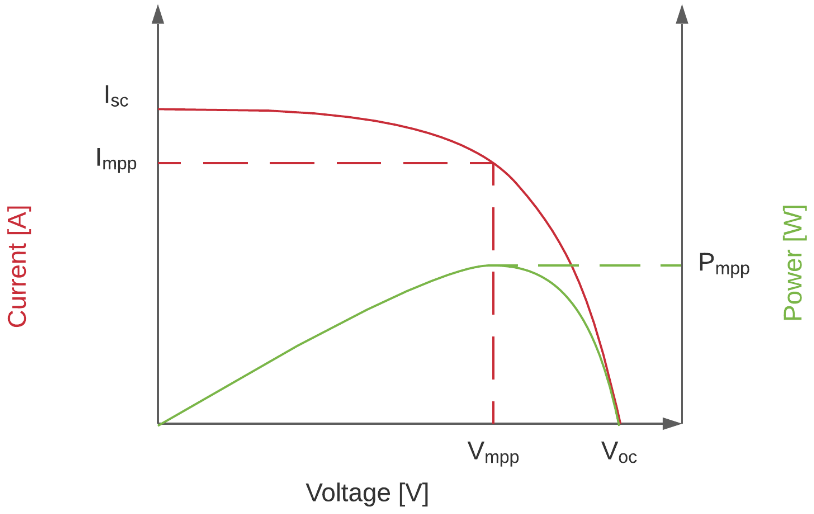

Figure 1.3: A typical IV curve and P-V curve of a solar cell.

The IV curve of a solar cell is characterised by the following parameters:

- The short circuit current (I_{sc}): This is the current if there is no voltage over the solar cell, thus creating a short circuit.
- The open circuit voltage (V_{oc}): This is the applied voltage such that there is no output current.
- The maximum power (P_{mpp}): This is the maximum power that can be obtained from the solar cell.

- The maximum power point voltage (V_{mpp}): This is the voltage at which maximum power is obtained.
- The maximum power point current (I_{mpp}): This is the current at which maximum power is obtained.
- The fill factor (FF): The parameter is the ratio of the maximum power and the product of I_{sc} and V_{oc}, so $FF = \frac{I_{mpp} \cdot V_{mpp}}{I_{sc} \cdot V_{oc}}$. This value is ideally as close to 1 as possible.

1.1.4 The five-parameter model

To model the electrical behaviour of a solar cell, the five-parameter model can be used [14, 17–19]. This model consists of four components and 5 unknown parameters, as shown in Figure 1.4. The model consists of a current source with current I_{ph}, a diode with saturation current I_0 and ideality factor n, and two resistors R_s and R_p.

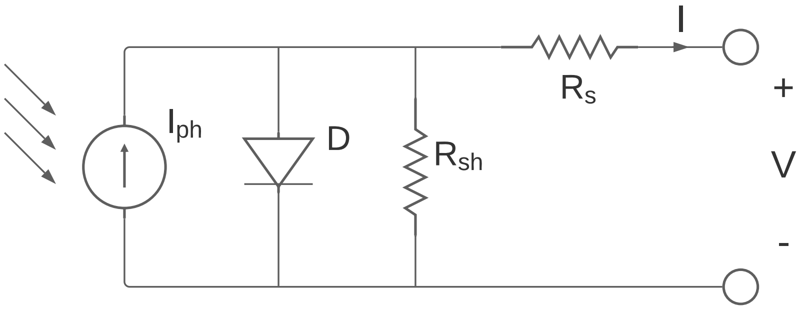

Figure 1.4: The five-parameter model, which can be used to model the electrical behaviour of a solar cell. It consists of a current source, a diode, and two resistors.

The five unknown parameters of the model are:

- The photo generated current (I_{ph}): This parameter is the value of the current source and expresses the amount of generated electron-hole pairs in a solar cell.
- The saturation current (I_0): This parameter is a characteristic of the diode, and it accounts for the recombination losses in the solar cell [20].
- The ideality factor (n): This parameter is also a characteristic of the diode, and it indicates which recombination mechanism is the most dominant [21].
- The series resistance (R_s): This parameter represents the ohmic losses in the bulk and the contacts of a solar cell [22]. The value of R_s would be 0 for an ideal solar cell.
- The shunt resistance (R_{sh}): This parameter represents the ohmic losses, caused by leakage currents [23]. The value of R_{sh} would be ∞ for an ideal solar cell.

By applying the laws of circuit theory, the output current can be expressed with Equation (1.2)

$$I = I_{ph} - I_0 \cdot \left(e^{\left(\frac{V + I \cdot R}{n \cdot V_t} \right)} - 1 \right) - \frac{V + I \cdot R_s}{R_{sh}} \tag{1.2}$$

Equation (1.2) is an implicit expression and cannot be solved analytically without using the Lambert W function [24]. This is explained in Section 2.1.

1.2 Tandem technology

A tandem solar cell is one of the technologies, which aims to overcome the Shockley-Quiesser limit [15]. In this technology, two solar cells of different material are combined to increase the efficiency.

1.2.1 The principle of tandem solar cells

As explained in Section 1.1, the efficiency of a solar cell is mostly limited due to thermalization losses and below bandgap losses. These losses can be reduced by using the so-called tandem technology [25]. In a tandem solar cell, two different materials with a different bandgap energy are placed on top of each other, such that each layer can absorb a different spectrum of light. The material with the highest bandgap is placed on top to absorb the photons with a high energy. The lower bandgap material is placed on the bottom to absorb photons with a lower energy, which cannot be absorbed by the top layer.

The efficiency of a tandem solar cell is higher compared to a normal solar cell, because high energy photons can transfer more of their energy into electricity. This is shown in Figure 1.5, where the usable energy in the wavelength spectrum is compared for the solar cell and the tandem solar cell.

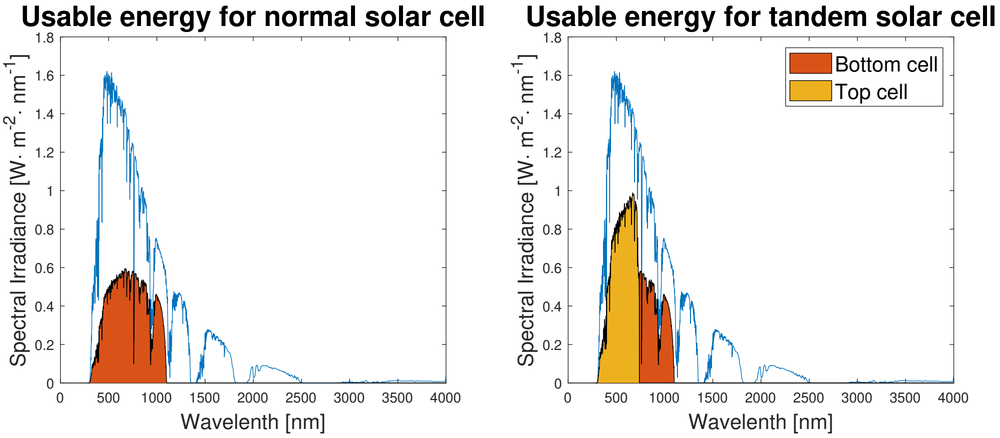

Figure 1.5: The usable energy for a normal solar cell and for a tandem solar cell. Because of the multiple bandgap energies, more energy is usable. In this figure a bandgap energy of 1.12 eV is used for the bottom layer and a bandgap energy of 1.68 eV is used for the top layer.

1.2.2 Different structures

There are multiple methods to connect a tandem solar cell. The solar cell can be connected in a two terminal (2T), three terminal (3T), or in a four terminal (4T) configuration [26–29]. All the different configurations are shown in Figure 1.6.

In the 2T configuration, the current flowing through the solar cells must be the same for both layers. Therefore, the currents between the top layer and the bottom layer needs to be matched. This can be done by varying the thickness of the top layer [27]. The absorption of the top layer depends on its thickness. Since the photons that are not absorbed by the top layer will be transmitted to

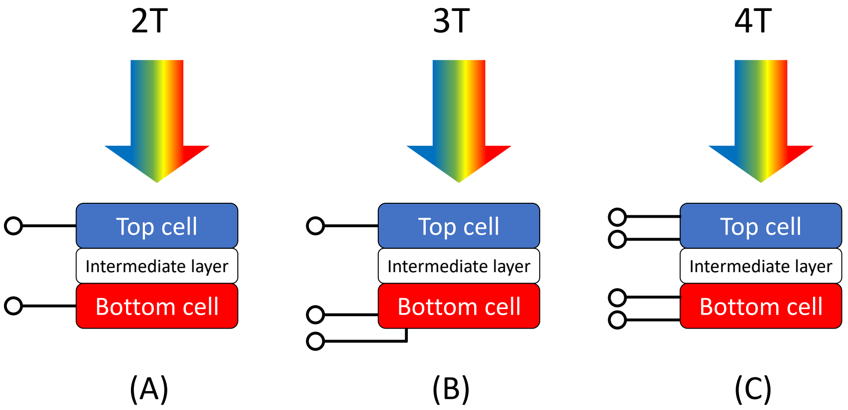

Figure 1.6: The different configurations for a tandem solar cell. In (A) the 2T configuration is shown, in (B) the 3T configuration is shown, and in (C) the 4T configuration is shown.

the bottom layer, the current density of the bottom layer will be affected by the thickness of the top layer. Other methods that can be used for current matching are [27]:

- Texturing can be added in the intermediate layer to create scattering in the bottom cell. Due to light scattering, more light will be absorbed in the bottom cell, thus creating a higher current.
- The bandgap energy in one of the two layers can be changed. The bandgap energy of a material affects the absorption of the solar cell, which therefore also affects the current.

Another challenge in the 2T configuration is to reduce the recombination losses at the intermediate layer [28]. Furthermore, the intermediate layer should also have a low electrical resistance and should not absorb light in the near infra-red region.

3T tandem cells are relatively new and are designed to use the advantages of both 2T and 3T tandem cells [30]. A third contact can be placed at the intermediate layer or at the back (more deeply discussed in Section 3.1), such that the top and bottom cells can operate independently. Therefore, current matching is not needed.

In the 4T configuration, the current of the two solar cells do not have to be matched. However, the production costs of both the 4T configurations are high compared to the 2T configuration [28, 29]. Therefore, these configurations are not suitable for large scale production, and will therefore not be considered in this project.

1.2.3 Perovskite/ silicon tandem solar cells

A combination of perovskite and silicon has become a promising structure for tandem solar cells [28, 31–35]. Several advantages of perovskite are that it is low cost, the bandgap can be varied, the fabrication process is not difficult, and it has a high absorption coefficient. Also, perovskite as a single junction solar cell has measured an efficiency of more than 25% [36] and the efficiency limit for a single junction perovskite solar cell is predicted at 30.88% [37].

Perovskite has a specific crystal structure in the form of ABX_3 [32, 35]. In this structure, A is a larger cation (meaning that it is positively charged), B is a smaller cation, and X is an anion (meaning that it is negatively charged). In PV applications, organic-inorganic perovskites are used, which means that A is an organic material, B is normally lead or tin, and X is a halogen [11].

There are still some challenges regarding perovskite [38]. To tune the optical properties, the structure of perovskite has to be modified, which affects the long-term stability of the solar cell. Also, perovskites with certain cations have been shown to degrade under exposure of moisture and heat.

Silicon is the most used materials for PV technology [39]. One important reason for this is that the bandgap of silicon at room temperature is 1.12 eV [13], which is close to the optimal bandgap for the SQ limit. Another reason is the fact that silicon is one of the most abundant materials on earth [40], which means that silicon is suitable for large scale production.

In a perovskite/silicon tandem solar cell, perovskite is used as top cell and silicon is used as bottom solar cell. A tandem solar cell with this combination has already led to cell efficiencies over 30% [36]

1.3 The PVMD Toolbox

This project will be implemented into the PVMD Toolbox [41]. This toolbox is created at the TU Delft in the Photovoltaic Materials and Devices (PVMD) research group to simulate the energy yield of a PV system. The simulation process is divided into different models, which are the absorption model, the ray tracing module, the semiconductor model, the irradiance model, the thermal model, the electrical model, and the inverter model [41]. An overview of all different models and the interaction between the models is given in Figure 1.7. A detailed explanation of each of these models is given in Section 2.1.

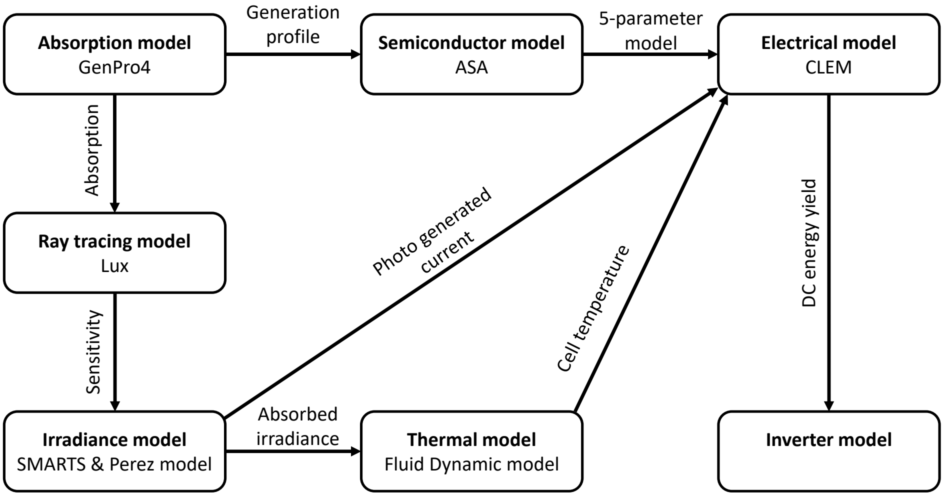

Figure 1.7: An overview of the different models in the toolbox. Also, the software used for different models is represented.

1.4 Loss analysis

For every PV system, there is a difference in the generated electrical energy and the received in-plane irradiance. A loss analysis provides an overview which factors cause these differences. In this project, 17 different losses are considered, which are divided over four categories. This section introduces the four categories. A detailed explanation for each individual loss can be found in Chapter 2.

1.4.1 Fundamental losses

The first losses that will be considered are the fundamental losses. These losses are called 'fundamental', because they cannot be prevented or reduced without fundamentally changing the PV system or the operating conditions. These losses will always happen when electricity is generated at a solar cell, since it is part of the working principle of photovoltaic technology. The fundamental losses are the losses used for calculating the upper limit of the efficiency, such as the SQ limit [15] or the upper limit of a tandem cell calculated by De Vos [25].

1.4.2 Optical losses

The second category are the optical losses. This category includes all losses that occur due to the working principle of light absorption. In total four optical losses are included, from which two are caused by non-active area. This is area that cannot be used for the generation of electricity. The other two losses of this category are losses occurring due to the behaviour of light, such as reflection and parasitic absorption.

1.4.3 Electrical losses

After photons have generated an electron-hole pair, the electrons and holes need to be collected such that an electrical current can flow. During this process, two different losses are present that reduce the efficiency of the solar cell, which are recombination losses and Ohmic losses. The losses of this category can be calculated by using the five-parameter-model, which is discussed in Section 1.1.

1.4.4 Module/ system losses

The last category are the module/ system losses. This are all losses that occur at module or system level. These losses can be grouped as DC system losses and AC system losses. The DC system losses arise because different cells are connected together, which introduces non-idealities. The AC system losses happen during the conversion from DC to AC, and the transportation of current through the cables.

1.4.5 Difference real-world operating conditions and STC

When solar cells are installed at operating conditions, its performance is in general different than at STC [7]. The two main factors which cause this difference are a difference in temperature and a difference in irradiation. Both of these factors can be seen as indirect losses, because they affect other losses.

The temperature

If the solar cell operates at a different temperature than the STC temperature, the characteristics of the IV curve will change [42–44]. An increase in temperature typically results in a decrease in efficiency.

The irradiance

At STC, the irradiance is defined at 1000 W/m^2. However, the irradiance is in general different when operating at outdoors conditions. Therefore, there will be a difference in performance and energy losses. One aspect that influences the level of irradiance is the angle of incidence [45], which is the angle between the module and the position of the sun.

1.5 Knowledge gap and thesis objective

As any other scientific report, this project aims at increasing the scientific knowledge and overcoming certain knowledge gaps. This section discusses the knowledge gaps this project wants to overcome and the objectives of this thesis.

1.5.1 Knowledge gap

The first knowledge gap this project aims to overcome is to extend the PVMD Toolbox. As described in [41], the PVMD Toolbox is developed at the TU Delft to model the energy yield of PV systems. However, this toolbox does not include a loss analysis model. This project will implement a loss analysis model to the toolbox, such that the loss distribution for different solar cells can be quantified.

As discussed in Section 1.2 the combination of perovskite and silicon in a tandem solar cell is promising. Because tandem cells of silicon and perovskite are relatively new, the potential of this technology is not fully known yet. There is some literature on the loss analysis of a single junction solar [4, 6, 14, 46–49] and there is literature on an optical analysis of a perovskite/silicon tandem solar cell [27, 33]. However, no literature has been found for a complete loss analysis for a perovskite/silicon tandem solar cell. This thesis can give insight into which factors affect the efficiency of a solar cell and what the most important losses are.

Also, since the combination of perovskite and silicon is not fully developed yet, no large-scale area PV module with perovskite/silicone technology has been designed [50]. Simulations of the energy yield of a PV system with perovskite/silicon solar cells under operating conditions are already done[26, 31, 51], but a loss analysis can help to understand the differences between STC and operating conditions for this technology.

Finally, the developed model can be used to analyse optimisations or improvements that can reduce the reduce the losses. By analysing and comparing the loss distributions, it can be seen how a certain improvement increases the efficiency and the effect can be quantified. Since no literature has been found for a complete loss analysis on the perovskite/silicon solar cell, there is also no literature found on reducing these different losses. This thesis can give an understanding how different improvements can help to increase the energy yield.

1.5.2 Thesis objective

This project is a continuation of previous work done on the PVMD Toolbox by students from the TU Delft [51, 52]. The main goal of this thesis is:

Use the energy loss distribution model to analyse improvements for perovskite/silicon tandem systems under realistic operating conditions.

To achieve this goal, the following sub-goals are defined:

Sub-goal 1: Development and implementation of a loss analysis model

The current version of the PVMD Toolbox provides an energy yield for a PV system at a certain location. The next step for the Toolbox is to have a quantification of the different losses in a PV system. The different losses discussed in Section 1.4 can each be calculated with methods described in literature. All these calculations combined provide an overview and quantification of the different losses that are present.

Sub-goal 2: Loss analysis of a perovskite/silicon tandem module at STC

As described in the beginning of this section, no literature has been found on a complete loss analysis for a perovskite/silicon tandem module. To compare the loss distribution with different solar cells, the loss distribution needs to be calculated at standard test conditions. This thesis aims to provide an overview of the different losses that are present and quantifies these losses at STC.

Sub-goal 3: Loss analysis of a perovskite/silicon tandem module at real-world operating conditions

As stated before, the performance of a PV system can change when operating outdoors. Therefore, it is also essential to look at the loss analysis of a solar cell at normal operating conditions. This thesis also aims at quantifying the different losses at operating conditions and comparing different locations with each other.

Sub-goal 4: Simulation of optimisations and improvements to reduce energy losses

The last objective of this thesis is to simulate possible optimisations and improvements. The loss analysis can be used as an indication where improvements can be the most beneficial. These different improvements can be simulated to see the effect and it can be used to optimise the design of the solar cell.

1.6 Thesis outline

This report consists in total of six chapters. Chapter 2 to 5 each cover a different sub-goal. Chapter 2 discusses the implementation of the different losses, which are discussed in Section 1.4. This is the first sub-goal discussed before. In Chapter 3, the loss distributions of different PV modules are analysed under STC, which covers sub-goal 2. Chapter 4 analyses the energy loss of different solar cell under realistic conditions, which is sub-goal 3. In Chapter 5, sub-goal 4 is covered. This chapter will show improvements that can increase the efficiency. Chapter 6 will present the conclusion of this project and will discuss recommendations for future study.

2. Development of a comprehensive loss analysis for the PVMD Toolbox

As discussed in Chapter 1, this project is an extension of the PVMD Toolbox. Before the results of the loss analysis can be studied, the implementation needs to be discussed, as this determines how the losses are defined. In this chapter the first sub-goal mentioned in Section 1.5 is covered.

This chapter first discusses the current state of the PVMD Toolbox. This is done to provide a clear overview of what this project adds to the Toolbox. Then, the implementation of the loss analysis is described, which is the part that is added to the Toolbox. First, the order of the calculation and the motivation for this order is discussed. After this, the implementations of the four categories, as discussed in Section 1.4, are discussed separately. Finally, a mathematical and physical validation of the implementation is given in which the results are compared to fundamental limits of literature.

2.1 The current version of the PVMD Toolbox

The PVMD Toolbox is briefly introduced in Chapter 1.3. It consists of several models that each simulate a different aspect of a PV system. An overview of these models is shown in Figure 1.7. For each of the models, a short explanation of its working principle is given.

2.1.1 The absorption model

The first model calculates the optical properties of the PV module. These properties are simulated using the GenPro4 software [53]. This software calculates the total reflectance, transmittance, and the absorptance in each layer, based on the thickness (d) and refractive index ($n(\lambda) + i \cdot k(\lambda)$) of each layer. This is done by using the net radiation method [54]. In this method, four different fluxes are defined for every layer, where each flux represents a photon path. All these fluxes can be solved with a set of linear equations, which allows GenPro4 to calculate the different outputs. Furthermore, GenPro4 is able to simulate flat interfaces as well as textured interfaces.

2.1.2 The ray tracing model

To simulate the mounting conditions of a solar cell, a sensitivity map is generated for all solid angles. This is calculated by using the software LUX [41], which has implemented a forward Monte-Carlo ray tracing method. This allows for shading and albedo effects. The sensitivity of a certain angle is defined as number of absorbed rays by the solar cell divided by the incoming rays [55].

2.1.3 The semiconductor model

To simulate the IV curve of the solar cell, the simulator Advanced Semiconductor Analysis (ASA) is used [56]. This simulator solves the Poisson equation and two continuity equations for electrons and holes in one dimension under different conditions. The input of the software are properties of each layer, which are the free electron concentration, the hole concentration, electrostatic potential, and the depth resolved generation profile.

The toolbox uses ASA to calculate the IV curves of a cell at different temperatures and different irradiances. This is done by using the five-parameter model, as discussed in Section 1.1. This creates a calibrated lumped element method (CLEM) with temperature and irradiance dependent parameters.

2.1.4 The irradiance model

The toolbox uses a model to simulate the irradiance from each solid angle at each moment of time. This model is based on the Perez model [57], which models the distribution pattern of the sky luminance. After this, the model uses SMARTS [58] to obtain the spectral composition of the irradiance or the photon flux. Combined with the sensitivity calculation of the optical model, the absorbed irradiance and the photo generated current in the solar cell can be calculated.

2.1.5 Thermal model

Since the performance of the solar cell dependents on its temperature, it is important to model the temperature accurately. The PVMD toolbox does this by using the fluid-dynamic model [11, 59]. An advantage of this model is that it only uses non-empirical parameters [41], which makes the Toolbox also useful for solar cells that are not tested yet. This model considers the following heat flows:

- Heat absorbed from the sun.
- Convective heat exchange.
- Radiative heat exchange between the module and the sky.
- Radiative heat exchange between the module and the ground.

These heat flows can be combined into a heat transfer balance [11]. If some assumptions are made a single equation for the module temperature can be made, written as

$$T_M = \frac{\alpha G + h_c T_a + h_{r,sky} \cdot T_{sky} + h_{r,gr} T_{gr}}{h_c + h_{r,sky} + h_{r,gr}}, \tag{2.1}$$

where T_M, T_a, T_{sky} and T_{gr} are the temperatures of the module, the ambient, the sky, and the ground respectively. αG represents the absorbed heat, and h_c is the convective heat coefficient. Furthermore, $h_{r,sky}$, and $h_{r,gr}$ are the radiative coefficients of the sky and ground respectively.

Because the values for $h_{r,sky}$ and $h_{r,sky}$ depend on T_m, this equation has to be repeated iteratively until the value for T_M becomes stable.

2.1.6 Electrical model

To calculate the generated power, the electrical model is used. This model takes as input the photo generated current [A], the cell temperature, and the parameters of the five-parameter model. The IV curve is calculated by using the Lambert W function [24, 60, 61]. The Lambert W function is a solution to the equation

$$x \cdot e^x = z, \tag{2.2}$$

such that $x = W(z)$. The Lambert W function can be used to have an explicit solution for the current of the solar cell in terms of the voltage. This expression can be written as [24]

$$I(V) = \frac{R_{sh} \cdot (I_{ph} + I_o)}{R_{sh} + R_s} - \frac{V}{R_{sh} + R_s} - \frac{n \cdot V_{th}}{R_s} \cdot W\left(\frac{R_{sh} \cdot I_0 \cdot R_s}{(R_{sh} + R_s)\, n \cdot V_{th}} \cdot e^{\frac{R_{sh} \cdot \left(R_s \cdot I_{ph} + R_s \cdot I_0 - V\right)}{(R_{sh} + R_s) n \cdot V_{th}}} \right). \tag{2.3}$$

To reduce the number of calculations, the operating conditions are discretized into temperature steps of 0.3 K and I_{ph} steps of 0.01 A/m^2. This discretization can reduce the number of calculated IV curves [41]. If certain operating conditions appear at multiple moments in time, they are only simulated once for all moments.

2.1.7 Inverter model

The last model that is discussed in this section is the inverter model, which simulates the conversion from DC power to AC power. The inputs of this model are the number of PV modules in series and parallel, the DC and AC cables, and the inverter properties. The PVMD Toolbox can simulate central inverters, string inverters, micro inverters, and power optimizers. To simulate the three different inverters, the SNL model is used [18, 62], and for the power optimizer a model from the TU Delft is used [41].

2.2 Order of calculation

Before the actual calculations of the different loss components can be done, it is important to determine the order in which the losses are calculated. The reason for this, is because the order affects the equations that need to be used.

This also means that multiple power distributions over the different losses are possible. As an example, it can be argued that reflection losses should be calculated before the thermalization losses, because the reflected photons are not absorbed and will therefore not lose energy due to thermalization. Changing the order of thermalization losses and reflection losses, would therefore change the loss distribution.

The order that is used for this project is shown below and shown in Figure 2.1. All the considered losses and the categories are described in Section 1.4. First, the fundamental losses are calculated, followed by the optical, electrical and system losses.

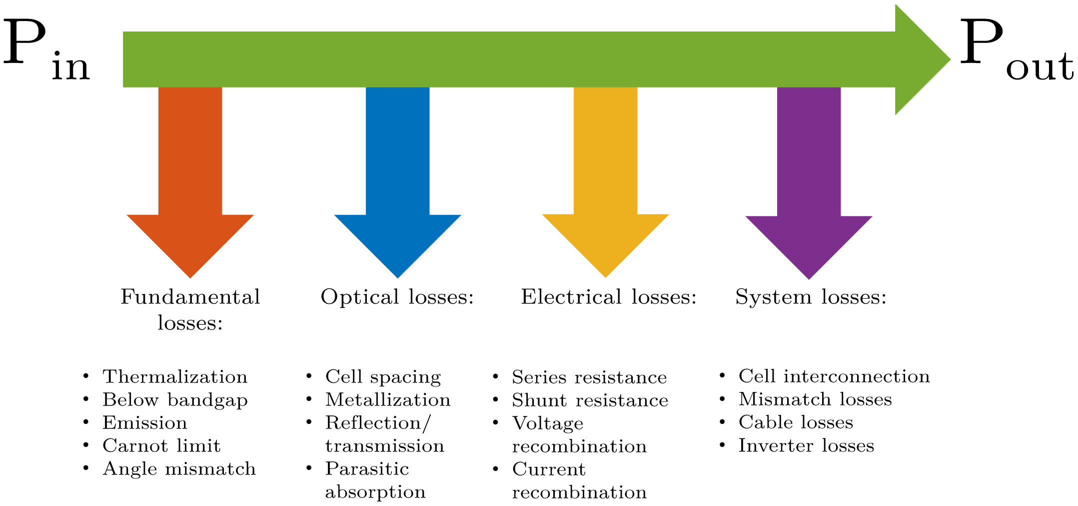

Figure 2.1: The order in which the different losses are calculated.

The main reason for calculating the fundamental losses first, is because these losses are, as the name states, fundamental [63, 64]. This means that these losses cannot be prevented without fundamentally changing the solar cell. Therefore, calculating these losses first indicates how much energy is fundamentally lost and gives a clear upper limit for the design of the solar cell.

Another reason for this order, is that the results can give more useful information. As explained in Chapter 1, a loss analysis can be used to improve the design of a solar cell, based on the loss distribution. By calculating the fundamental losses first, a better estimate can be made of how much energy can be gained by improving a certain aspect of the solar cell. As the fundamental losses are taken out of the other losses, this does not have to be taken into account when estimating a certain gain. This makes the loss analysis more useful because it can more easily be seen which improvements can have the largest gain.

The motivation for the remaining order of the optical losses, electrical losses, and system losses is that it can be seen as the order of which the energy is transferred into AC electricity. First, photons need to be absorbed by the solar cell, which introduces optical losses. After this, photons need to be transferred into electricity. In this process, electrical losses occur. Finally, the created electricity at cell level is transferred to AC electricity at module level, in which the system losses occur.

The order of the losses within a category are chosen in the order of which they occur. Whenever there is not a clear order of occurring, either the losses are not dependent on each other, or the most logical order is chosen. A complete list of all losses is shown below.

1. Fundamental losses (P_{fund})
    (a) Thermalization losses (P_{term})
    (b) Losses due to below bandgap non absorption (P_{below})
    (c) Emission losses ($P_{emission}$)
    (d) Carnot limit losses (P_{Carnot})
    (e) Angle mismatch losses (P_{angle})
2. Optical losses ($P_{optical}$)
    (a) Losses due to cell spacing ($P_{cell-spacing}$)
    (b) Losses due to metallization ($P_{metallization}$)
    (c) Reflection and transmission losses ($P_{ref,trans}$)
    (d) Parasitic absorption losses ($P_{abs,par}$)
3. Electrical losses ($P_{electrical}$)
    (a) Ohmic losses due to series resistance (P_{series})
    (b) Ohmic losses due to shunt resistance (P_{shunt})
    (c) Voltage losses due to non-radiative recombination (P_{NRRV})
    (d) Current losses due to non-radiative recombination (P_{NRRI})
4. System losses (P_{system})
    (a) Losses due to cell interconnection ($P_{intercon}$)
    (b) Mismatch losses ($P_{mismatch}$)
    (c) Cable losses (P_{cable})
    (d) Inverter losses ($P_{inverter}$)

The losses are defined such that the input power is equal to the sum of the different categories and the AC output power P_{AC}, which can be written as

$$P_{in} = P_{fund} + P_{optical} + P_{electrical} + P_{system} + P_{AC}. \tag{2.4}$$

2.3 Fundamental losses

Fundamental losses are losses that cannot be prevented or reduced without fundamentally changing the solar cell or its operating conditions. In this project, five fundamental losses are considered. The implementation for each of these losses will be discussed separately. The equations are defined such that they are not dependent on non-ideal parameters of a solar module, such as the EQE or V_{mpp}. However, by neglecting these non-ideal parameters, some of fundamental losses are overestimated and some are underestimated. To compensate for this, a certain non-ideality effect is defined at the end of this section. The total fundamental losses (P_{fund}) can be written as

$$P_{fund} = P_{term} + P_{below} + P_{emission} + P_{Carnot} + P_{angle} + P_{non-ideal}. \tag{2.5}$$

2.3.1 Thermalization losses

As discussed in Section 1.1, photons with a higher energy than the bandgap energy can generate an electron-hole pair. However, if photons have more energy, the difference between the photon energy and the bandgap energy will be lost as thermal heat [14]. This is referred to as thermalization. To calculate the total thermalization losses, this energy difference should be calculated for all photons with a wavelength smaller than the wavelength corresponding to the bandgap energy (λ_g). The thermalization losses can be calculated as

$$P_{term} = A_{mod} \int_0^{\lambda_g} \phi_{in}(\lambda) \left(\frac{h \cdot c}{\lambda} - E_g \right) d\lambda, \tag{2.6}$$

where A_{mod} is the area of the PV module, $\phi_{in}(\lambda)$ is the photon flux for a given wavelength λ, h and c are the plank constant and the speed of light respectively, and E_g is the bandgap energy of the solar cell. λ_g can be calculated with

$$\lambda_g = \frac{h \cdot c}{E_g}. \tag{2.7}$$

Temperature dependence of the bandgap energy

The bandgap energy of a solar cell generally depends on the temperature [65, 66]. This effect can be modelled by expressing the bandgap energy as a function of temperature. However, because the temperature dependence is not known for every material that is used, it is assumed that the bandgap remains constant for different temperatures.

2.3.2 Below bandgap losses

If photons have a lower energy than the bandgap energy, they are not able to generate an electron-hole pair. The energy of these photons will be lost as heat or as non-absorption [14]. This is called the below bandgap losses and it can be calculated by integrating over the incoming spectral irradiance (I_{in}) for all wavelengths larger than λ_g, which is written as

$$P_{below} = A_{mod} \int_{\lambda_g}^{\infty} I_{in}(\lambda) d\lambda, \tag{2.8}$$

where A_{mod} is the area of the module and $I_{in}(\lambda)$ is the spectral irradiance for a given wavelength λ. λ_g is calculated in the same way as for the thermalization losses.

2.3.3 Emission losses

Because a solar cell does also emit black body radiation, some of the incoming power is lost due to radiative recombination. This radiation can be modelled with the generalised Plank equation [14, 63, 67]:

$$\phi_E\left(E, T, \mu, \Omega\right) = \frac{2 \cdot \Omega}{c^2 \cdot h^3} \cdot \frac{E^2}{e^{\frac{E-\mu}{kT}} - 1} \tag{2.9}$$

In this equation ϕ_E is the number of emitted photons per energy, E is the energy of the emitted photons, T is the temperature of the object, μ is the chemical potential of the solar cell, and Ω is the solid angle of emission. Equation (2.9) is written as a function of energy, but it can also be written as a function of wavelength (ϕ_λ), as shown in Equation (2.10). This is done, such that it can be used in combination with the flux density per wavelength of the incoming spectrum (ϕ_{in}).

$$\phi_\lambda\left(\lambda, T, \mu, \Omega\right) = \frac{2 \cdot \Omega \cdot c}{\lambda^4} \cdot \frac{1}{e^{\frac{E-\mu}{kT}} - 1} \tag{2.10}$$

The total emission losses can be calculated by integrating over the wavelengths smaller than λ_g. Since a solar cell radiates photons with an energy equal to the bandgap energy, the number of emitted photons has to be multiplied with the E_g, written as

$$P_{emission} = A_{mod} \int_{0}^{\lambda_g} E_g \cdot \phi_\lambda\left(\lambda, T_{cell}, q \cdot V_{opt}, \Omega_{emit}\right) d\lambda, \tag{2.11}$$

where T_{cell} is the cell temperature, Ω_{emit} is the solid-state angle of emission, and V_{opt} is the optimal voltage, shown in Equation (2.13). The optimal voltage is more deeply discussed in the rest of this section.

2.3.4 Carnot and angle mismatch losses

The energy of an electron leaving the solar cell is typically lower than the bandgap energy. As shown in Equation (2.10), the emission losses depend on the cell voltage. This limits the cell voltage, as a too large voltage leads to much emission. The fundamental voltage limit can be derived by only considered radiative recombination, which can be modelled with the generalised plank equation (Equation (2.9)). The total absorbed power density (P) is calculated by multiplying the absorbed current with the optimal voltage, written as

$$P = q \cdot V_{opt} \left(\int_{E_g}^{\infty} \phi_{in}\left(E\right) dE - \int_{E_g}^{\infty} \phi_E\left(E, T_{cell}, q \cdot V_{opt}, \Omega_{emit}\right) dE \right), \tag{2.12}$$

where V_{opt} is the optimal voltage that maximises the absorbed power density. This voltage can be seen as the maximum power point voltage of an ideal solar cell. When black body (BB) irradiation is considered as input irradiation, an analytic equation for the optimal voltage can be derived, as shown in Equation (2.13). The derivation of this equation is shown in Appendix A.1.

$$V_{opt} = \frac{E_g}{q} - \frac{E_g}{q}\frac{T_{cell}}{T_{sun}} - \frac{k \cdot T_{cell}}{q} \ln\left(\frac{\Omega_{emit}}{\Omega_{abs}}\right) \tag{2.13}$$

The difference between the output voltage and the bandgap energy consists of two terms, namely $\frac{E_g}{q}\frac{T_{cell}}{T_{sun}}$ and $\frac{k \cdot T_{cell}}{q} \ln\left(\frac{\Omega_{emit}}{\Omega_{abs}}\right)$. These voltage differences are called the Carnot voltage (V_{Carnot}) and the angle mismatch voltage (V_{angle}) respectively. A description of Ω_{emit} and Ω_{abs} is given later in this section.

It should be noted that the value of the optimal voltage depends on the incoming irradiance spectrum. Only at black body irradiance, the optimal voltage has an analytic equation, whereas for other irradiances it has to be calculated numerically. To account for this, a scaling factor has been defined as a correction for the Carnot voltage and the angle mismatch voltage. This factor is the ratio of the difference between the bandgap energy and the optimal voltage at the given irradiance, and the difference between the bandgap energy and the optimal voltage at black body irradiance.

This leads to new equations for the Carnot voltage and the angle mismatch voltage, which are

$$V_{Carnot} = \frac{E_g}{q}\frac{T_{cell}}{T_{sun}} \cdot \frac{\frac{E_g}{q} - V_{opt}}{\frac{E_g}{q} - V_{opt,BB}}, \tag{2.14}$$

$$V_{Carnot} = \frac{k \cdot T_{cell}}{q} \ln\left(\frac{\Omega_{emit}}{\Omega_{abs}}\right) \cdot \frac{\frac{E_g}{q} - V_{opt}}{\frac{E_g}{q} - V_{opt,BB}}. \tag{2.15}$$

Carnot losses

Carnot losses occurs because the efficiency is limited when operating at two different temperatures [63, 68]. For solar cells, the different temperatures are the temperature of the sun and the operating temperature of the solar cell. The Carnot losses can be calculated by multiplying V_{Carnot} with the maximum output current I_{max}. Therefore, the Carnot losses can be calculated with the [14, 63, 64, 69]

$$P_{Carnot} = V_{Carnot} \cdot I_{max}. \tag{2.16}$$

I_{max} can be calculated by taking the difference of the number of incoming photons per wavelength (ϕ_{in}) and the number of emitted photons per wavelength and integrating over corresponding wavelength range, written as

$$I_{max} = A_{mod} \cdot q \int_0^{\lambda_g} \phi_{in}(\lambda) - \phi_\lambda\left(\lambda, T_{cell}, q \cdot V_{opt}, \Omega_{emit}\right) d\lambda. \tag{2.17}$$

Angle mismatch losses

The second term of the voltage difference is caused by a difference in solid angle between the absorption and emission of the solar cell. The power loss due to the angle mismatch can be calculated by multiplying V_{angle} with I_{max} [14, 63, 64]:

$$P_{angle} = V_{angle} \cdot I_{max} \tag{2.18}$$

In this equation, Ω_{emit} is the solid angle in which the solar cell emits its radiation. For monofacial solar cells, this is half of the unit sphere (2π sr) and for bifacial solar cell, this angle is a full unit sphere (4π sr) [70–72]. Ω_{abs} is the solid angle in which the solar cell absorbs the photons, which is the solid angle of the sun on the earth. Ω_{abs} can calculated to be around $6.8 \cdot 10^{-5}$ sr [73].

It can be argued that this angle only applies for direct irradiance, since diffuse or albedo radiation can come from larger angles. However, Ω_{abs} should be considered as a parameter for the amount of irradiance instead of the angle of incidence. Even though the diffuse and albedo radiation can come from different angles, this radiation is still coming from the sun. Therefore Ω_{abs} is equal for all the different types of irradiances.

2.3.5 Overestimation due to non-idealities effect

Considering an ideal solar cell leads to overestimating some losses. To compensate for this, two non-idealities effects are defined. These effects are added to have one power component accounting for the overestimation, which will be named $P_{non-ideal}$. The equation is shown in Equation (2.19), where $P_{non-ideal,1}$ and $P_{non-ideal,2}$ are the results of the two different effects. These two components are discussed separately in the rest of this section.

$$P_{non-ideal} = P_{non-ideal,1} + P_{non-ideal,2} \tag{2.19}$$

Overestimation of emission losses

The emission losses are calculated with V_{opt}. However, due to non-idealities the maximum power point voltage is typically lower than the optimal voltage. Therefore, the number of emitted photons will be lower since the cell voltage in Equation (2.11) should actually be lower. The overestimation due to this is the difference between actual emitted photons and calculated emitted photons. This difference has to be multiplied with E_{photon} to obtain the non-ideality effect as

$$P_{non-ideal,1} = A_{mod} \cdot E_{photon} \int_0^{\lambda_g} \phi_\lambda\left(\lambda, T_{cell}, q \cdot V_{mpp}, \Omega_{emit}\right) - \phi_\lambda\left(\lambda, T_{cell}, q \cdot V_{opt}, \Omega_{emit}\right) d\lambda, \tag{2.20}$$

where $E_{photon} = E_g - q \cdot V_{Carnot} - q \cdot V_{angle}$, which can be seen as the energy of the photon that can be absorbed. It should be noted that the difference will be negative, since the optimal voltage is higher, indicating that this is a gain due to non-ideality.

Absorption below bandgap

In theory a solar cell cannot absorb photons with an energy lower than the bandgap energy, since the theory assumes a zero absorption for wavelengths higher than λ_g. However, the EQE is typically nonzero for wavelengths larger than λ_g, which is described by Urbach's rule [74, 75]. This means that these photons can still be absorbed. The second non-ideality effect is calculated as

$$P_{non-ideal,2} = -A_{mod} \cdot E_{photon} \int_{\lambda_g}^{\infty} \left(\phi_{in}(\lambda) - \phi_\lambda\left(\lambda, T_{cell}, q \cdot V_{mpp}, \Omega_{emit}\right)\right) \cdot EQE(\lambda) d\lambda. \tag{2.21}$$

A minus sign is added in front of the equation, as it can be seen as power taken from the below bandgap losses. Therefore, it is considered as a gain, meaning the loss component should be negative.

Underestimation of thermalization losses

For the non-ideality effect of tandem modules another component is considered. For a non-ideal solar cell, it is possible for a high energy photon to be absorbed by the bottom cell instead of the top cell. This leads to an underestimation of the thermalization losses, which should be included in the non-ideality effect. However, this does not happen in a single-junction module, as there is only one absorber. The mathematical expression for this is discussed in Appendix A.2.

2.4 Optical losses

After the fundamental losses have been calculated, the optical losses can be quantified. As discussed in Section 1.4, the optical losses are all losses that prevents photons from being absorbed into the absorber material. As shown in the list of Section 2.2, there are four optical losses. The total optical losses ($P_{optical}$) can be written as

$$P_{optical} = P_{cell-spacing} + P_{metallization} + P_{ref,trans} + P_{par-abs}. \tag{2.22}$$

2.4.1 Losses due to cell spacing

Solar cells are typically in the shape of a pseudo square [76], which means they do not fully cover the area of a PV module. Also, the modules can have some empty space on the edges, which is not covered with solar cells. Although, it is still possible for these photons to be reflected onto the solar cell [76, 77], this is not considered as it is not compliant with the current version of the toolbox. The cell spacing losses can be calculated by multiplying the fraction of area that is not covered with solar cells with the difference between the total incoming power and the fundamental losses, such that losses are not counted double. Therefore, the losses due to cell spacing are written as

$$P_{cell-spacing} = (P_{in} - P_{fund}) \cdot \left(1 - \frac{N_{cells} \cdot A_{cell}}{A_{mod}}\right), \tag{2.23}$$

where N_{cells} is the number of cells, A_{cell} is the area of a single cell, A_{mod} is the area of the PV module, and P_{fund} is the sum of the fundamental losses as shown in Equation (2.5)

2.4.2 Shading losses due to metallization

To transport the electrons and holes away from the solar cell, metallic contacts are normally added to the front and back of the solar cell. Because these contacts occupy some area, they will also create some non-active area. It needs to be realised that the incoming photons might be reflected by the metal wires such that the photons still reach the active area. If the photons are reflected into an angle that is larger the critical angle of the corresponding interface, all the photons will be reflected [78]. This phenomenon is called total reflection and allows almost all reflected photons to be absorbed by the solar cell [79].

However, to make the implementation compliant with the current version of the Toolbox, a fraction of the solar cell is considered to be shaded. This is defined as the shading factor (SF). The shading factor causes an additional non-active area, which prevents photons from being absorbed. The losses due to metallization can be calculated with

$$P_{metallization} = (P_{in} - P_{fund}) \cdot \frac{N_{cells} \cdot A_{cell}}{A_{mod}} \cdot SF. \tag{2.24}$$

2.4.3 Reflection and transmission losses

When a photon hits the active area of the PV module, it still might not be absorbed due to reflection or transmission. Because air and the solar cells typically have a different refractive index, there will be reflection as described by the Fresnel equations [78]. There will also be a part of the light, which is not absorbed at all and transmits through the solar cell, which is described by Lambert-Beer's law [11].

However, the absorption model of the toolbox can be used to calculate the reflection and transmission losses. As described in Section 1.3, the absorption, reflectance, and transmission are calculated in this model for different angles. An example of a typical result from the optical model is shown in Figure 2.2.

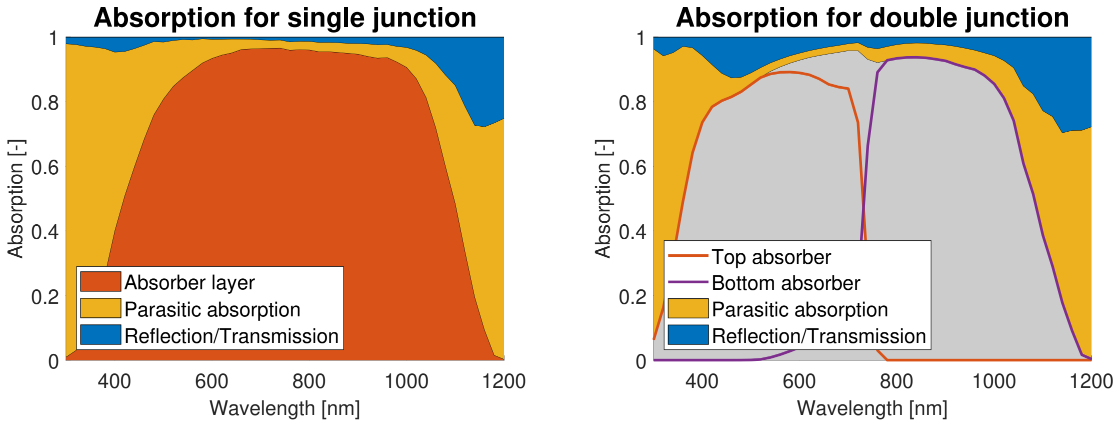

(a) The results of the optical model for a single junction solar cell.

(b) The results of the optical model for a double junction solar cell.

Figure 2.2: An example of the output of the optical simulation of two solar cells. For each wavelength, the reflection, parasitic absorption and absorption in the absorber layer is shown.

These results can be used to calculate the reflection and transmission losses by multiplying the photon flux at each wavelength with the reflectivity/ transmissivity. For each photon, the fundamental losses should not be included, which means that each photon loses an energy of E_{photon} (as defined in Section 2.3). The total reflection and transmission losses can be calculated as

$$P_{ref,trans} = A_{eff} \int_0^{\lambda_g} (\phi_{in}(\lambda) - \phi_{\lambda,emission}(\lambda)) \cdot (R(\lambda) + T(\lambda)) \cdot E_{photon} d\lambda, \tag{2.25}$$

where A_{eff} is the effective area ($A_{eff} = N_{cells} \cdot A_{cell} \cdot (1 - SF)$), and $R(\lambda)$ and $T(\lambda)$ are the reflectivity and transmissivity at each wavelength respectively.

It should be noted that transmission typically only occurs for bifacial solar cells. Mono-facial solar cells normally have a metal reflector at the back to prevent transmission.

2.4.4 Parasitic absorption

Solar cells typically have other layers that do not generate electron-hole pairs, which can absorb photons [76]. This is called parasitic absorption. The results shown in Figure 2.2 can be used to calculate this loss. For each wavelength, the photon flux should be multiplied with the parasitic absorptivity ($\alpha_{par} = (1 - R(\lambda) - T(\lambda) - \alpha(\lambda))$, where $\alpha(\lambda)$ is the absorptivity of the solar cell). Similar to the reflection/transmission losses, this should be multiplied with the energy E_{photon}. The equation for the losses due to parasitic absorption can be written as

$$P_{par-abs} = A_{eff} \int_0^{\lambda_g} (\phi_{in}(\lambda) - \phi_{\lambda,emission}(\lambda)) \cdot \alpha_{par}(\lambda) \cdot E_{photon} d\lambda. \tag{2.26}$$

2.5 Electrical losses

After photons have been absorbed by solar cell, there are also losses when photons transfer their energy into electricity. As discussed in Section 1.4, the electrical losses can be divided into ohmic losses and recombination losses. These losses are calculated on cell level, so the total losses are the sum of the individual cells. Therefore, the total electrical losses ($P_{electrical}$) can be written with the following equation:

$$P_{electrical} = \sum_{i=1}^{N_{cells}} (P_{series,i} + P_{shunt,i} + P_{NRRI,i} + P_{NRRV,i}) \tag{2.27}$$

It should be noted that the electrical losses are calculated as if all cells are operating at their maximum power point. In the equations in this section, the values of I_{mpp} and V_{mpp} are derived from the IV curve of the individual cells. The difference between the output power at the maximum power point and actual operating power point is included in the system losses.

For tandem cells, the electrical losses are calculated for top and bottom cell separately. The values of I_{mpp} and V_{mpp} are derived from the individual IV curves.

2.5.1 Ohmic losses

The materials in a solar cell have a resistivity, which creates ohmic losses. These ohmic losses can be divided into two types. The first type comes from the resistance in the bulk and contacts, which is represented with the series resistance in the five-parameter model [22]. The second type comes from a leakage current since the solar cell has a conductance. This type is represented with the shunt resistance in the five-parameter model [23].

Series resistance losses

The losses due to the series resistance can be calculated by multiplying the current through the resistor, which is I_{mpp}, with the voltage drop over the resistor V_{series}. The voltage drop is calculated with Ohm's law. The series resistance losses can be calculated as

$$P_{series} = I_{mpp}^2 \cdot R_s. \tag{2.28}$$

Shunt resistance losses

The voltage over the shunt resistor is equal to $V_{mpp} + I_{mpp} \cdot R_s$. The current through the resistor is this voltage divided by R_{sh}, which will later be referred to as I_{shunt}. Therefore, the shunt resistance losses can be calculated with

$$P_{shunt} = \frac{(V_{mpp} + I_{mpp} \cdot R_s)^2}{R_{sh}}, \tag{2.29}$$

2.5.2 Recombination losses

Besides radiative recombination, it is possible that holes and electrons recombine in the solar cell without radiating photons [14, 48]. These recombined holes and electrons will not contribute to the output current, reducing the generated electricity. This is called the non-radiative recombination (NRR). This can be separated into a current component (P_{NRRI}), which accounts for the loss in current, and a voltage component (P_{NRRV}), which accounts for a loss in voltage.

The power loss due to non-radiative recombination can be calculated in different ways. Three methods will be presented, that will be discussed individually. Each method will be based on the five-parameter model, which is discussed in Section 1.1.

Method 1

The first method defines non-radiative recombination losses as the difference between the power of current source in the five-parameter model (I_{ph}) and the output power combined with the resistive losses. This can be divided in the voltage component (P_{NRRV}) and the current component (P_{NRRI}) The voltage loss due to NRR (V_{NRRV}) can then be calculated as

$$V_{NRRV} = V_{opt} - V_{mpp} - V_{series}. \tag{2.30}$$

The power loss due to a voltage difference can then be calculated by multiplying V_{NRRV} with I_{ph}, as shown in Equation (2.31). The reason for multiplying with I_{ph}, is that every generated electron hole pair experiences this voltage loss.

$$P_{NRRV} = V_{NRRV} \cdot I_{ph} \tag{2.31}$$

The current component be calculated in a similar way by taking the difference between the absorbed current and the output current combined with the shunt resistance current. This current loss (I_{NRRI}) can be seen as the current flowing into the diode of the five-parameter model and is written as

$$I_{NRRI} = I_{ph} - I_{mpp} - I_{shunt}. \tag{2.32}$$

The power loss due to a current difference can then be calculated by multiplying the current loss with the voltage over the diode:

$$P_{NRRI} = I_{NRRI} \cdot (V_{mpp} + V_{series}). \tag{2.33}$$

The advantage of this method is that it is relatively simple. Both V_{NRRV} and I_{NRRI} are calculated by taking the voltage difference and current difference respectively, which is less complicated than the other methods. Another advantage is that everything in the end adds up to 100% exactly. By defining V_{NRRV} and I_{NRRI} as they are defined, the losses combined with the output power will always be equal to P_{in}. This is desirable because this means that all the losses have been identified. The disadvantage of this method is that it is physically less accurate compared to the other methods. For this method, no equation describing that describe a physical process are used to calculate the voltage and current recombination loss.

Method 2

The second method is a variation of the first method. V_{NRRV} and P_{NRRV} are calculated still calculated with Equation (2.30) and (2.31). The current loss is the current through the diode and can be modelled with

$$I_{recom} = I_0 \cdot \left(e^{\left(\frac{V_{MPP} + I \cdot R}{n \cdot V_t} \right)} - 1 \right), \tag{2.34}$$

where, I_{recom} is the recombination current, both the non-radiative recombination current and the radiative recombination current. Since radiative recombination losses are already included in the fundamental losses, this needs to be excluded. This can be done with the external radiative efficiency (ERE), which is the fraction of total recombination current that results in radiative emission current [80]. It can be determined by calculating the radiative emission at V_{oc}, since the output current is zero at this voltage. That means that at this operating point the recombination current equals I_{ph} [80], meaning that

$$ERE = \frac{\frac{A_{eff}}{N_{cells}} \int EQE(\lambda) \cdot \phi_\lambda \left(\lambda, T_{cell}, q \cdot V_{oc}, \Omega_{emit} \right) d\lambda}{I_{ph}}, \tag{2.35}$$

where $\frac{A_{eff}}{N_{cells}}$ is the effective area per cell, $EQE(\lambda)$ is the external quantum efficiency, and ϕ_λ is the emitted photons per wavelength at V_{oc} as shown by Equation (2.10).

With the external radiative efficiency, the non-radiative recombination current can be calculated as shown in Equation (2.36). The total recombination current is multiplied with the term $(1-ERE)$, because this is the fraction of recombination current due to non-radiative recombination. Finally, the recombination current loss can be calculated as

$$P_{NRRI} = I_{recom} \left(1 - ERE \right) \cdot \left(V_{mpp} + V_{series} \right). \tag{2.36}$$

The advantages of this method compared to method 1 is that it is more physically accurate, as it uses the diode equation to model the recombination current. The downside of the method is that the calculation of voltage loss is still not physically accurate, because it is still defined as the remaining voltage. Also, the final results do not add up to 100% exactly, since numerical deviations occur during the implementation. This will be discussed more deeply in the next method.

Method 3

In method 3, both the voltage and current loss are calculated with physical processes. Due to the non-radiative recombination processes, the maximum power point voltage becomes lower. The derivation of the optimal voltage, as shown in Section 2.3, can be repeated, but with non-radiative recombination losses as well. To do this, the radiative emitted photons have to be multiplied with $\frac{1}{ERE}$, since this would then be the total recombination current. This leads to an analytic expression for the maximum power point voltage:

$$V_{mpp} = \frac{E_g}{q} - \frac{E_g}{q} \frac{T_{cell}}{T_{sun}} - \frac{n \cdot k \cdot T_{cell}}{q} \ln \left(\frac{1}{ERE} \frac{\Omega_{emit}}{\Omega_{abs}} \right) \tag{2.37a}$$

$$V_{mpp} = \frac{E_g}{q} - \frac{E_g}{q} \frac{T_{cell}}{T_{sun}} - \frac{n \cdot k \cdot T_{cell}}{q} \ln \left(\frac{\Omega_{emit}}{\Omega_{abs}} \right) - \frac{n \cdot k \cdot T_{cell}}{q} \ln \left(\frac{1}{ERE} \right) \tag{2.37b}$$

$$V_{mpp} = V_{mpp,ideal} - \frac{n \cdot k \cdot T_{cell}}{q} \ln \left(\frac{1}{ERE} \right) \tag{2.37c}$$

The non-radiative recombination voltage loss can be written as

$$V_{NRRV} = \frac{n \cdot k \cdot T_{cell}}{q} \ln \left(\frac{1}{ERE} \right). \tag{2.38}$$

The external radiative efficiency is calculated with Equation 2.35. The recombination voltage loss can then be multiplied with the absorbed current, shown in Equation 2.31. The current recombination loss is calculated the same as method 2, which is done with Equation 2.36 and 2.33.

The advantage of method 3 is that everything is described with physical processes, and it is compliant with the five-parameter model. The disadvantage of this method is that all the losses and output power may not add up to 100%. This happens, since the implementation of method 3 introduces small numerical differences. An explanation for this, could be the fact that the electrical model discretizes the irradiation and the temperature. However, this is something that can be further investigated in future work.

Motivation for used method

The method that will be used for the rest project is method 1, since the implementation is relatively simple, and it does not introduce numerical deviations. Also, the difference between the absorbed energy and the output energy combined with ohmic losses is lost due to recombination, which justifies using method 1.

The deviations by using method 2 and 3 are shown in Appendix A.3. In the rest of this chapter, method 1 will be considered.

2.6 System losses

The last losses that are considered are system losses, which happen after the electricity is generated at cell level. These losses include the cell interconnection, the mismatch, the cable, and the inverter losses. The total system losses (P_{system}) can be written as

$$P_{system} = P_{intercon} + P_{mismatch} + P_{cable} + P_{inverter}. \tag{2.39}$$

2.6.1 Cell interconnection losses

To couple different modules into a PV system, each module is connected via an interconnection. These interconnections also have some resistance ($R_{intercon}$) [76]. The loss due to this resistance is the current through the interconnection multiplied with the voltage, written as

$$P_{intercon} = I_{module}^2 \cdot R_{intercon}. \tag{2.40}$$

2.6.2 Mismatch losses

The IV curves of solar cells within module are not always identical. Therefore, the maximum power point of an individual cell can be different than the maximum power point of the module. This makes the cell operate on a different operating point than its own maximum power point, which can be seen as a loss.

The mismatch losses are calculated by taking the difference between the sum of the individual maximum power point powers and the actual output power. This can then be written as

$$P_{mismatch} = \left(\sum_{i=1}^{N_{cells}} P_{mmp,i} \right) - I_{module} \cdot \left(V_{module} + I_{module} \cdot R_{intercon} \right). \tag{2.41}$$

For tandem PV modules, a similar equation can be used. Since the electrical losses are calculated for top and bottom cell separately, the mismatch losses are calculated as

$$P_{mismatch} = \left(\sum_{i=1}^{N_{cells}} P_{mmp-top,i} + P_{mmp-bottom,i} \right) - I_{module} \cdot (V_{module} + I_{module} \cdot R_{intercon}) \,. \quad (2.42)$$

2.6.3 Cable losses

To transport the electricity to the inverter, the modules are connected via cables. Because the cables have some resistance, there will be some power loss. The inverter model, as discussed in Section 1.3, calculates the efficiency of the cables. This efficiency can be used for the cable losses, which can be calculated with

$$P_{cable} = P_{in-cable} \cdot (1 - \eta_{cable}) \,. \quad (2.43)$$

In this equation, $P_{in-cable}$ is the power that goes into the cables and η_{cable} is the efficiency of the cables that is provided by the inverter model of the Toolbox.

2.6.4 Inverter losses

When the inverter converts the DC power into AC power, there are typically some losses. The inverter model (discussed in Section 1.3), calculates the AC output power. The inverter losses can be calculated as the difference between the in-going DC power and the out-coming AC power, which can be written as

$$P_{inverter} = P_{DC-in} - P_{AC} \,. \quad (2.44)$$

2.7 Theoretical validation of the implementation

Before the implementation can be used to analyse PV modules, it should first be validated. Two types of theoretical validation will be done. First, it will be shown that the calculations add up to 100%, such that all the outgoing power is equal to the incoming power. This can be considered as a mathematical validation. The validation will be done for both single junction and tandem junction solar cells. The implementation for the calculation of a tandem junction solar cell is similar to the implementation described above. A detailed discussion about of the implementation for tandem modules can be found in Appendix A.2

The other validation that will be done is a comparison with fundamental limits described in literature. Since the fundamental losses are defined such that they do not depend on non-ideal properties, the fundamental losses can be used to estimate the fundamental limit of the solar cell. If the values of the fundamental losses match the values from the literature, this is an indication that the implementation is accurate. This can be considered as a physical validation.

2.7.1 Mathematical validation

To validate the implementation, the loss analysis of a single and tandem junction module has been calculated. The single junction module is a mono-facial crystalline silicon module, and the tandem junction module is a two-terminal perovskite/silicon module. The results of the calculations for both modules are shown in Figure 2.3 and Table 2.1. Both calculations are done for STC.

The sum over all the percentages equals 100% for both solar cells, which can be seen in Table 2.1. This means that all the input power has been found. This indicates that the implementation is mathematically valid.

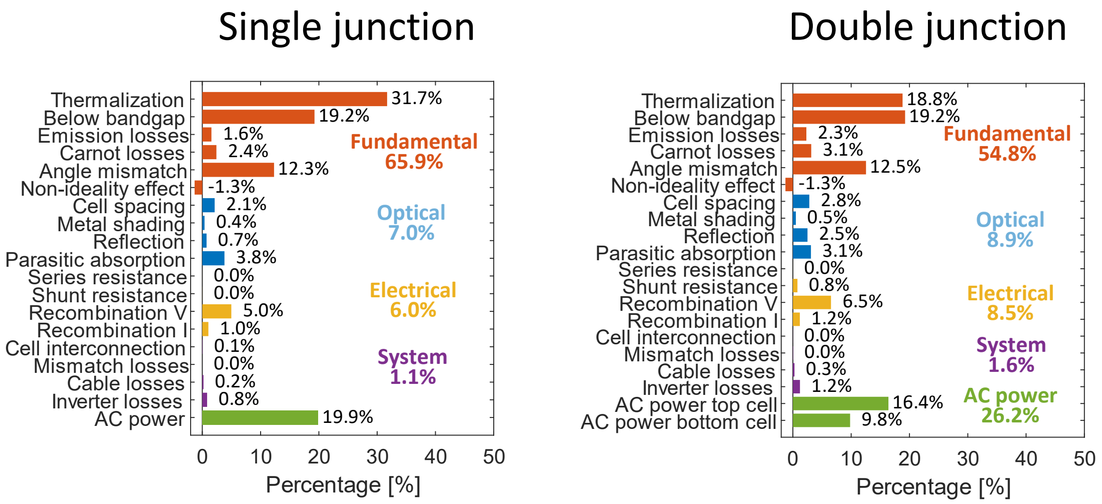

(a) The loss distribution for a single junction crystalline silicon module.

(b) The loss distribution for a tandem silicon/perovskite module.

Figure 2.3: The results of the calculations. On the left, a single junction mono crystalline silicon module is considered. On the right, a two-terminal perovskite/silicon module is considered.

Table 2.1: The power distribution of the various categories for the single module and the tandem module. Note that the sum over the categories may not add up to 100% due to rounding at one decimal.

Category	Single module [%]	Tandem module [%]
Fundamental	65.9	54.8
Optical	7.0	8.9
Electrical	6.0	8.5
System	1.1	1.6
Power	19.9	26.2
Total	100.0	100.0

2.7.2 Physical validation

To physically validate the implementation, the fundamental losses are compared to values from literature. Different upper limits have been defined for both single and tandem junction cells. For this work, the upper limit (η_{upper}) is defined in as

$$\eta_{upper} = \frac{P_{in} - (P_{term} + P_{below} + P_{emission} + P_{Carnot} + P_{angle})}{P_{in}}. \tag{2.45}$$

The upper limit according to the implementation is 32.8% for single junction modules and 44.1% for tandem junction modules. The upper limit for a single junction is compared to the limit described by Shockley and Queisser [15], and the limit described by Richter [16]. The upper limit for the tandem junction is compared to the limit described by De Vos [25].

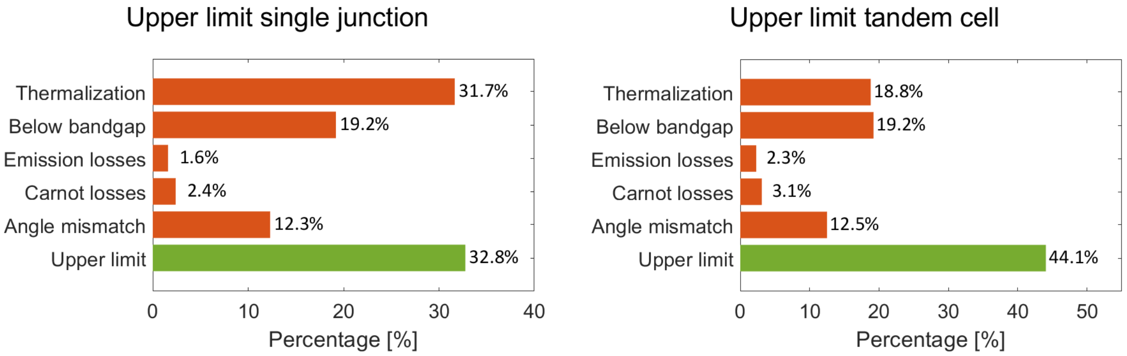

(a) The upper limit for a single junction module.

(b) The upper limit for a tandem module.

Figure 2.4: The upper limit of a single solar cell and tandem solar cell. For the upper limit, only the fundamental losses are considered.

Upper limit for single junction solar cells

The upper limit calculated by Shockley and Queisser is 30%, which is slightly different than the calculated limit of this project. The most important reason is that a different irradiance spectrum is considered. The results shown in Figure 2.3 are obtained under the AM1.5 spectrum, whereas the limit of Shockley and Queisser is calculated with black body radiation of the sun. If black body radiation is also considered as irradiance spectrum, the new upper limit according to this work becomes 30.0%, which agrees with the limit of Shockley and Queisser. The differences between the two spectra are shown in Figure 2.5. The results of the loss analysis under black body radiation are discussed in Appendix A.4.

The upper limit calculated by Richter is 29.4% for a $110\mu m$ thick silicon solar cell [16]. This is also slightly different than the derived limit of 32.8%. However, there are two significant differences between the calculations of both limits. Firstly, Richter calculated the limit for a crystalline silicon solar cell and included parameters specific for crystalline silicon solar cells, such as the intrinsic carrier concentration. This is different than the calculation of the fundamental losses, where no material

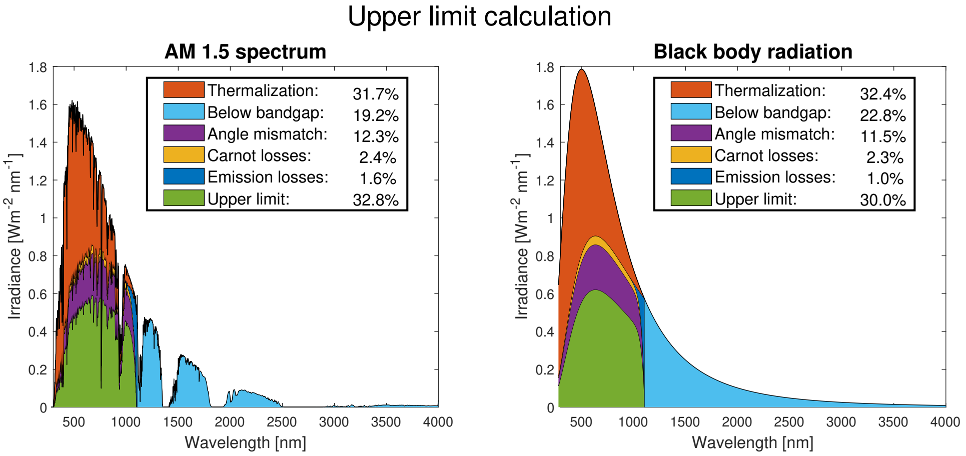

Figure 2.5: The difference in upper limit for a single junction solar cell between the AM1.5 spectrum (on the left) and the black body radiation (on the right).

specific parameters are used. The other main difference is that Richter also included non-radiative recombination in his calculations. Non radiative recombination, such as Auger recombination, also gives an upper bound for the limit for silicon solar cells [81]. However, this loss is not categorized as fundamental in the implementation since it is a material dependent parameter and not fundamental in general. Therefore, it is not included in the upper limit, which can explain the difference between both limits.

Upper limit for a tandem junction solar cell

The upper limit calculated by De Vos is 42% for a tandem junction solar cell, which varies slightly with the derived limit of 44.1%. De Vos calculated its limit with black body radiation instead of the AM1.5 spectrum. Therefore, the results of the loss analysis under black body radiation (discussed in Appendix A.4) should be taken as a reference. Under this spectrum, the upper limit is 40.6%. The reason for the difference with the limit of De Vos, is that different bandgap energies are used. In the ideal case, the bottom cell has a bandgap energy of 1.0 eV and the top cell has a bandgap energy of 1.9 eV [25], which are different than the bandgap energies of the simulated tandem PV module. However, the equations for the fundamental losses can also be used for the ideal bandgap energies. As discussed in Appendix A.4, the upper limit for this situation is 42.0%, which agrees with the value calculated by De Vos.

Another difference is that De Vos also considered emission losses being absorbed by the other cell, which is known as photon recycling. This could then increase the number of absorbed photons. However, this is not considered in the implementation since it would make the calculation more complicated. Moreover, emission losses are relatively low which means that emitted photons being re-absorbed will also be relatively low.

Overview of different upper limits

This section has described multiple upper limits for both single junction solar cells and tandem junction solar cells. Also, two different spectra are used, namely the AM1.5 spectrum and black body radiation of the sun. An overview of the different upper limits is shown in Table 2.2.

Table 2.2: An overview of the different upper limits (η_{upper}). The first row lists the upper limits at the AM1.5 spectrum and the second row lists the upper limits at black body radiation.

Spectrum	Single junction [%] $E_g = 1.12eV$	Tandem junction [%] $E_{g1} = 1.68eV, E_{g2} = 1.12eV$	Tandem junction [%] $E_{g1} = 1.9eV, E_{g2} = 1.0eV$
AM1.5	32.8	44.1	-
Black body	30.0	40.6	42.0

2.8 Deviations due to numerical methods

Because the irradiance spectrum is typically not an analytic function, but a set of measured data points, numerical methods have to be used. In this section, two rooms for deviations regarding numerical methods need to be considered.

2.8.1 Method of integration

For some losses, integration over the irradiance spectrum is required. This integration cannot be done analytically, but has to done numerically, as the incoming spectrum is typically defined pointwise. Numerical integration is a whole field of science on its own [82]. However, only two different methods will be considered. These methods are integration with the Riemann sum and trapezoidal integration [83]. The difference between the two methods is shown in Figure 2.6.

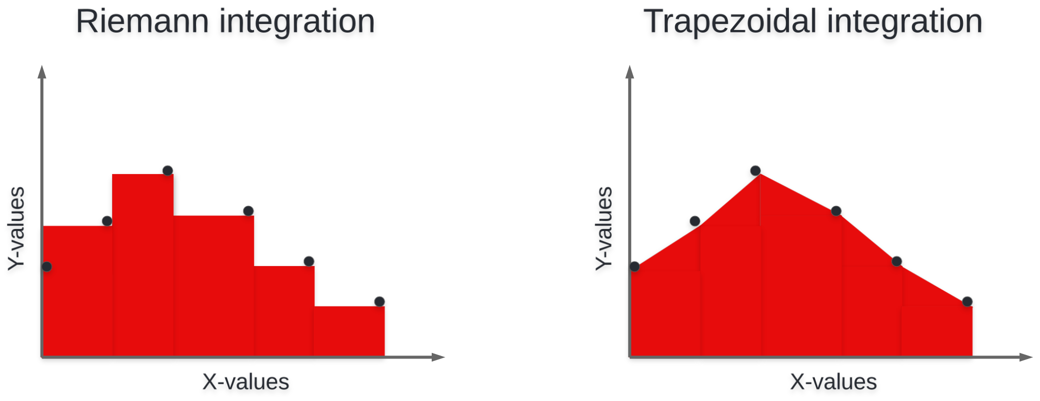

(a) An illustration of integration based on the Riemann sum.

(b) An illustration of integration based on the trapezoidal method.

Figure 2.6: The difference between integration based on the Riemann sum and trapezoidal integration.

In general, there will be a different outcome, based on which method is used. As an example, the total amount of power in the AM1.5 spectrum is calculated by using both methods. The results are shown in Table 2.3. The difference between both methods is 0.047%, which means that the methods do not vary significantly. For the equations in this study, trapezoidal integration is used, as it has a better accuracy for most analytical functions [84]. Even though the incoming spectrum is typically not defined analytically, it is assumed that the trapezoidal integration is more accurate.

Table 2.3: The irradiance in the AM1.5 spectrum calculated with two different methods of integration.

Method of integration	Power in AM1.5 spectrum [W]
Riemann sum	999.3970
Trapezoidal	999.8660

2.8.2 Wavelength range and interval

One of the inputs of GenPro4 is the interval between two wavelength points and the total wavelength range. Both of them are important parameters for the simulations of the optical model, and thus they can have an effect on the final results. In Table 2.4 the results for a mono-facial silicon PV module are presented for different wavelength settings. It can be seen that the maximum deviation is 0.02%. The reason for choosing 1200 nm and 2400 nm as final wavelength, is that 1200 nm is slightly larger than λ_g of silicon, and 2400 nm ensures that 99% of the AM1.5 spectrum is included.

The wavelength interval and final wavelength that are used are 10 nm and 1200 nm respectively. These values are chosen as the are the default setting of GenPro4 and a variation in settings does not have significant differences in the results.

Table 2.4: The results for different wavelength settings. It can be seen that there is at most 0.02% deviation.

$\Delta\omega$ [nm]	2		5		10		15		20	
ω_2 [nm]	1200	2400	1200	2400	1200	2400	1200	2400	1200	2400
P_{term}	31.71	31.71	31.71	31.71	31.71	31.71	31.71	31.71	31.71	31.71
P_{below}	19.25	19.25	19.25	19.25	19.25	19.25	19.25	19.25	19.25	19.25
$P_{emission}$	1.57	1.57	1.57	1.57	1.57	1.57	1.57	1.57	1.57	1.57
P_{Carnot}	2.42	2.42	2.42	2.42	2.42	2.42	2.42	2.42	2.42	2.42
P_{angle}	12.31	12.31	12.31	12.31	12.31	12.31	12.31	12.31	12.31	12.31
$P_{non-ideal}$	-1.32	-1.32	-1.32	-1.32	-1.32	-1.32	-1.32	-1.32	-1.32	-1.32
$P_{cell-spacing}$	2.12	2.12	2.12	2.12	2.12	2.12	2.12	2.12	2.12	2.12
$P_{metallization}$	0.38	0.38	0.38	0.38	0.38	0.38	0.38	0.38	0.38	0.38
$P_{ref,trans}$	0.74	0.74	0.74	0.74	0.74	0.75	0.74	0.73	0.74	0.74
$P_{par,abs}$	3.78	3.78	3.78	3.78	3.78	3.79	3.78	3.79	3.78	3.79
P_{series}	0.00	0.00	0.00	0.00	0.00	0.00	0.00	0.00	0.00	0.00
P_{shunt}	0.01	0.01	0.01	0.01	0.01	0.01	0.01	0.01	0.01	0.01
P_{NRRV}	4.98	4.98	4.98	4.98	4.98	4.98	4.98	4.98	4.98	4.98
P_{NRRI}	1.05	1.05	1.05	1.05	1.05	1.05	1.05	1.05	1.05	1.05
P_{inter}	0.05	0.05	0.05	0.05	0.05	0.05	0.05	0.05	0.05	0.05
$P_{mismatch}$	0.00	0.00	0.00	0.00	0.00	0.00	0.00	0.00	0.00	0.00
P_{cables}	0.21	0.21	0.21	0.21	0.21	0.21	0.21	0.21	0.21	0.21
$P_{inverter}$	0.83	0.83	0.83	0.83	0.83	0.83	0.83	0.83	0.83	0.83
P_{out}	19.91	19.90	19.90	19.91	19.90	19.89	19.91	19.90	19.91	19.89
P_{total}	100.00	100.00	100.00	100.00	100.00	100.00	100.00	100.00	100.00	100.00

2.9 Conclusion

This chapter presented the implementation of the loss analysis for the PVMD Toolbox, fulfilling the first sub-goal described in Section 1.5. 17 different loss components and a non-ideality effect have been identified and are divided into four categories (fundamental, optical, electrical, and system losses). For all components, equations have been defined to quantify the different losses.

For this implementation, two validations are done. First, a mathematical validation is done by showing that the sum of all losses and output power equals the incoming power. This indicates that all energy has been identified. The second validation is a physical validation, where the upper limit of a single junction and a tandem solar cell are compared to upper limits calculated in literature. For both solar cells, the calculated upper limit matches the value from literature. Therefore, the first sub-goal is achieved successfully. In the next chapter, this model will be used to calculate the loss distribution for different modules at STC.

3. Loss analysis under standard test conditions

The second sub-goal of this study is to analyse the loss distribution of different PV modules under STC. In this chapter, four different modules will be considered: a mono-facial crystalline silicon, a bifacial crystalline silicon, a mono-facial two terminal perovskite/silicon tandem, and a mono-facial three terminal tandem perovskite/silicon module. The single junction modules are included as a reference for the tandem modules. By using the equations defined in chapter 2, the different losses are calculated.

First, the design of the cells and modules will be discussed. After this, the cell structures, and the optical and electrical properties are analysed. To understand the differences in the loss analysis, the results will be comparisons with each other. Finally, the conclusion is presented.

3.1 The design of the cells

The designs of the different solar cells are based on the monolithic perovskite/silicon two-terminal tandem solar cell from Al-Ashouri et al [85], which has a power conversion efficiency of 29.15%. The design of the solar cell has been implemented and validated into the Toolbox by the PVMD research group [41]. To make the cell more realistic, the thickness of the silicon layer is reduced to a standard thickness and encapsulation is added. Also, the perovskite thickness is changed in order to achieve current matching. For the design for the mono-facial crystalline silicon cell and a bifacial crystalline silicon, the top layer is removed to observe the effect of adding a top layer. By comparing the mono-facial crystalline silicon cell with the perovskite/ silicon tandem cell, the effect of an additional layer can be seen. Finally, the design of the tandem cell has been adjusted such that the cell can operate as three-terminal tandem cell. This has been done to compare the loss distribution of two-terminal and three-terminal tandem modules.

In the rest of this section, the different cell structures and characteristics are discussed. A brief comparison between the structures of the four cells can be found in Figure 3.1.

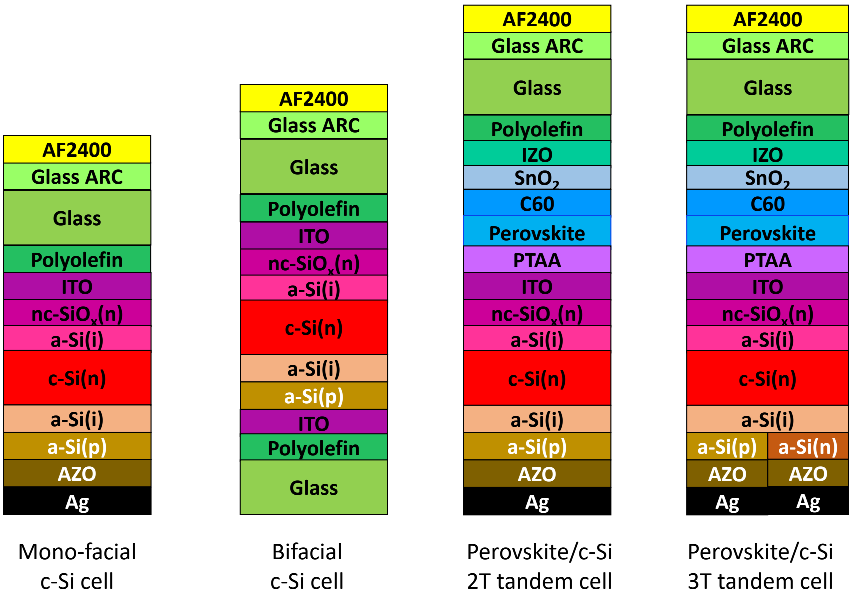

Figure 3.1: The structures of the different cells. Note that both tandem cells are mono-facial.

3.1.1 The mono-facial crystalline silicon cell

As mentioned before, this cell is based on the bottom part of the tandem module. The results for this cell can then be used to observe the increase in efficiency by adding the top cell. Another difference is that the texturing of the crystalline silicon is not removed for the front. Therefore, the silicon layer for this cell is double textured, whereas the silicon layer in the tandem cell is only rear textured. The structure of the mono-facial cell, which is fed as an input to GenPro4, is shown in Table 3.1.

Table 3.1: The structure of the mono-facial module that is used as an input.

Layer	Thickness [μm]
AF2400 [86]	0.093
Porous glass AR [87]C	0.053
Glass with low iron (Fe2O3) [88]	3200
Polyolefin-UVT	450
ITO [89]	0.063
n-SiOx (n)	0.020
a-Si(i) [89]	0.009
c-Si, bulk n-type (Double textured)	160
a-Si (i) [89]	0.006
a-Si (p) [89]	0.012
AZO	0.055
Ag [90]	0.30

After simulating this cell in the Toolbox, the optical and electrical properties of the cell can be obtained. The EQE and the IV curve on this cell are shown in Figure 3.2. It can be seen that the maximum power density (p_{mpp}) at cell level is 226.13 W/m^2, resulting in a cell efficiency of 22.6% at STC.

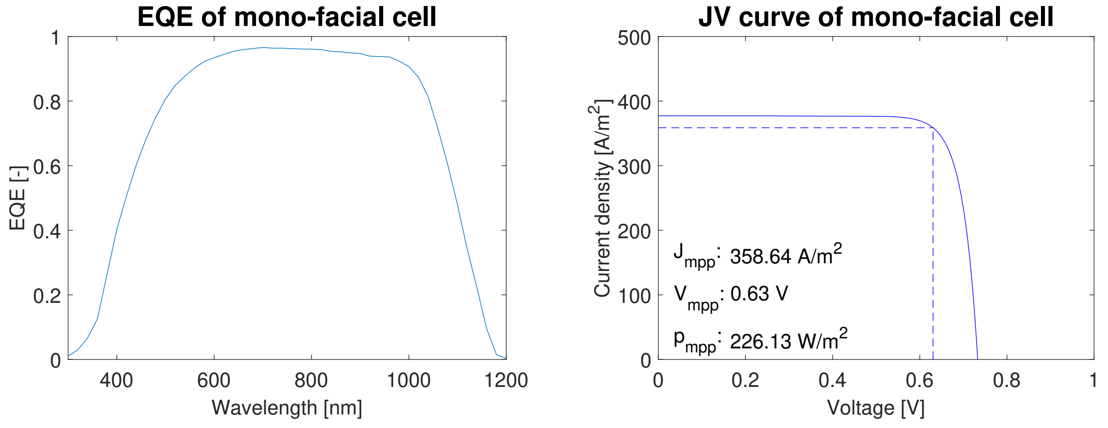

(a) The EQE curve of the mono-facial solar cell (b) The IV curve of the mono-facial solar cell

Figure 3.2: The EQE and the IV curve of the mono-facial solar cell.

3.1.2 The bifacial crystalline silicon cell

The structure of bifacial cell is similar to structure of the mono-facial cell and is shown in Table 3.2. The main difference is that rear contact has been replaced with glass, such that light can enter from both sides. Also, the thickness of the glass is changed. This cell is also included in the study to observe the difference in loss distribution between mono-facial and bifacial cells.

Table 3.2: The structure of the bifacial module that is used as an input.

Layer	Thickness [μm]
AF2400 [86]	0.093
Porous glass ARC [87]	0.053
Glass with low iron (Fe2O3) [88]	2000
Polyolefin-UVT	450
ITO [89]	0.063
n-SiOx (n)	0.020
a-Si(i) [89]	0.009
c-Si, bulk n-type (Double textured)	160
a-Si (i) [89]	0.006
a-Si (p) [89]	0.012
ITO [89]	0.063
Polyolefin-UVT	450
Glass with low iron (Fe2O3) [88]	2000

For bifacial solar cells, irradiance can come both from the front and the back. However, for the normal AM1.5 spectrum, only light from the front is considered. To also analyse the performance of the solar cell for light from the back, a new spectrum can be defined [91]. For this report, the new spectrum (which will referred to as B-STC) will be the AM1.5 spectrum at the front, and 20% of the AM1.5 spectrum at the rear.

Another aspect for bifacial solar cell, is the bifaciality factor (f_b). This is the ratio of its performance when light comes from the back over the performance when light comes from the front. This can be written as

$$f_b = \frac{\eta_{rear}}{\eta_{front}}. \tag{3.1}$$

For simplicity, f_b is assumed to be equal to 1, which is valid according to the work of H. Schulte-Huxel [92]. The main reason for this, is that the Toolbox does not include rear irradiance for STC calculations. By assuming f_b is equal to 1, the B-STC performance can be analysed by multiplying the photo-generated current with 1.2.

The EQE and the IV curve of the bifacial solar cell are shown in Figure 3.3. It can be seen that there is a small difference between the EQE of the front side and the rear side. However, the ratio of the optical performance of the rear side and the front side is 93% (when illuminating both sides with the AM1.5 spectrum), justifying the method for simulating bifacial modules. The output cell power density is 270.03 W/m^2. Because the incoming irradiance for B-STC is 1200 W/m^2, the cell efficiency is 22.5%.

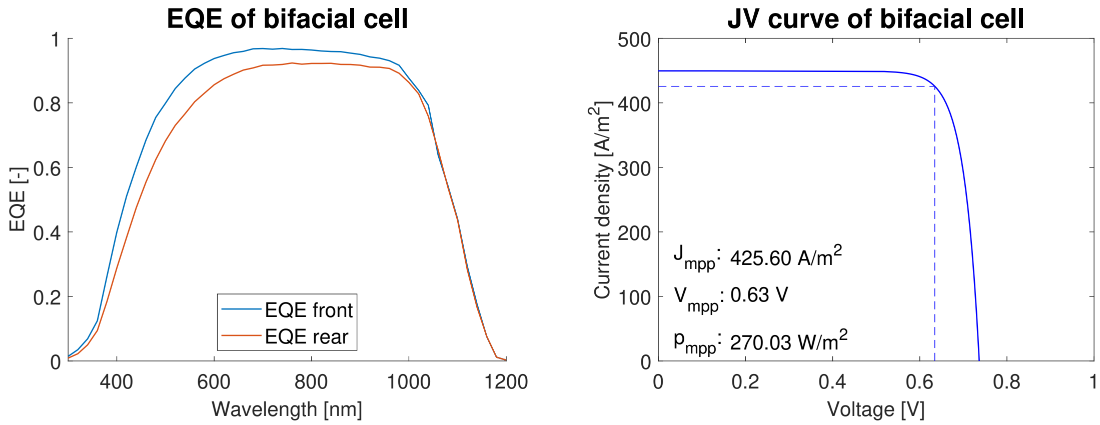

(a) The EQE curve of the bifacial solar cell (b) The IV curve of the bifacial solar cell

Figure 3.3: The EQE and the IV curve of the bifacial solar cell.

3.1.3 The perovskite/silicon two-terminal tandem cell

The next cell is the tandem cell as originally developed by Al-Ashouri et al. The only changes are the addition of encapsulation, and the changes in the silicon and perovskite thickness to make the cell more feasible for large scale production. The structure of the cell is shown in Table 3.3.

Table 3.3: The structure of the two-terminal tandem cell that is used as an input for the 2T tandem module.

Layer	Thickness [μm]
AF2400 [86]	0.093
Porous glass ARC [87]	0.053
Glass with iron (Fe2O3) [88]	3200
Polyolefin-UVT	450
IZO [93]	0.085
SnO2 [94]	0.005
C60	0.007
Perovskite 1.68 eV [95]	0.575
PTAA	0.023
ITO [89]	0.063
n-SiOx (n)	0.020
a-Si (i) [89]	0.009
c-Si, bulk n-type (Rear textured)	160
a-Si (i) [89]	0.006
a-Si (p) [89]	0.012
AZO	0.055
Ag [90]	0.30

The EQE curves and the IV curves of this tandem cell is shown in Figure 3.4. It can be seen that current matching is considered, as the maximum power point current of the top and bottom cells are similar.

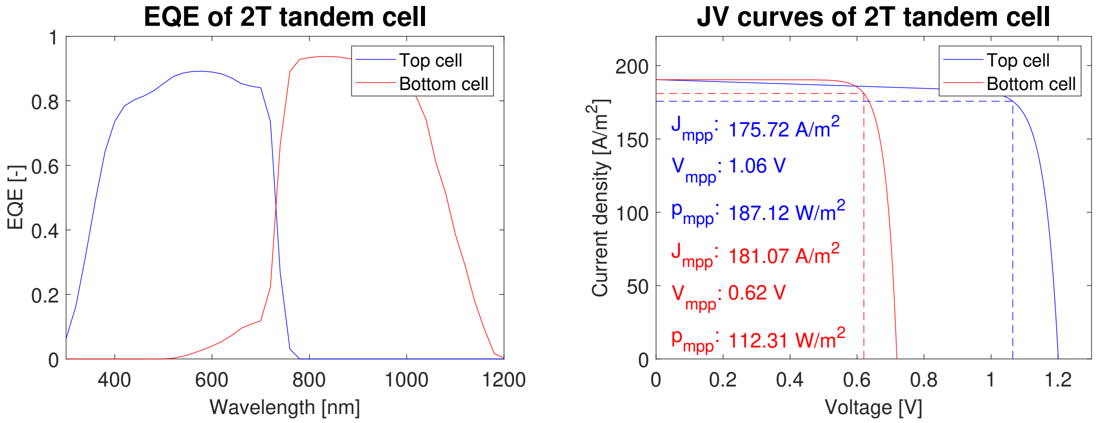

(a) The EQE curve of the two-terminal tandem solar cell

(b) The IV curve of the top and bottom cell for the two-terminal tandem cell

Figure 3.4: The EQE and the IV curve of the tandem solar cell.

3.1.4 The perovskite/silicon three-terminal tandem cell

For the cell design of the 3T tandem cell, many possibilities can be considered. Since the design of a three-terminal tandem cell is not the main focus of this project, the 2T tandem cell will be used as a starting point. However, to fairly compare 2T and 3T tandem cells, some adjustments need to be made. The most important design decisions are discussed in this subsection.

The third contact point

The key principle of 3T tandem cells is that there is a third contact point, such that there can be two different current flows [30, 96–98]. This removes the limitation that the top and bottom cell need to be current matched. The third contact point can be placed in the middle between the top and bottom layer, or at the back side such that the bottom cell becomes an IBC cell. For this project, the third contact point is chosen to be at the back for two reasons:

- The fabrication of a third contact point in the middle is challenging and it can reduce the active device area [97].
- The IBC implementation is more similar to the 2T cell design. Because the design of a 3T tandem cell is not the focus of this project, this implementation is preferred.

Series and reverse connection

Another aspect for three-terminal tandem cells is that the top and bottom cell can be connected in series or reverse connection. The difference between a series connection and reverse connection can be seen in Figure 3.5. In the reverse connection, the current from both the top and bottom cell are coming from the negative back contact and go to their own positive contact. In series connection, the top current flows into the negative contact, whereas the bottom current still flows from the negative bottom contact to the positive bottom contact.

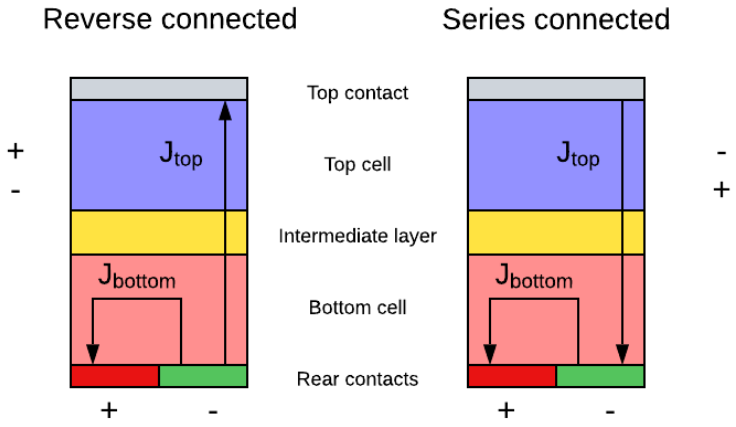

Figure 3.5: The difference between reverse connected (on the left) and series connected (on the right).

There are differences on cell level and on module level. On cell level, the optical performance can change depending in the order of which the materials are stacked. On module level, there is a difference in the mismatch losses when the cells are connected. This is discussed in detail in Section 3.2. The performance of the series and reverse connection are compared in Appendix B.4.

The energy bandgap of perovskite

The main difference between 2T and 3T tandem modules is that 2T tandem cells are current matched, and 3T tandem cells are voltage matched. This means that ratio the operating voltage of the top cell and the operating voltage of the bottom cell is always the same. This ratio can be written as $\frac{m}{n}$ and will from now on be referred as the VM (Voltage Matching) ratio.

To maximise the output power, the ratio of the maximum power point voltage of the top cell and the maximum power point voltage of the bottom cell should be as close to the VM ratio as possible. The maximum power point voltage of the top cell depends on the energy bandgap of the perovskite layer.

Due to limited time and resources, a perovskite material with a bandgap energy of 1.68 eV is chosen. The IV curves of the top and bottom cells are shown in Figure 3.7.

The thickness of the cell perovskite layer

The thickness of the perovskite layer affects the number of absorbed photons. Because current matching is not considered for three-terminal tandem cells, it is desired that the top layer absorbs as much photons as possible. This requires a larger thickness compared to the perovskite layer in the two-terminal tandem cell.

However, a larger thickness will increase the recombination, as electrons and holes need to overcome a greater distance. The chosen thickness of the perovskite layer is 1000 nm, as it is shown in literature that this is optimal thickness for perovskite [28, 99].

The input cell structure

A limitation of PVMD Toolbox is that the cell structure for GenPro4 should be one-dimensional. Therefore, an IBC contact cannot be realised. To simulate a three-terminal tandem cell with the IBC contact, it is assumed that the optical results are the same for both contacts. This assumption is justified in Appendix B.3. The cell structure that is used as input for the Toolbox is shown in Table 3.4.

Table 3.4: The structure of the three-terminal tandem cell that is used as an input for the three-terminal tandem module.

Layer	Thickness [μm]
AF2400 [86]	0.093
Porous glass ARC [87]	0.053
Glass with iron (Fe2O3) [88]	3200
Polyolefin-UVT	450
IZO [93]	0.085
SnO2 [94]	0.005
C60	0.007
Perovskite 1.68 eV [95]	1.000
PTAA	0.023
ITO [89]	0.063
n-SiOx (n)	0.020
a-Si (i) [89]	0.009
c-Si, bulk n-type (Rear textured)	160
a-Si (i) [89]	0.006
a-Si (p) [89]	0.012
AZO	0.055
Ag [90]	0.30

ASA simulation

The perovskite layer that is used for the 3T tandem cell is different than the perovskite layer used for the 2T tandem cell. Therefore, the designed perovskite top cell should be simulated in ASA [56] such that it can be used in the Toolbox. Similar to GenPro4, only one-dimensional structures are allowed as inputs. Therefore, the input structure shown in Table 3.4 is used as input for ASA.

The temperature and irradiance dependence can be obtained from the JV curves under different conditions. These JV curves are shown in Figure 3.6. The temperature ranges from 15°C till 95°C, which is slightly different than the temperature range of the ASA simulations of the normal perovskite top cell. The reason for this, is that the ASA simulation did not converge for low temperatures. However, most energy yield is generated within this temperature range, as shown in Appendix C.7.

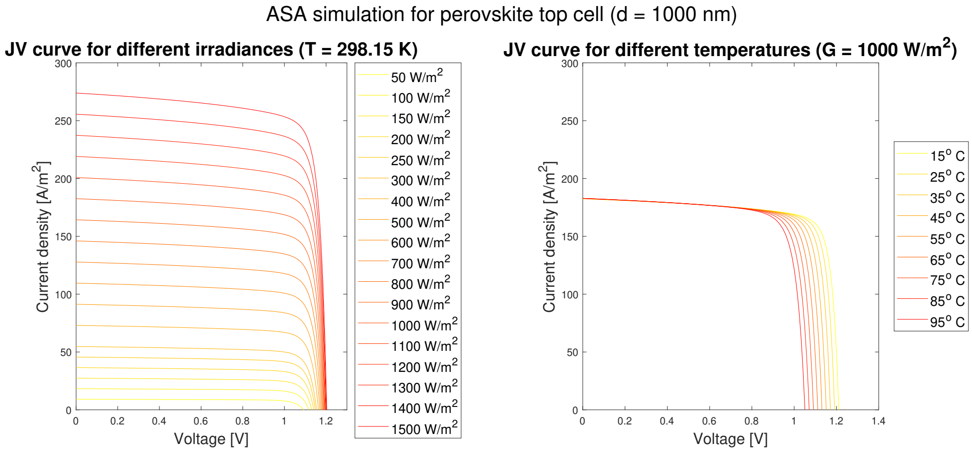

Figure 3.6: The JV curves for different conditions. These curves are used to extract the temperature and irradiance dependencies.

The EQE and the JV curve

The EQE curves and the JV curves of the 3T tandem cell are shown in Figure 3.7. It can be seen that voltage matching is considered, as the maximum power point voltages of both cells are close to the ratio $\frac{m}{n} = \frac{3}{2}$.

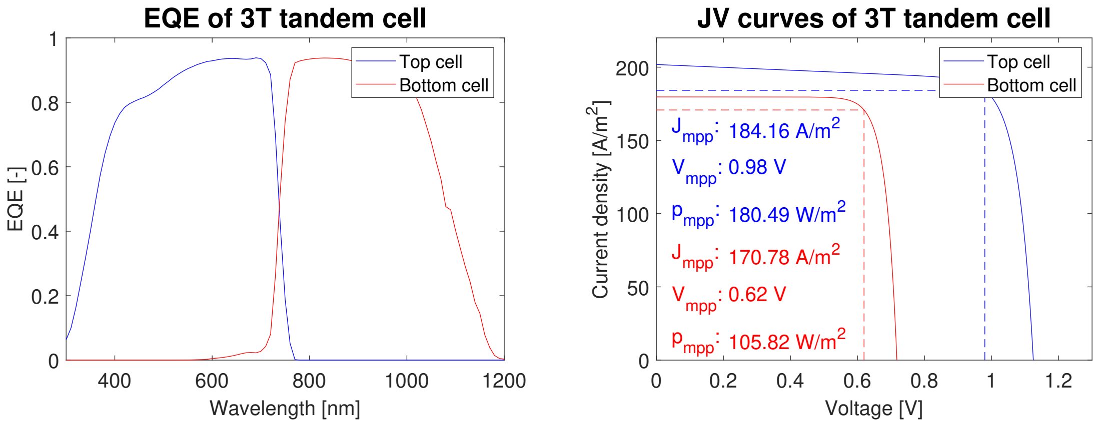

(a) The EQE curve of the 3T tandem solar cell.

(b) The IV curve of the 3T tandem solar cell.

Figure 3.7: The EQE and the IV curve of the 3T tandem solar cell.

The JV curves presented in Figure 3.7 make an assumption that will also be made in the rest of this project. It is assumed that the IV curve of the top cell is not influenced by the operating point of the bottom cell and vice versa. However, in reality the IV curves of a 3T tandem cell are not completely independent [30]. The reason that this assumption is made, is that the Toolbox considers the top and bottom cell as individual cells during the electrical model. Therefore, it is not possible to include the dependence of the IV curves. Therefore, it should be considered that this assumption is made and that the simulated results may differ from reality.

3.2 The design of the modules

For each module, the same system parameters are considered. This includes the area of the cell/ module, the type of interconnection, and the number of cells. The most important parameters are:

- The area of the cell (A_{cell}) is 0.0246 m^2.
- The area of the module (A_{mod}) is 1.89 m^2.
- The number of cells in the module (N_{cells}) is 72.
- The resistance of the interconnection ($R_{intercon}$) is 0.0130 Ω.
- The percentage of shaded area due to metallization is 1.2%.

An important aspect for PV modules is the connection of the cells within the modules. For the mono-facial c-Si module and the bifacial c-Si module all the cells are connected in series. Because these modules consist only of single-junction cells, the implementation of the cell connection relatively simple. A detailed explanation of the implementation in the Toolbox can be found in the thesis of Nour El Din [51].

For the tandem modules, the connection of the cells is important and can influence the output power. Therefore, the connection of the two-terminal and three-terminal tandem modules are discussed separately.

3.2.1 Connection of the two-terminal tandem module

Because a two-terminal tandem cell, by definition, only has two terminals, the top and bottom cell are always connected in series. The electrical behaviour of the cell can be simulated by connecting the five-parameter circuit of both cells to each other. This is shown in Figure 3.8. The connection of the two-terminal tandem cells is implemented with the same method as the single junction modules. This implementation is also discussed in the thesis of Nour el Din [51].

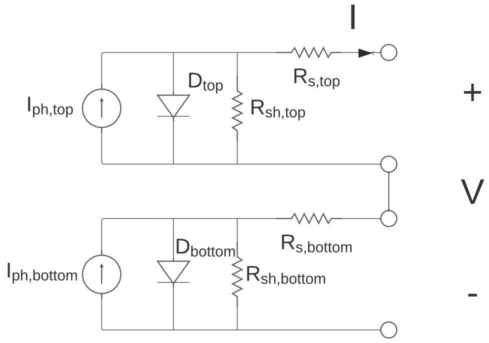

Figure 3.8: The connection of the 2T tandem cell

3.2.2 Connection of the three-terminal module

The cells in a three-terminal module are connected in a different way. Due to the third contact, it is possible to connect the top and bottom cell in parallel. However, the module itself only has two terminals, which means that the connection of the cells is more complicated than for the 2T tandem module. An important parameter for three-terminal is the VM-ratio $\left(\frac{m}{n}\right)$, which indicates that m bottom cells are connected in parallel with n top cells [98]. This also means that the ratio of the operating voltages is equal to

$$\frac{V_{top}}{V_{bottom}} = \frac{m}{n}. \tag{3.2}$$

The connection of the different cells is also determined by the type of connection at cell level (series or reverse). Both the series and reverse module connection are shown in Figure 3.9 and Figure 3.10. In these figures, the VM-ratio is $\frac{2}{1}$.

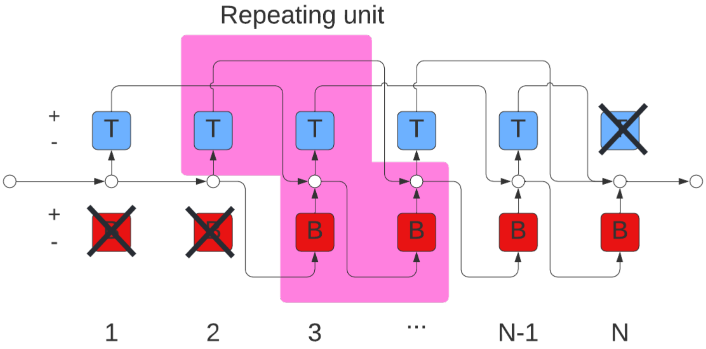

Figure 3.9: The configurations of 3T series connected tandem cells, with the VM ratio of $\frac{2}{1}$. The first two bottom cells and last top cell cannot be used.

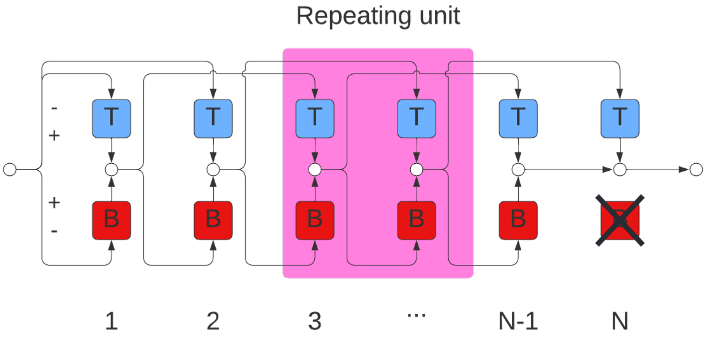

Figure 3.10: The configurations of 3T reverse connected tandem cells, with the VM ratio of $\frac{2}{1}$. The last bottom cell cannot be used.

For the series connection, there are two bottom cells and one top cell, which are not connected. Also, the top cell at position 1 and the top cell at position N-1 are connected in parallel with a bottom cell, which means that both operate at half of the desired voltage. Therefore, it can be argued that this series connection has two non-active cells.

If the tandem cells are reversed, the number of active cells will increase. This is shown in Figure 3.10. In this configuration, the number of active cells is N-1.

In the study performed by McMahon [98], the following relations were defined for the number of active cells (N_{active}) for a 3T module with the VM-ratio $\frac{m}{n}$.

$$\begin{aligned} N_{active} &= N + 1 - (m+n) && \text{for series connection} \\ N_{active} &= N + 1 - \max(m,n) && \text{for reverse connection} \end{aligned} \tag{3.3}$$

Design of the module

On module level, two choices need to be made. The VM-ratio needs to be chosen, and it should be decided whether the cell has a series or reverse connection. Based on the IV curves in Figure 3.7b, the VM-ratio of 3:2 is chosen, since this is close to the ratio of the maximum power point voltages of the top and bottom cell.

The cell connection is chosen based on a comparison of both connections. The series connected module is slightly more efficient than the reverse connected modules, as shown in Appendix B.4. The difference between both modules is that the reverse connected module has more reflection losses, and the series connected module has more mismatch losses. It is discussed by MCMahon [98] that the mismatch losses of 3T tandem modules can be reduced for simple adjustments, such as increasing the number of cells in the module or fabricating heterogeneous cells. Therefore, the series connection is chosen.

3.2.3 Implementation of the 3T tandem module

The current version of the PVMD Toolbox does not contain a developed model for three-terminal modules that considers end losses. Therefore, this implementation will also be discussed in this section. Two different models are designed to simulate the 3T tandem module. The first model is a simplified version and will be referred to as the approximation model. The second model provides a more accurate simulation and will be referred to as the comprehensive model.

The approximation model

The approximation model will be based on the work of McMahon [98]. As discussed before, the VM-ratio indicates the ratio between the operating voltages of the top and bottom cell. The output voltage of the module can be approximated at:

$$V_{module} = N_{active} \cdot \frac{V_{top}}{m} = N_{active} \cdot \frac{V_{bottom}}{n} \tag{3.4}$$

The output current of the module will be the sum of the different paths that are connected in parallel with each other. For a VM-ratio of $\frac{m}{n}$, there will be m paths of top cells and n paths of bottom cells. Therefore, the output current can be approximated at:

$$I_{module} = m \cdot I_{top} + n \cdot I_{bottom} \tag{3.5}$$

The output power of the module can then be modelled as

$$P_{module} = V_{module} \cdot I_{module} \tag{3.6}$$

There are two approximations which are made by this model that simply the calculations:

- It is assumed that each tandem cell receives the same amount of irradiation and will therefore have the same top IV curves and bottom IV curves. If this is not the case, Equation (3.4) would not be valid.
- The end effects at the beginning and the end are neglected. Because the top cell at position 1 and the top cell at position N are operating at a fraction of the normal voltage, they have a different operating voltage. A different operating voltage would typically imply a different operating current. However, it is assumed that the top cells at the ends have the same current as the top cells in the middle of the string.

The comprehensive model

The comprehensive model is used to avoid the assumptions that are made by the approximation model. The central idea of this model is to focus on the voltage of the middle contacts, where the middle contact is the negative rear contact in Figure 3.5. The operating point of each top or bottom cell is completely determined by the voltages at the middle contacts. If the values of the different middle contacts are found for a certain output voltage, the current of the module can be calculated. By varying the output voltage, the IV curve of the model can be created.

The voltages of the middle contacts are calculated by solving a set of equations. Since there are N middle contacts, also N equations need to be defined. These equations will be different for the series connected or reverse connected cells. Since the module will contain series connected cells, only the equations for this type will be discussed. The model for the reverse connection module can be found in Appendix B.1.

To indicate the voltage of a middle point of a certain cell, $V_{middle,x}$ will be used, where x is the index of the cell (ranging from 1 to N). To indicate the voltage over a single top cell or bottom cell, $V_{top,x}$ and $V_{bottom,x}$ will be used respectively. By looking at Figure 3.9, it can be seen that the voltage of the top cells can be written as

$$V_{top,x} = V_{middle,x+m} - V_{middle,x} \qquad \text{if } N - n > x. \tag{3.7}$$

For the voltage over the bottom cells, a similar relation can be defined. Since the first m bottom cells are not connected, there voltage will be undefined. The voltage over a bottom cell can be written as

$$V_{bottom,x} = V_{middle,x} - V_{middle,x-n} \qquad \text{if } m < x. \tag{3.8}$$

The current through each cell can be written as a function of voltage over the cell, as shown in Equation (2.3), which is discussed in Chapter 2. This equation is obtained by solving the voltage current relationship in the five-parameter model. The current of a top cell and bottom cell, will be indicated with $I_{top,x}\left(V_{top,x}\right)$ and $I_{bottom,x}\left(V_{bottom,x}\right)$ respectively.

At each middle point, current is coming in and current is going out. According to Kirchhoff's current law, the incoming current should equal the outgoing current. This law can be used to create equations. For $m < x < N - n$ the following holds:

$$I_{top,x-m}\left(V_{top,x-m}\right) + I_{bottom,x}\left(V_{bottom,x}\right) = I_{top,x}\left(V_{top,x}\right) + I_{bottom,x+n}\left(V_{bottom,x+n}\right). \tag{3.9}$$

The last $n+m$ equations that are needed to complete the set of N equations will come from the first m and last n middle points. Since the first m middle points are connected to the negative terminal of the module, those can be set to 0. This can be written as

$$V_{middle,x} = 0 \qquad \text{if } m \geq x. \tag{3.10}$$

Since the last n middle points are all connected to the output, it can be defined that

$$V_{middle,x} = V_{out} \qquad \text{if } x \geq N - n. \tag{3.11}$$

As mentioned before, V_{out} is a parameter that will be varied to create the IV curve of the module. The system of equations will be solved with the MATLAB function *vpasolve* [100].

Validation of the models

To validate the different models, a 3T tandem module is simulated in LTspice. The IV curve of both models and the LTspice simulation are shown in Figure 3.11 and the important electrical parameters are shown in Table 3.5. All models show similar results, indicating that the approximation model is accurate. Because the comprehensive model takes more computation time than the approximation model, the approximation is used in the Toolbox.

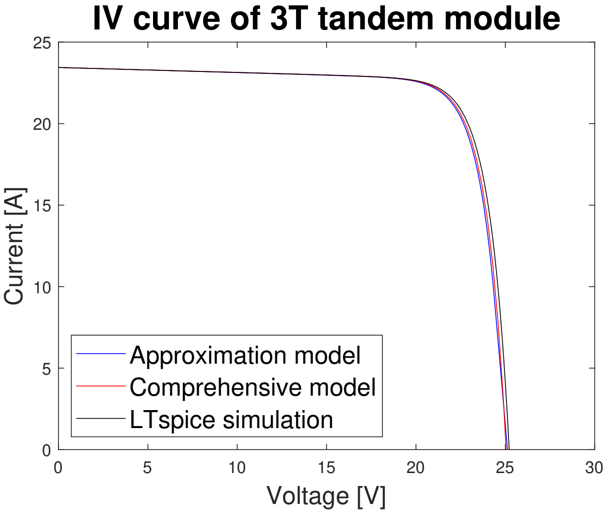

Figure 3.11: The IV curve of the different models. It can be seen that the three curves are similar.

Table 3.5: The electrical parameters for the different models.

Model	I_{sc} [A]	V_{oc} [V]	P_{mpp} [W]	FF [-]	I_{mpp} [A]	V_{mpp} [V]
Approximation	23.4	25.1	470	0.797	21.7	21.6
Comprehensive	23.4	24.9	472	0.808	21.8	21.6
LT spice	23.4	25.2	475	0.804	21.7	21.9

3.2.4 The module IV curves

The IV curves of all the modules are shown in Figure 3.12. It can be seen that the 2T tandem module has the highest efficiency (27.7%), followed by the 3T tandem module (24.6%), the monofacial c-Si module (20.9%), and the bifacial c-Si module (20.8%). An important difference between the two-terminal and three-terminal tandem module, is that the two-terminal tandem module has a higher voltage, and the three-terminal tandem module has a higher current. This is because all cells in the 2T tandem module are connected in series, whereas the cells in the 3T tandem module are connected in a combination of series and parallel.

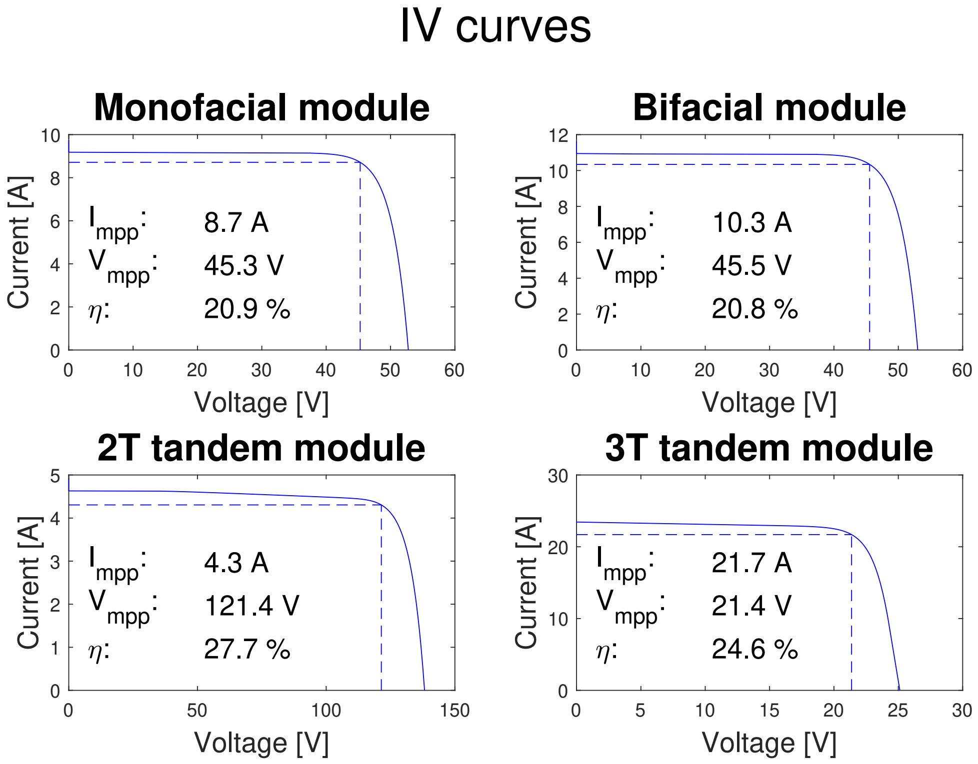

Figure 3.12: The IV curves of the different modules.

3.3 Results and comparison between modules at STC

The results for the different modules are shown in Figure 3.13 and Figure 3.14. The next step is to compare the loss distributions of the modules and analyse the differences. In this section, the four different modules will be compared with each other. This comparison will be done per category. It should be noted that if stated that certain losses increase or decrease with x%, this is meant as an absolute increase in percentage points, not as a relative increase.

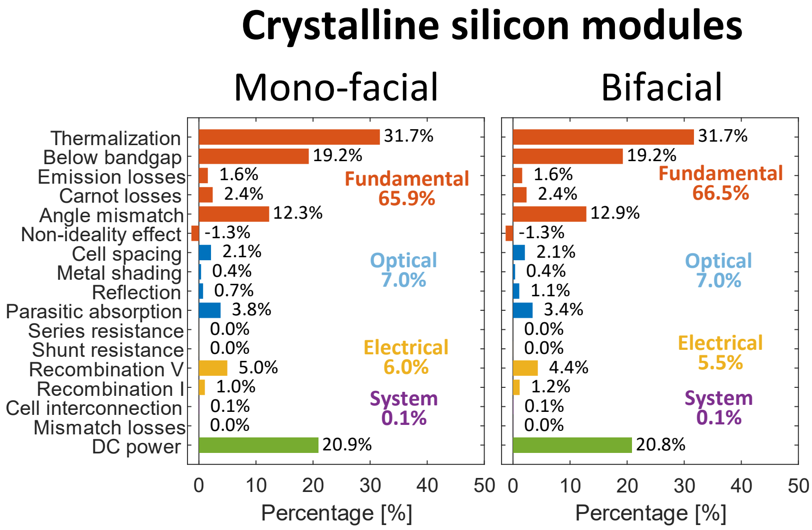

Figure 3.13: The results of the mono-facial and bifacial module.

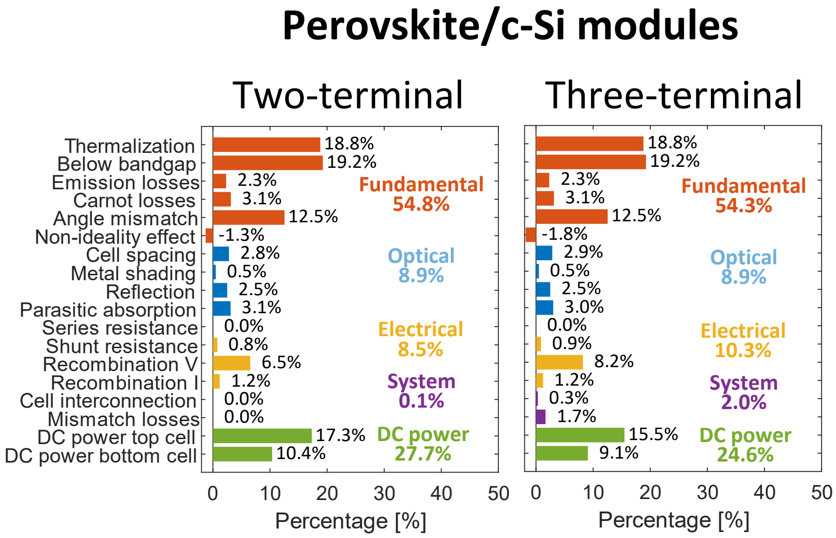

Figure 3.14: The results of the 2T and 3T tandem module.

3.3.1 Fundamental losses

An overview of the fundamental losses in the different modules is presented in Table 3.6. The fundamental losses of the mono-facial and bifacial module are similar, and those of the 2T tandem and 3T are the same. The differences between the four modules are caused by three phenomena: multiple/ different band gaps, a different solid state of emission, and a better EQE for the top cell.

Table 3.6: A comparison of the fundamental losses of the four different modules

	Mono-facial c-Si	Bifacial c-Si	Tandem 2T perov/c-Si	Tandem 3T perov/c-Si
Thermalization [%]	31.7	31.7	18.8	18.8
Below bandgap [%]	19.2	19.2	19.2	19.2
Emission losses [%]	1.6	1.6	2.3	2.3
Carnot losses [%]	2.4	2.4	3.1	3.1
Angle mismatch [%]	12.3	12.9	12.5	12.5
Non-ideality effect [%]	-1.3	-1.3	-1.3	-1.8

Differences due to multiple band gaps

The biggest difference between the single junction and the tandem module is the decrease in thermalization losses. As explained in Section 1.2, tandem PV is designed to use more energy from the high-energy photons, which causes this decrease.

Another effect of a different bandgap energy is that the Carnot losses change, as shown by Equation (2.16). Because the Carnot voltage difference is dependent of the bandgap energy, the Carnot losses increase for a higher bandgap. Since tandem PV contain two different band gaps, the Carnot losses have increased 0.7%-0.9% compared to single junction modules.

The number of emitted photons is dependent on the applied cell voltage(Equation (2.9)). The top cell (with the higher bandgap energy) has a larger voltage, resulting in more emitted photons. This makes the emission losses increase from 1.6% for mono-facial modules to 2.3% for tandem modules.

Difference due to a different solid angle

Bifacial solar cells have a solid angle of emission that is twice as large as mono-facial solar cells. This leads to a larger angle mismatch voltage, causing an increase of 0.6% in the angle mismatch loss compared to the mono-facial c-Si module.

A better EQE for the top cell

The 3T tandem module has a better EQE for the top cell, due to the thicker perovskite layer. This means that more high energy photons are absorbed in the top cell, compared to the 2T tandem module. When a high energy photon is absorbed in the bottom cell instead of the top cell (due to a non-perfect EQE), there are more thermalization losses. The non-ideality factor accounts for this underestimation of the thermalization losses. Because the 3T tandem cell has a better EQE, less high energy photons are absorbed in the bottom cell, leading to a lower underestimation of the thermalization losses. This causes a difference of 0.5% in the non-ideality factor.

3.3.2 Optical losses

The optical losses of the different modules are presented in Table 3.7. Similar to the fundamental losses, the results for the mono-facial and bifacial module are close to each other, and the results for the 2T and 3T tandem modules are almost the same. The differences in results are due to the following two causes: lower fundamental losses for tandem modules, and the different cell structures.

Table 3.7: A comparison of the optical losses of the four different modules

	Mono-facial c-Si	Bifacial c-Si	Tandem 2T perov/c-Si	Tandem 3T perov/c-Si
Cell spacing [%]	2.1	2.1	2.8	2.9
Metal shading [%]	0.4	0.4	0.5	0.5
Reflection [%]	0.7	1.1	2.5	2.5
Parasitic absorption [%]	3.8	3.4	3.1	3.0

Lower fundamental losses for tandem modules

The cell-spacing and metallization losses both contain the term $(P_{in} - P_{fund})$. This term increases as a result of lower fundamental losses for tandem modules (as shown in Table 3.6). Therefore, the cell-spacing and metallization losses are larger for tandem modules than for the single junction modules.

A different cell structure

The cell structures of the different modules are discussed in the previous sections of this chapter. Each material has different optical parameters, which can cause a difference in reflection/transmission and parasitic absorption. Although there are many differences that can be discussed, only two important differences will be highlighted.

The difference in reflection/transmission losses between the mono-facial and bifacial module is because bifacial cells do not have a back reflector. Therefore, photons that would be reflected by the back contact, can now be transmitted through the solar cell. This causes the increase of the reflection/transmission losses.

An important difference between the single junction cells and tandem cells is that the single junction cells have double texturing, whereas tandem cells only have rear texturing. Front texturing is designed to reduce the reflection, due to its pyramid shape. Since tandem cells do not have front texturing, their reflection losses increase.

3.3.3 Electrical losses

An overview of the electrical losses is shown in Table 3.8. The differences between the modules are due to the different materials that are used and different levels of irradiances.

Table 3.8: A comparison of the electrical losses of the four different modules.

	Mono-facial c-Si	Bifacial c-Si	Tandem 2T perov/c-Si	Tandem 3T perov/c-Si
Series resistance [%]	0.0	0.0	0.0	0.0
Shunt resistance [%]	0.0	0.0	0.8	0.9
Voltage recombination [%]	5.0	4.4	6.5	8.2
Current recombination [%]	1.0	1.2	1.2	1.2

Different materials

The tandem cells and the silicon cells are made of different materials, which means that the values of the electrical parameter are also different. The values of the parameters for different photo generated currents are shown in Appendix B.2. Because perovskite has a smaller shunt resistance, there is more leakage current. Therefore, the shunt resistance losses increase with 0.8%-0.9% for both tandem modules

Also, perovskite has a larger value for the ideality factor n. A larger value of the ideality factor lowers the MPP voltage, since there is a greater dependence between the recombination current and the output voltage. Therefore, the difference between the MPP voltage and the optimal voltage increases. Because the non-radiative recombination voltage losses depend on this difference (shown in Equation (2.30)), this loss increases for the tandem modules.

There is also a large difference between the 2T and the 3T tandem module. Due to the thicker layer of perovskite, the 3T tandem cell has more recombination, leading to a larger value for the ideality factor and the saturation current. This causes the increase in recombination losses for the 3T tandem module.

Different irradiances

The bifacial module is simulated under B-STC, whereas the mono-facial modules are simulated under STC. Since B-STC has a higher irradiance, bifacial cells have a larger photo generated current. This reduces the recombination since the ideality factor and the saturation current density depend on the photo generated current (Appendix B.2).

3.3.4 System losses

The last category is the system losses. The results of this category are shown in Table 3.9. The differences for the system losses can be explained by two different causes: the output current, and the configuration.

Table 3.9: A comparison of the electrical losses of the four different modules

	Mono-facial c-Si	Bifacial c-Si	Tandem 2T perov/c-Si	Tandem 3T perov/c-Si
Cell interconnection [%]	0.1	0.1	0.0	0.3
Mismatch losses [%]	0.0	0.0	0.0	1.7

The output current

The interconnection losses depend on the output current since a higher current leads to more ohmic losses. For the 2T tandem module, the output current is lower, since the irradiation is divided over the top and bottom cell, and all cells are connected in series. Therefore, the interconnection losses decrease for the 2T tandem module. For the 3T tandem module, there is a higher output current, leading to an increase of interconnection losses.

The configuration

Mismatch losses occur if the solar cells within a module cannot operate on their maximum power point. The operating point of the individual solar cells is determined by the configuration of the module. For the single-junction modules, all cells can operate on their maximum power point, and therefore there are no mismatch losses.

For the 2T tandem module, the top and bottom cells need to be current matched, as they are connected in series. Because the top and bottom cells are almost current matched (as shown in Figure 3.4b), there are no significant mismatch losses.

For the 3T tandem, there are significantly more mismatch losses. This is caused by the non-active solar cells. In a 3:2 series connection, there are four non-active cells, which already cause a loss of $\frac{4}{72}$ compared to the generated electricity. This means that there are approximately 1.5% ($\frac{4}{72} \cdot \eta$) mismatch losses due to the non-active cells.

3.4 Conclusion

The second sub-goal of this work is to quantify the loss distribution at STC. This chapter has presented the loss distributions for four different PV modules under STC. An overview of these results is shown in Figure 3.13 and Figure 3.14. As expected, tandem modules have a higher efficiency compared to single junction modules, which is mostly due to a reduction of the thermalization losses. However, the resistance and recombination losses increase for tandem modules, since the perovskite top cell has more resistance and recombination losses compared to the silicon cell.

Additionally, mono-facial modules are compared to bifacial modules. The efficiency for mono-facial module is slightly larger than bifacial modules due to lower angle mismatch losses. However, the actual power generation is larger for bifacial modules due to the additional rear side irradiance.

Additionally, the loss distribution of a 2T tandem module is compared to that of a 3T tandem module. This required to design an electrical model of a 3T module, as this was not included in the PVMD Toolbox. The simulations show that 3T tandem modules have significantly more mismatch losses. This is because the 3T tandem module has more non-active cells, which create mismatch losses. Also, the greater thickness for the perovskite cell in the 3T module resulting in more recombination. Overall, the efficiency of the 2T module is 3.1% larger than the efficiency of the 3T module.

The next chapter will analyse the annual loss distribution for the same modules under realistic operating conditions.

4. Loss analysis for real world operating conditions

The third sub-goal of this study is to analyse the loss distributions of the PV modules under realistic operating conditions. In this chapter, the modules described in Chapter 3 will be simulated at four locations. Using the equations defined in Chapter 2, the loss distributions are calculated.

First, the model used for calculating the incoming irradiance, is explained. This model is needed since this is not provided by the Toolbox itself. After this, the four locations will be discussed, and the differences will be highlighted. Then, the results for the modules will be discussed individually in the order: mono-facial crystalline module, bifacial crystalline module, the 2T tandem module, and the 3T tandem module. This is followed by a comparison among the different modules. After the results, the upper limits of the different modules under different locations will be discussed and compared with the upper limit at test conditions. Finally, the conclusion and recommendations of this chapter are presented.

4.1 The irradiance model

To calculate the loss analysis of a given PV system, it is crucial to know the incoming power. The absorbed power is calculated in the ray tracing model and the irradiance model. However, this model does not calculate the total in-plane irradiation. Therefore, a simple irradiance model is constructed to calculate the in-plane irradiance on the module. The calculated irradiance is then corrected based on calculations from the Toolbox. An important assumption is that the irradiance on all the cells is the same for every cell. The reasoning behind this assumption is explained in Appendix C.1.

The irradiance model of the Toolbox uses the SMARTS model [101], which can simulate the spectral irradiance. However, this spectral irradiance does not consider cloud coverage, which typically has an effect on the spectral distribution. This is more discussed in Chapter 6.

4.1.1 The simple model for incoming irradiance

The irradiance model used for the loss analysis is based on Perez model, similar to the actual irradiance model of the Toolbox. By using Perez model, the irradiance for each position in sky can be modelled based on the direct normal irradiance (DNI), diffuse horizontal irradiance (DHI), and the position of the sun. In the irradiation model, the sky is divided into 160 vertices, such that the irradiance for each vertex can be calculated. For each vertex, the Angle of Incidence (AOI) can be calculated, which is important for the in-plane irradiance. The irradiance from a certain vertex is calculated by multiplying the total irradiance from this vertex with the cosine of the angle of incidence. The total incoming power can then be calculated as

$$P_{in} = \sum_{i=1}^{160} I_i \cdot \max\left[\cos(AOI_i), 0\right], \tag{4.1}$$

where I_i is the irradiance coming from vertex i. The term $\max\left[\cos(AOI), 0\right]$ is used, such that only vertices that can directly reach the module are included.

A limitation of this simplified model is that it does not consider albedo reflection. The reason for this is that it is unknown in which direction light travels from a given vertex. Therefore, the assumption is made, that all the light from a vertex travels directly to the module.

4.1.2 Correction

The model described above uses a different method than the model of the Toolbox, which can cause deviations in the absorbed current density. To make the model of the loss analysis more consistent, a correction is done. The absorbed current density of the simplified model ($J_{abs,sim}$) can be calculated with the incoming photon flux from the vertices and the EQE of the solar cell for different angles, written as

$$J_{abs,sim} = \sum_{i=1}^{160} \left(\int_0^{\lambda_g} q \cdot \phi_i(\lambda) \cdot EQE\,(AOI_i)\, d\lambda \right) \max\left[\cos(AOI_i), 0\right]. \tag{4.2}$$

The correction factor is then defined as the ratio of the absorbed current density of the Toolbox ($J_{abs,tb}$) over the absorbed current density of the model. This correction factor is based on the work of Schmager et al [102]. The incoming irradiance of a given vertex is them multiplied with this factor. This can be written as:

$$I_{i,cor} = I_{i,org} \cdot \frac{J_{abs,tb}}{J_{abs,sim}}, \tag{4.3}$$

where $I_{i,cor}$ and $I_{i,org}$ are the corrected and original irradiance from vertex i respectively. The corrected irradiance can then be used to calculate the incoming power with Equation (4.1). The irradiance weighted correction coefficient for each climate is shown in Table 4.1. The correction is the largest in Delft and Shanghai. However, for all locations, the correction is approximately 1.04 for all locations, indicating that the error is smaller than 5%.

Location	Delft	Lisbon	Lagos	Shanghai
Correction factor	1.042	1.038	1.041	1.042

Table 4.1: The irradiance weighted correction factor for each factor. The error at each location is smaller than 5%.

The model for bifacial irradiance

For bifacial modules, the irradiance can come from both sides of the PV module. This makes the model for the incoming irradiance more complicated, especially since ignoring albedo reflection would be an invalid assumption. Therefore, a different model has been defined for bifacial modules, and it is discussed in Appendix C.2.

4.2 The different climates

The four different modules are simulated at four different climates. For each climate, a geographical location is selected, that will represent this climate. The locations are:

1. Delft (the Netherlands), representing temperate low irradiance climates.
2. Lisbon (Portugal), representing temperate high irradiance climates.
3. Lagos (Nigeria), representing tropical high irradiance climates.
4. Shanghai (China), representing temperate medium irradiance climates.

The hourly climate data of the different locations is extracted from METEONORM version 7.3 [103]. Table 4.2 shows the most important annual climate parameters, which are the annual global horizontal irradiation (GHI), the mean annual ambient temperature (T_A), the mean annual wind speed (WS), and the Köppen-Geiger-Photovoltaic (KGPV) classification [104, 105]. Also,

Table 4.2: The most important climate parameters of the four locations. Also, the locations are classified according to the KGPV classification.

Location	Annual in-plane irradiation [kWh·m^{-2}]	Mean annual T_A [^{o}C]	Mean annual WS [m·s^{-1}]	KGPV	Optimum tilt [^{o}]
Delft	1127	10.8	4.0	DL	31
Lisbon	1575	16.7	3.6	DH	28
Lagos	1909	27.5	3.9	AH	5
Shanghai	1284	17.5	3.5	DM	17

the optimum tilt of the module is shown, which has been determined by previous work on the Toolbox [41].

Besides the total in-plane irradiation, it is also important to know what the spectral distribution is, and what levels of irradiance occur most often. Figure 4.1 shows the normalized distribution of the air mass. The distribution is irradiance weighted, and it can be seen that most incoming power is received with a lower air mass than 1.5 (air mass at standard test conditions). This means that there will be a small blue shift in the spectrum. It should be noted that these values are simulated with SMARTS [101], and this might differ from reality.

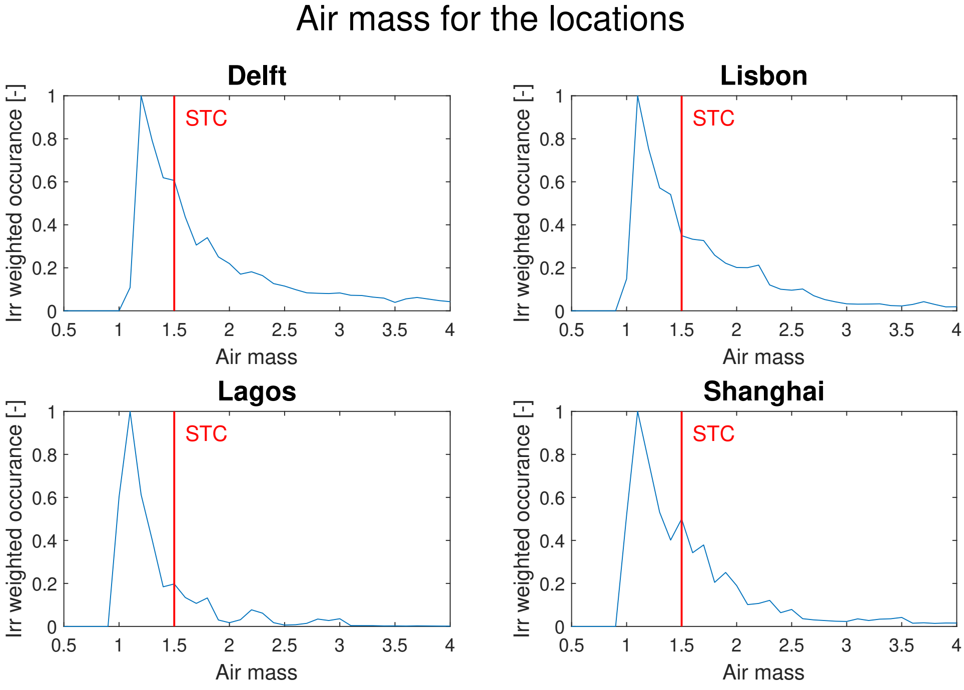

Figure 4.1: The normalized distribution of the air mass of the different climates. The red line is the air mass corresponding to the STC spectrum

Figure 4.2 shows the normalized distribution of the different irradiance levels. In Delft and Shanghai, low levels of irradiance happen more often compared to Lagos and Lisbon. These values are also irradiance weighted.

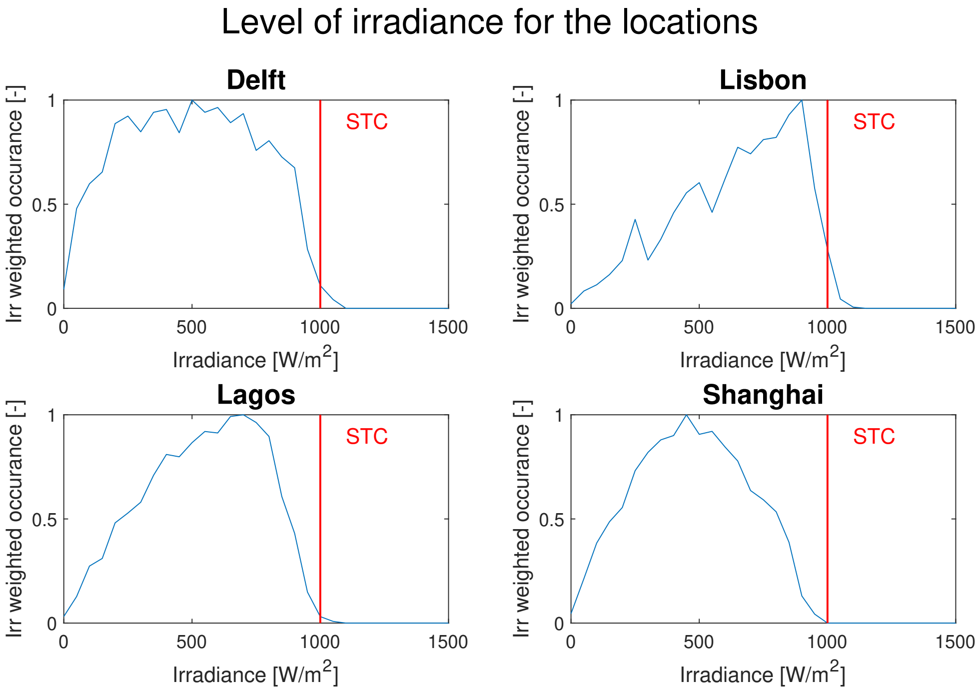

Figure 4.2: The normalized distribution of the irradiance level of the different climates. The red line is the irradiance level corresponding to the STC spectrum

4.3 The results for the mono-facial c-Si module

This section presents the loss distribution for the mono-facial module. The results of the bifacial, two-terminal, and three-terminal module will be presented in the next sections. A full discussion about the loss distribution can be found in Appendix C.3. In this section, only the significant changes compared to STC will be discussed.

The results for the mono-facial module are shown in Figure 4.3. The calculations are performed for each hour and combined into an annual loss distribution. This means that hourly, daily, or seasonally variations could also be analysed. This could be used to see how the losses vary for different moments of the day or different moments of the year. However, due to limited time only the annual results are analysed.

The main results are summarized in Table 4.3. The greatest DC-efficiency is achieved in Delft, mostly due to slightly lower fundamental losses. The greatest energy yield is achieved in Lisbon, due to the high irradiation.

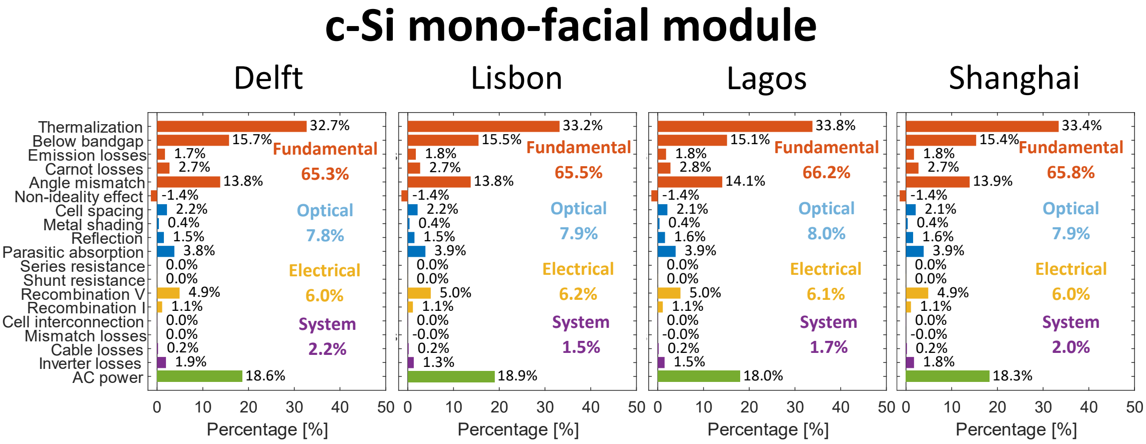

Figure 4.3: The results of the mono-facial module for the different locations.

Table 4.3: The most important results for the mono-facial crystalline silicon module.

	Delft	Lisbon	Lagos	Shanghai	STC
DC efficiency [%]	20.7	20.4	19.7	20.3	20.9
AC Energy yield [MWh]	1.99	3.41	2.68	2.22	-

An important difference between outdoors conditions and STC, is the spectral variation in incoming irradiance. At real-world operating conditions, the irradiance is blue-shifted compared to STC, since the (irradiance weighted) air mass is lower than 1.5 for all locations (see Figure 4.1). This leads to an increase of thermalization and a decrease of below bandgap losses. The thermalization losses increase from 31.7% at STC to 32.7%-33.8% at outdoors conditions, and the below bandgap losses decrease from 19.2% to 15.1%-15.7%. The blue shift is the largest in Lagos, as this location has the lowest air mass, explaining why the difference is the largest in Lagos.

Another difference is that the amount of in-plane irradiance is typically lower at outdoors conditions than at STC. This results in lower optimal voltage. Therefore, the Carnot voltage and the angle mismatch voltage increase, as they are the difference between the optimal voltage and $\frac{E_g}{q}$. Therefore, the Carnot and angle mismatch losses increase from 2.4% and 12.3% at STC to 2.7%-2.8% and 13.8%-14.1% at real-world operating conditions respectively.

For the optical losses, only the reflection losses change significantly. Because irradiance is reaching the module at more oblique angles, the reflection increases. Therefore, the reflection losses increase from 0.7% at STC to 1.5%-1.6% at outdoors locations.

Finally, the output power varies among the different locations. Since the efficiency of the inverter depends on the output voltage and current, the inverter will be more efficient for Lisbon and Lagos, as they have larger power outputs. This causes the inverter losses to be lower in Lisbon and Lagos.

4.4 The results for the bifacial c-Si module

The bifacial module is also simulated for every hour of the year at four different locations. The loss distributions for this module are shown in Figure 4.4.

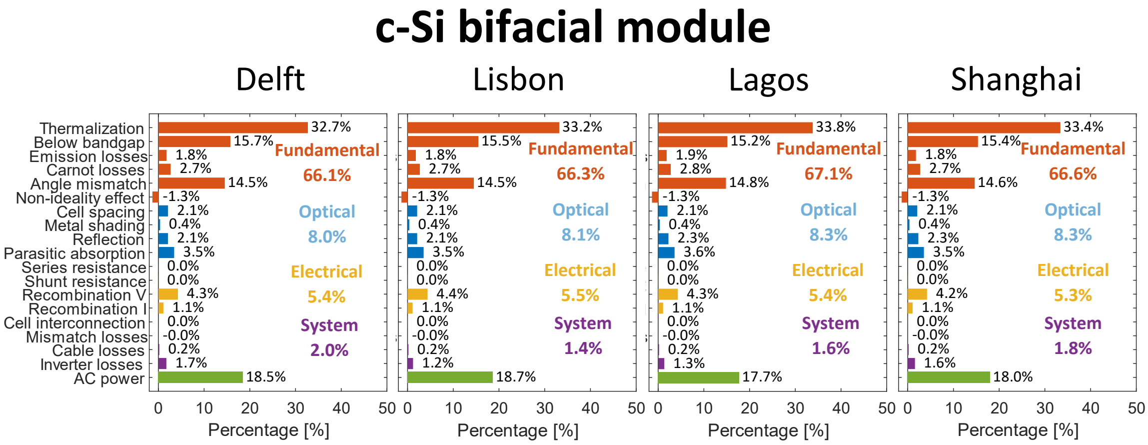

Figure 4.4: The results of the bifacial module for the different locations.

The most important results of the simulations are shown in Table 4.4. Similar to the mono-facial module, the module located in Delft has the highest DC-efficiency (due to lower fundamental losses), and the module located in Lisbon has the largest energy yield (due to more irradiance).

Table 4.4: The most important results for the bifacial crystalline silicon module.

	Delft	Lisbon	Lagos	Shanghai	B-STC
DC efficiency [%]	20.4	20.1	19.2	19.8	20.8
AC Energy yield [MWh]	2.26	3.83	2.99	2.51	-

The results of the bifacial module follow similar trends as the mono-facial module. Due to a blue shift of the spectrum, the thermalization losses increase from 31.7% at STC to 32.7%-33.8% at real-world operating conditions, and the below bandgap losses decrease from 19.2% to 15.2% to 15.7%.

A difference compared to the mono-facial module, is that the angle mismatch losses are higher. Bifacial cells have a larger solid angle of emission, leading to more emission. This causes an increase of the angle mismatch voltage, leading to a higher loss compared to the mono-facial module.

Similar to the mono-facial modules, the inverter losses vary due to different inverter efficiencies. However, the inverter losses are slightly smaller than the mono-facial module, since the bifacial modules have a higher output power.

4.5 The results for the 2T tandem module

The next module that will be discussed is the two-terminal tandem module, whose structure is shown in Section 3.1. The perovskite layer has a thickness of 575 nm, as this optimises the performance under STC. The annual loss distributions of this module are shown in Figure 4.5.

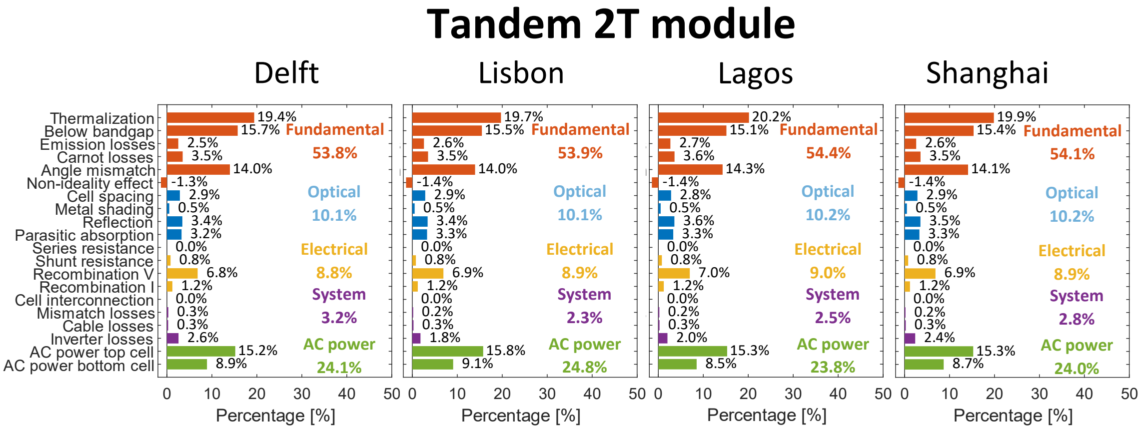

Figure 4.5: The results of the two-terminal tandem module for the different locations.

The most important results are summarised in Table 4.5. Similar to the other modules, the greatest energy yield is achieved in Lisbon. The tandem module located in Delft has the greatest DC-efficiency, which is mostly due to lower fundamental thermalization losses. A difference compared to the c-Si modules is that the difference between STC and real-world operating conditions is more significant than for c-Si modules.

Table 4.5: The most important results for the 2T tandem perovskite/silicon module.

	Delft	Lisbon	Lagos	Shanghai	STC
DC efficiency [%]	27.0	26.9	26.1	26.7	27.7
AC Energy yield [MWh]	2.56	4.47	3.54	2.90	-

For the fundamental losses, the similar effects as for the single junction modules can be seen. The thermalization losses increase from 18.8% at STC to 19.4%-20.2% at real-world operating conditions, and the below bandgap losses decrease from 19.2% to 15.1%-15.7%. This is a result of the blue shift in the spectrum.

There is also less incoming irradiance compared to standard test conditions, which leads to a lower optimal voltage. This results in a higher Carnot and angle mismatch voltage loss. The Carnot and angle mismatch losses increase from 3.1% and 12.5% at STC to 3.5%-3.6% and 14.0%-14.3% at outdoors conditions, respectively.

Similar to the crystalline silicon modules, the incoming photons reaches the module at more oblique angles compared to STC. This makes the reflection increase from 2.5% at STC to 3.4%-3.6%.

A difference compared to the crystalline-silicon modules is the significant increase in recombination losses. The saturation current density and the ideality factor of the perovskite cell increase for a higher temperature as shown in Appendix B.2. The cell temperatures are higher at real-world operating conditions compared to STC (shown in Appendix C.7), leading to more recombination losses. The voltage recombination loss increases from 6.5% at STC to 6.8%-7.0% outdoors. This difference is the highest in Lagos, since the cell temperatures are the highest at this location.

The mismatch losses increase from 0.0% at STC to 0.2%-0.3% at real-world operating conditions, which means that the current mismatch does not cause significant power losses. This is due to the fill factor gain, and is explained more deeply later this section.

The inverter losses show a similar trend as found before. The locations with lower output powers have a larger inverter loss, due to a lower inverter efficiency.

The fill factor gain

The mismatch losses are larger at outdoors conditions than at test conditions. This is expected according to literature [106]. However, the actual power mismatch loss is not as much as the current mismatch indicates, which is due to the so-called fill factor gain. This is the effect that the fill factor can increase if the IV curves of the top and bottom cell are not matched, which is shown in Figure 4.6. The IV curve of the unmatched tandem cell is steeper compared to the matched cell, indicating that the fill factor has increased.

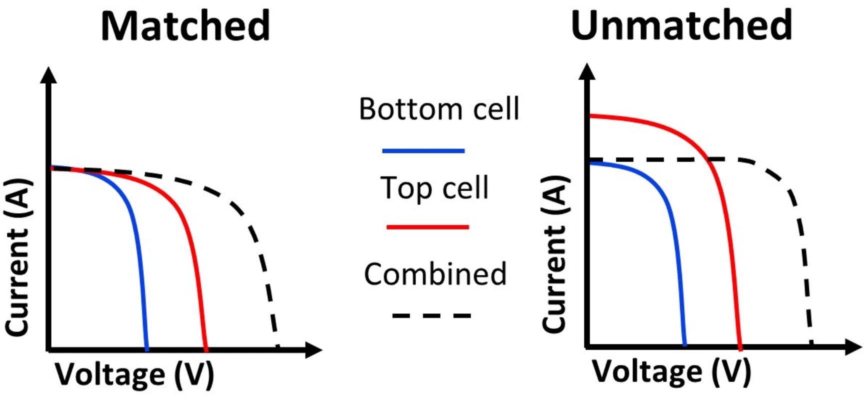

Figure 4.6: The fill factor of the tandem cell can increase when the cells are not current matched.

In Table 4.6, the current mismatch and the fill factor are shown for the different locations. For the locations where the absorbed current mismatch is large, the fill factor increases. This limits a mismatch in power, where the power mismatch is defined as the relative difference between the power when operating at four-terminal (P_{4T}) and the power when operating at two-terminal (P_{2T}).

Table 4.6: The fill factor increases when there is a greater current mismatch. The current mismatch is calculated as the difference in I_{ph} compared to absorbed current in the bottom cell. The power mismatch is defined as $\frac{P_{4T}-P_{2T}}{P_{2T}}$.

	Delft	Lisbon	Lagos	Shanghai	STC
Current mismatch [%]	7.03	6.25	8.11	6.87	0.18
Fill factor [-]	0.824	0.828	0.838	0.832	0.817
Power mismatch [%]	1.17	0.76	0.86	0.80	0.20

Figure 4.7 shows the normalised distribution of the fill factor, weighted according to the generated AC energy yield. The fill factors for all moments in time are discretized in steps of 0.001, and for each interval the AC energy yield is added together, to see which fill factors occur most often. It can be seen that for all locations, most of the AC energy is generated at a fill factor larger than the fill factor at STC.

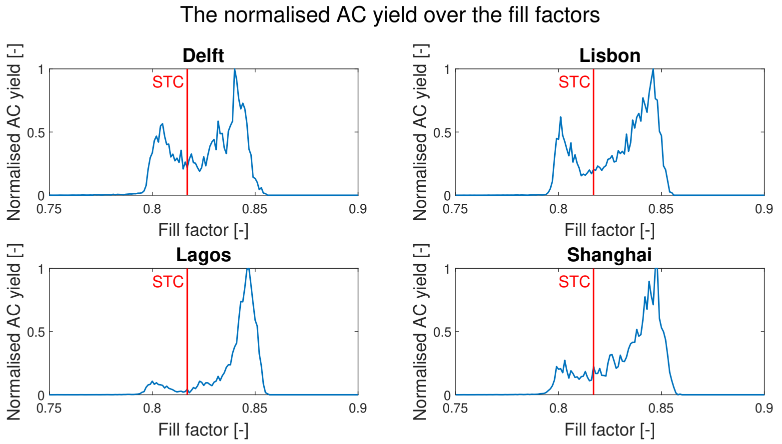

Figure 4.7: The normalized distributions of the fill factor for all locations, weighted with the generated AC energy yield. The red line indicates the fill factor at STC.

Another illustration of the fill factor gain can be seen in Figure 4.8. This figure shows the normalised distribution of the current mismatch (top graph) and the power mismatch (bottom graph) over the different fill factors. The distribution of the current mismatch is calculated by adding the current mismatches that occur at the same fill factor. First, the fill factors at all moments in time are discretized in steps of 0.001. Then, a range of all possible fill factors is created, ranging from 0 to 1, with an interval of 0.001. Each possible fill factor is denoted with FF_i, where $0 < i < 1000$. The current mismatch at fill factor FF_i, denoted with ΔI_i, can be calculated with

$$\Delta I_i = \sum_{t \in T, FF_t = FF_i} |I_{ph,top,t} - I_{ph,bot,t}|. \tag{4.4}$$

In this equation, t is an hour in the year, T is the collection of all hours in the year, FF_t is the fill factor at time t, and $|I_{ph,top,t} - I_{ph,bot,t}|$ is the absolute current mismatch at time t. The condition $FF_t = FF_i$ is used, such that only the hours with a fill factor equal to FF_i are added at index i. Finally, all values are normalised by dividing by the maximum value, resulting in the top graph shown in Figure 4.6.

The distribution of the power mismatch is calculated with a similar equation. The power mismatch at a fill factor FF_i is denoted with ΔP_i and is calculated with

$$\Delta P_i = \sum_{t \in T, FF_t = FF_i} |P_{4T,t} - P_{2T,t}|, \tag{4.5}$$

where $P_{4T,t}$ is the power output at time t if it would operate as four terminal tandem, and $P_{2T,t}$ is actual power output at time t (as the module operates as two terminal tandem). Also, these values are normalised by dividing by the maximum value.

The current mismatch has a peak at a lower fill factor compared to STC, and a peak at a higher fill factor compared to STC. However, the power mismatch only has a peak at a lower fill factor. This indicates that the current mismatch can be compensated if the fill factor is relatively high. In this figure, only the current mismatch and power mismatch of Delft are shown, but a similar trend can be seen for other locations. Delft is shown, as this location provided the clearest illustration.

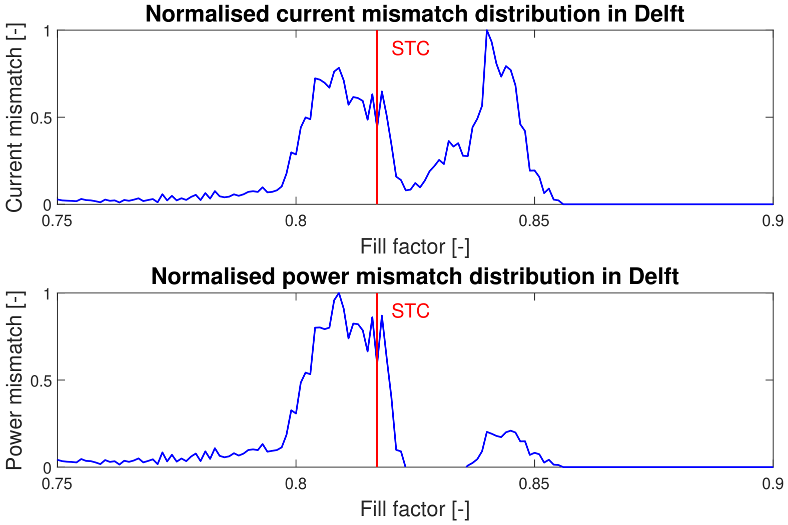

Figure 4.8: An illustration of the fill factor gain. The top graph shows the normalized distribution of the current mismatch over different fill factors, whereas the bottom graph shows the distribution of the power mismatch over the different fill factors.

4.6 The results for the 3T tandem module

The last module that is simulated is the three-terminal tandem module, whose structure is described in Section 3.1. The thickness of the perovskite layer is 1000 nm, which is thicker than the perovskite layer of the two-terminal tandem cell. The results of the three-terminal tandem modules performing outdoors are shown in Figure 4.9. The most important parameters are summarised in Table 4.7. The module located in Lisbon has the highest efficiency and the highest energy yield, which is due to lower fundamental losses and more irradiance. However, all locations have a lower efficiency compared to the efficiency at test conditions.

Table 4.7: The most important results for the 3T tandem perovskite/silicon module.

	Delft	Lisbon	Lagos	Shanghai	STC
DC efficiency [%]	23.7	23.8	23.0	23.3	24.6
AC Energy yield [MWh]	2.42	4.15	3.29	2.72	-

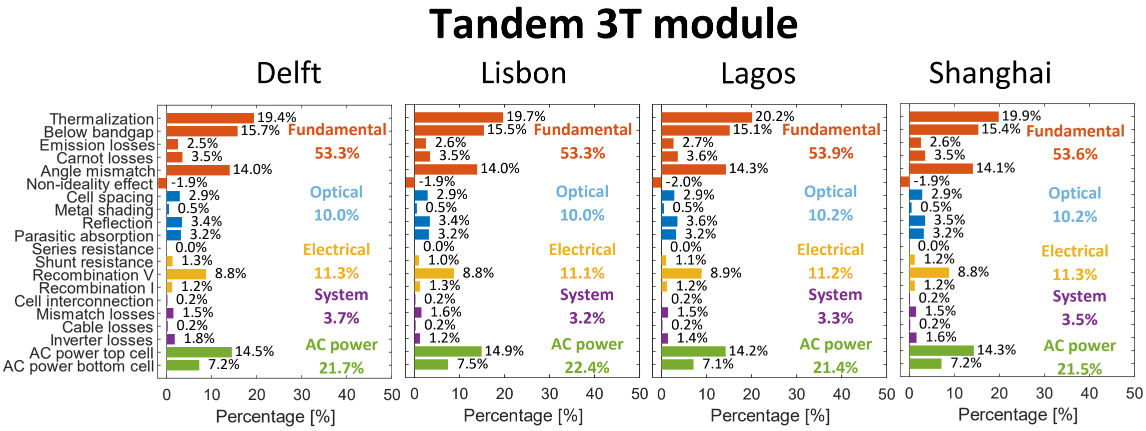

Figure 4.9: The results of the three-terminal tandem module for the different locations.

The 3T tandem module also shows an increase in thermalization losses (18.8% to 19.4%-20.2%) and a decrease of below bandgap losses (19.2% to 15.1%-15.7%), due to a blue shift in the spectrum. The increase of reflection (from 2.5% to 3.4%-3.5%) is similar to the 2T tandem module as well.

The non-ideality effect is larger for the 3T tandem module compared to the 2T tandem module. This is due to a better EQE for the 3T tandem cell, and is more deeply discussed in Section 4.7.

The recombination losses are larger compared to the 2T tandem module. Because the layer of perovskite has a greater thickness in the 3T tandem cell, there is more recombination. This leads to a higher saturation current density and a higher ideality factor, as shown in Appendix B.2. Also, these values increase for a higher cell temperature, which causes the increase of voltage recombination loss (7.9% to 8.8%-8.9%) compared to STC.

The mismatch losses in the 3T tandem module follow a different trend than in the 2T tandem module. Because the voltage ratio of the top and bottom cell stays relatively constant, the mismatch losses do not vary significantly for the conditions. At all locations and at STC the mismatch losses are 1.5%-1.6%, which is different compared to the 2T tandem module. This difference is more discussed in Section 4.7.

4.7 Comparison of the different modules

The outdoors performance of the different modules can also be compared with each other. Because the different locations all followed similar trends, the comparison will only be done for Delft. In the comparison, only significant differences will be discussed per category, similar to the discussion Chapter 3.

4.7.1 Fundamental losses

The fundamental losses for the different modules are shown in Table 4.8. Similar to the comparison at STC, the thermalization losses for the tandem modules are lower due to multiple bandgap energies.

Table 4.8: The fundamental losses for the different modules in Delft.

	Mono-facial c-Si	Bifacial c-Si	Tandem 2T perov/c-Si	Tandem 3T perov/c-Si
Thermalization [%]	32.7	32.7	19.4	19.4
Below bandgap [%]	15.7	15.7	15.7	15.7
Emission losses [%]	1.7	1.8	2.5	2.5
Carnot losses [%]	2.7	2.7	3.5	3.5
Angle mismatch [%]	13.8	14.5	14.0	14.0
Non-ideality effect [%]	-1.4	-1.3	-1.3	-1.9

Another difference between the crystalline silicon and the tandem modules, is the emission losses. Because a tandem cell has two materials that emit radiation, there is more emission for the tandem cells.

The Carnot losses are the largest for the tandem cells, because the perovskite cell has a larger bandgap energy than the silicon cell. The Carnot voltage is a fraction of the bandgap voltage, leading to an increase of Carnot losses for the tandem modules. The angle mismatch voltage increases for the bifacial module, since it has a larger solid state of emission.

The last significant difference is that the non-ideality effect is larger for the 3T tandem module than for the 2T tandem module. The non-ideality effect includes an overestimation of the emission losses, below bandgap absorption (Urbach's tail), but also the underestimation of thermalization losses. Because the perovskite cell does not have a perfect EQE, some high energy photons are absorbed by the silicon. This means that there are actually more thermalization losses than for an ideal solar cell. Because the 3T tandem cell has a better EQE (Section 3.1), this underestimation is less, leading to a better non-ideality effect.

4.7.2 Optical losses

Table 4.9 presents the optical losses for the different modules in Delft. The cell spacing and metal shading losses are larger for the tandem cells, since the tandem cells have lower fundamental losses (similar to the comparison at STC).

The cell structure plays an important role for the optical losses. Bifacial modules do not have a back reflector, leading to more transmission losses. Also, the tandem cells do not have front texturing, which leads to more reflection for the tandem modules.

The difference in parasitic absorption, is due to the different cell structures, which is also similar to the comparison at STC.

Table 4.9: The optical losses for modules in Delft.

	Mono-facial c-Si	Bifacial c-Si	Tandem 2T perov/c-Si	Tandem 3T perov/c-Si
Cell spacing [%]	2.2	2.1	2.9	2.9
Metal shading [%]	0.4	0.4	0.5	0.5
Reflection [%]	1.5	2.1	3.4	3.4
Parasitic absorption [%]	3.8	3.5	3.2	3.2

4.7.3 Electrical losses

The electrical losses are presented in Table 4.10. For the crystalline silicon modules, the resistance losses are negligible. The shunt resistance losses are higher for the 3T tandem module than for the 2T tandem module. This can be counter-intuitive, since the 3T tandem cell has a lower shunt resistance (Appendix B.2). However, since the 3T has more current coming from the perovskite cell, the shunt resistance losses increase.

The recombination losses are significantly larger for the tandem modules, which are caused by the perovskite top cells. As shown in Appendix B.2, the saturation current density and the ideality factor are larger for perovskite. This leads to more recombination, increasing the recombination voltage and current loss. Because the perovskite layer is thicker in the 3T tandem cell, the recombination for this module is higher compared to the 2T tandem module.

Table 4.10: The electric losses for modules located in Delft.

	Mono-facial c-Si	Bifacial c-Si	Tandem 2T perov/c-Si	Tandem 3T perov/c-Si
Series resistance [%]	0.0	0.0	0.0	0.0
Shunt resistance [%]	0.0	0.0	0.8	1.3
Voltage recombination [%]	4.9	4.3	6.8	8.8
Current recombination [%]	1.1	1.1	1.2	1.2

4.7.4 System losses

The system losses for the different modules are shown in Table 4.11. The 3T tandem module has the highest output current (shown in Figure 3.12 in Chapter 3), which explains the fact that it is the only module with significant cell interconnection losses.

The mismatch losses are the largest for the 3T tandem module, since it has non-active cells. As mentioned in Section 3.3, this already accounts for approximately 1.4% of the mismatch losses. However, the mismatch losses did not increase for the 3T tandem module compared to STC, whereas the mismatch losses for the 2T tandem module increased for STC.

Finally, the inverter losses are the largest for the 2T tandem module. Because this module has the lowest output current (Figure 3.12 in Chapter 3), the inverter is less efficient. This causes the inverter losses to be the highest for this module.

Table 4.11: The system losses for the different modules in Delft.

	Mono-facial c-Si	Bifacial c-Si	Tandem 2T perov/c-Si	Tandem 3T perov/c-Si
Cell interconnection [%]	0.0	0.0	0.0	0.2
Mismatch losses [%]	0.0	0.0	0.3	1.5
Cable losses [%]	0.2	0.2	0.3	0.2
Inverter losses [%]	1.9	1.7	2.6	1.8

4.8 Conclusion

This chapter analysed the loss distributions of the different module under different real-world operating conditions, such that this chapter fulfils sub-goal 3 (listed in Section 1.5). The difference between outdoors operating conditions and STC are similar for all locations. Due to a blue-shift of the spectrum, there is increase in thermalization losses, but a decrease for the below bandgap losses. Also, there is an increase in reflection losses, as light reaches the module at more oblique angles of incidence. In all cases, the modules simulated in Lagos (tropical high irradiance climate) have the lowest efficiency. Also, it was found that the difference between STC and real-world operating conditions is more significant for tandem modules than for c-Si modules.

The mismatch losses for two-terminal tandem modules increase slightly at outdoors conditions, as a result of spectral variations. However, this chapter showed that the fill factor gain partly compensates for a mismatch in absorbed current. The fill factor gain is the phenomena, where the fill factor increases when there is a current mismatch. For the 2T tandem module, a current mismatch of 7.0% only leads to a power mismatch loss of 1.2%, due to a higher fill factor. This means that the power mismatch is a better indicator for mismatch losses than the current mismatch.

5. Optimisations and improvements for tandem PV system

The last sub-goal described in Section 1.5 is to use the developed model to analyse optimisations or improvements for PV system. This chapter presents the different optimizations/ improvements that are performed and discusses the effect it has on the performance of the solar cell. These improvements are only simulated for the two-terminal perovskite/silicon module, as this module is the main focus of this study.

In this chapters, four different optimisations/ improvements are considered, which are solar tracking, fixing the cell temperature, changing the perovskite thickness, and varying the bandgap energies. The first section will discuss solar tracking, which can be seen as an improvement as it aims to improve the operating conditions. This is followed by analysing the effect of fixing the temperature which also improves the operating conditions. Then, different thicknesses of the perovskite layer are simulated and analysed. This can be seen as an optimisation, as the optimal thickness for different conditions is found. Finally, the optimal bandgap energies for maximising the upper limit are found, which can also be seen as an optimisation.

5.1 Solar tracking

An important difference between outdoors conditions and standard test conditions, is the intensity of the received in-plane irradiance. An important factor of the in-plane irradiance is the Angle of Incidence (AOI), as the direct irradiance on the module is written as [11]

$$G_M^{dir} = I_e^{dir} \cdot \cos(AOI), \tag{5.1}$$

where G_M^{dir} is the direct in-plane irradiance, I_e^{dir} is the direct normal irradiance (DNI). It can be seen that if the angle of incidence is smaller, the direct irradiance on the module will increase.

Besides increasing the in-plane irradiance, a smaller angle of incidence can also lead to other effects. Smaller angles of incidences can lead to less reflection [107]. Therefore, the efficiency of the PV system could potentially increase when reducing the angle of incidence. This is something that will be tested and analysed in this section.

To reduce the angle of incidence, solar tracking can be used. To track the sun, the module should be able to rotate either around a horizontal axis or a vertical axis. Therefore, three types of solar tracking will be distinguished, which are also shown in Figure 5.1:

1. Altitude tracking, meaning that the module can rotate around the horizontal axis.
2. Azimuth tracking, meaning that the module can rotate around the vertical axis.
3. Dual axis tracking, meaning that the module can rotate around both axes.

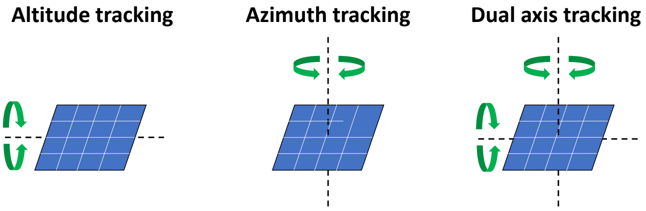

Figure 5.1: An illustration of the different types of tracking that are considered.

In literature, different implementations of solar tracking systems are described [108, 109]. However, for this study, the simulation performed is kept simple due to time restrictions. For azimuth tracking, the azimuth that maximises the incoming irradiance is selected, while the altitude of the module stays fixed. Similar for altitude tracking, the tilt of the module that maximises the in-plane irradiance is selected. This method does not always provide the angle that is closest to the sun, especially in cases with relatively high diffuse irradiance.

For dual axis tracking, the azimuth and altitude of the module are set the same as the azimuth and altitude of the sun. Because finding the azimuth and altitude that maximise the in-plane irradiation increased the simulation time significantly, this implementation is chosen.

Since the ray tracing model and irradiance model are not suitable for solar tracking, the Toolbox is not used for calculating the incoming irradiance. To calculate the in-plane irradiance, the simple irradiance model described in Section 4.1 is used. First, the spectral irradiance from each vertex is calculated for the static module, including the correction for the static module. Then, this calculated spectral irradiance from each vertex is also considered for the tracking systems. The in-plane irradiance is calculated with Equation 4.1.

5.1.1 The effect on the AC yield

As mentioned before, solar tracking increases the in-plane irradiation. Therefore, the AC energy yield can increase up to 40%. Table 5.1 shows the annual incoming irradiation, AC energy yield, and efficiency for the different tracking systems at all locations. The table shows that for all locations, the tracking systems result in an increase in in-plane irradiance, AC yield, and efficiency.

For all locations, dual axis tracking is the most effective as expected. For most locations, azimuth tracking results in a larger increase than altitude tracking. The causes of this are explained later in this section. Only for Lagos, altitude tracking is more effective. This is not surprising, as the tilt of the modules in Lagos is relatively small, which means that the module is almost flat on the ground. A change in azimuth would therefore not be as significant as for other locations.

Table 5.1: An overview of the incoming annual irradiation, efficiency, and AC energy yield for the different tracking systems in the different locations.

Location	Type of tracking	Incoming annual irradiation [MWh]	AC energy yield [MWh]	AC Efficiency [%]
Delft	None (Tilt = 31^o)	10.6	2.56	24.1
	Altitude tracking	11.4	2.77	24.4
	Azimuth tracking	12.8	3.18	24.9
	Dual axis tracking	13.7	3.46	25.2
Lisbon	None (Tilt = 28^o)	18.0	4.47	24.8
	Altitude tracking	19.3	4.85	25.1
	Azimuth tracking	22.0	5.62	25.6
	Dual axis tracking	24.5	6.31	25.8
Lagos	None (Tilt = 5^o)	14.9	3.54	23.8
	Altitude tracking	15.5	3.73	24.1
	Azimuth tracking	15.4	3.69	24.0
	Dual axis tracking	17.6	4.36	24.7
Shanghai	None (Tilt = 17^o)	12.1	2.90	24.0
	Altitude tracking	12.7	3.08	24.3
	Azimuth tracking	13.2	3.21	24.4
	Dual axis tracking	14.3	3.56	24.9

5.1.2 The effect on the efficiency

Figure 5.2 shows the efficiency of the PV system in Delft for a whole day. It can be seen that in the morning and evening the effect of azimuth and dual axis tracking is the greatest. As the sun is in the east in the morning and in the west in the evening, the *AOI* is large for the static PV system. However, by rotating around the vertical axis (which is possible for azimuth and dual axis tracking), the *AOI* can be kept small at in the morning and evening. This also explain why azimuth tracking is more effective than altitude tracking. In the middle of the day, all tracking systems are equally efficient, indicating that the optimal orientation is the same as the static system at this moment in time.

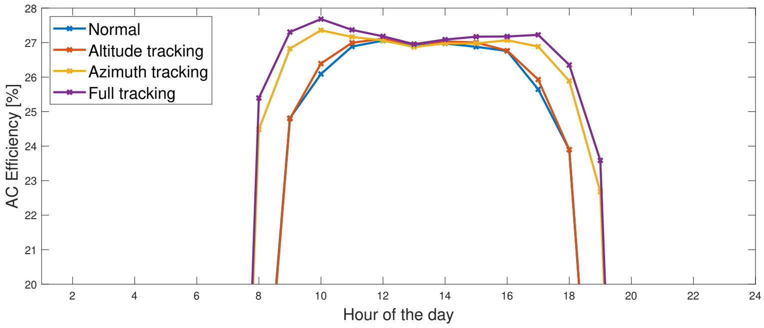

Figure 5.2: The effect of tracking for the PV system in Delft over a whole day. As example, April 9th is selected.

5.1.3 The effect on the loss distribution

To explain why the efficiency is affected by solar tracking, the loss distributions of the tracking systems need to be analysed. Figure 5.3 shows the yearly loss distribution for each tracking system.

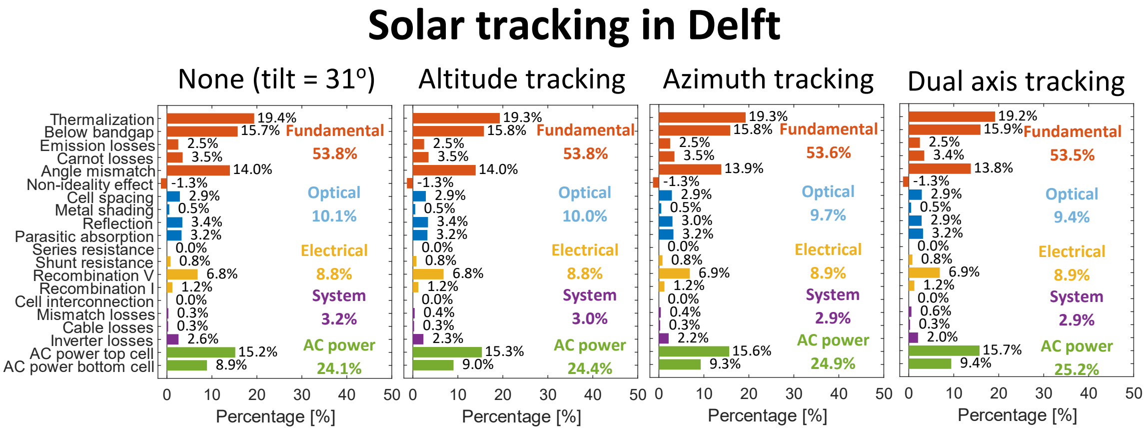

Figure 5.3: The loss distributions for the tracking systems in Delft. All values are yearly irradiance weighted.

The year average tandem system efficiency is the largest for dual axis tracking (25.2%), followed by azimuth tracking (24.9%), altitude tracking (24.4%), and static (24.1%). The increase of efficiency is mainly caused by a reduction of angle mismatch, Carnot, reflection, and inverter losses. However, the mismatch losses increase for when tracking is used.

The increase of incoming irradiance allows the optimal voltage to be larger. Since the angle mismatch and the Carnot voltage accounts for the difference between the $\frac{E_g}{q}$ and the optimal voltage, both voltages decrease for a larger optimal voltage. This leads to a reduction of the angle mismatch and Carnot losses.

As mentioned before, the angle of incidence is reduced when solar tracking is used. This leads to a reduction of the reflection losses, as the reflection decreases for a lower AOI. In the figure, it can be seen that the reflection decreases the most for dual axis tracking, as it reduces the AOI the most. For altitude tracking, however, there is no reduction in reflection observed. This is because for altitude tracking, the sky view factor needs to be taken into account. The sky view factor indicates which part of the sky (when seen as a hemisphere) can reach the module [11] and is important for diffuse irradiation. When the module is tilted, this sky view factor is reduced. To maximise the in-plane irradiance, a trade-off needs to be made between minimising the AOI for the direct irradiance and maximising the sky view factor for the diffuse irradiance. This is shown in Figure 5.4, where the incoming irradiance and reflection losses are plotted for different values of module tilt and azimuth. The simulations are done for June 13th at 13:00 as this moment provides a clear difference. It can be seen that for altitude tracking, there is a different optimal value for the reflection losses and the in-plane irradiance. For azimuth tracking however, there is only one optimal value, since the sky view factor remains constant. Therefore, the reflection is not reduced for altitude tracking.

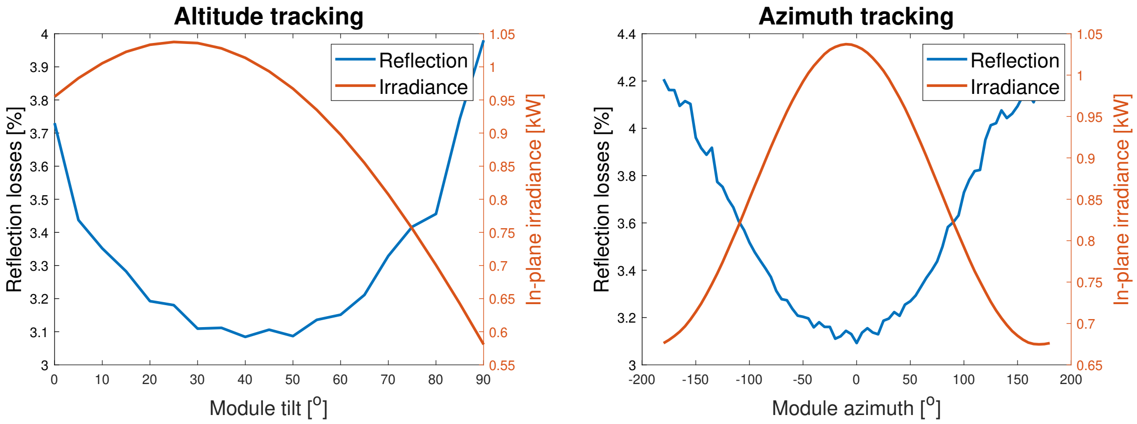

(a) The reflection losses and incoming irradiance for different values of the tilt. It can be seen that they have a different optimal tilt.

(b) The reflection losses and incoming irradiance for different azimuths. It can be seen that they have the same optimal value.

Figure 5.4: For altitude tracking, a trade-off needs to be made between maximising the incoming irradiance and minimising the reflection losses.

The inverter losses decrease as a result of a larger voltage and current. Due to a larger in-plane irradiance, the produced electricity increases. As mentioned in Chapter 4, the selected inverter becomes more efficient when the current and voltage increase, resulting in lower inverter losses.

The only loss that increases, is the mismatch loss. Due to a different in-plane irradiance, there is a greater mismatch between the top and bottom cell. This causes the mismatch losses to increase with 0.3% for dual axis tracking (from 0.3% to 0.6%). This indicates that a different thickness of perovskite may be optimal for a tracking system.

5.2 Fixing the temperature

The IV curve of a solar cell depends on the cell temperature [42–44]. Both the open circuit voltage and the fill factor decrease for a higher temperature. The temperature dependence on the IV curve on the silicon and perovskite cell in the two-terminal cell is shown in Figure 5.5. For all curves, the absorbed photocurrent is kept constant at 200 A/m^2. It can be seen that the open circuit voltage decreases for higher temperatures.

The short circuit current is also dependent on the temperature. However, this effect is not included, since this effect is also not included in the Toolbox and the effect is smaller compared to the voltage effect. Also, there is not sufficient data available for perovskite to model this effect correctly.

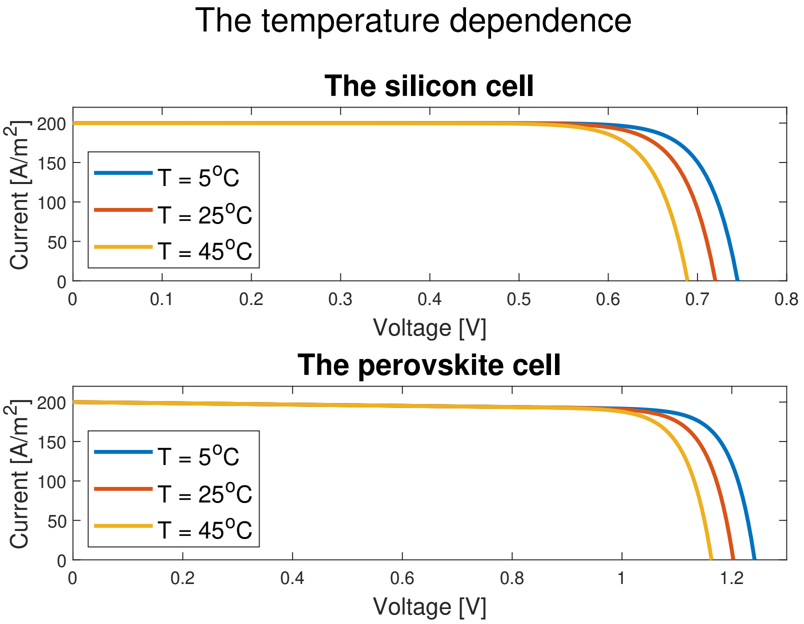

Figure 5.5: The temperature dependence on the IV curve of the silicon and perovskite cell.

As shown in Appendix C.7, the cell temperature reached values up to 60°C for different locations. To reduce the temperature of the cell, active cooling can be applied. In literature, different systems for active cooling are presented [110, 111]. For this study, however, active cooling is simulated by setting the temperature of the module equal to a fixed value. It should be noted that this might be unrealistic to keep a cell's temperature fixed at one specific temperature for a whole year. However, this is done to observe the temperature effect on the loss distribution.

5.2.1 The effect on the efficiency

The efficiencies for the PV systems under different cell temperatures are shown in Figure 5.6. It can be seen that for all locations, the efficiency decreases for a higher temperature. The highest efficiency is obtained in Lisbon due to the largest irradiation. The increase in efficiency from 50°C to 20°C is around 1.7%-1.8% for all locations.

If the efficiency at 20°C in Delft (24.5%) compare with the efficiency in Delft without cooling (24.1%), there is a relative increase of 1.7% in the efficiency. This will also lead to a 1.7% increase for the energy yield over a year. To examine whether it is beneficial to apply active cooling, the amount of energy needed for cooling needs to be calculated. This is discussed in more detail in the recommendations in Chapter 6.

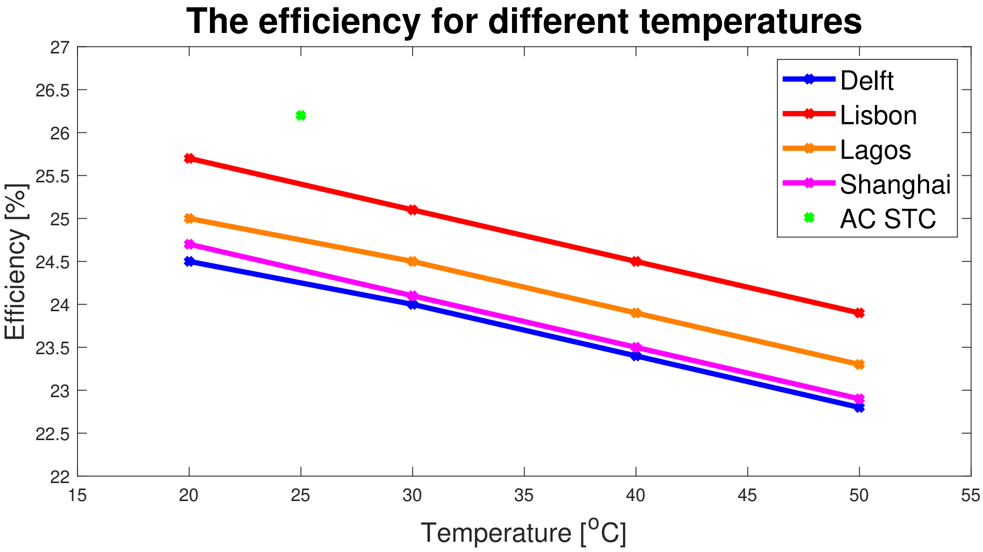

Figure 5.6: The effect of active cooling for all locations. It can be seen that at each location, the efficiency is the highest at lower temperatures. Also, the efficiency at STC (25°C) is included in the plot as a reference.

5.2.2 The effect on the loss distribution

The efficiency increase for lower cell temperature is mostly caused by a decrease in recombination, both radiative and non-radiative. As shown in Figure 5.7, the losses that change significantly are the emission, Carnot, angle mismatch, and recombination losses. In this section, only the loss distribution in Delft is presented, as all locations follow similar trends. The results of the other locations can be found in Appendix D.3.

Equation 2.10 shows that the emission will increase for a larger temperature, explaining why the emission losses increase for increasing temperatures. Due to the increase in emission, the optimal voltage decreases. This results in a lower Carnot and angle mismatch voltage, as these voltages are

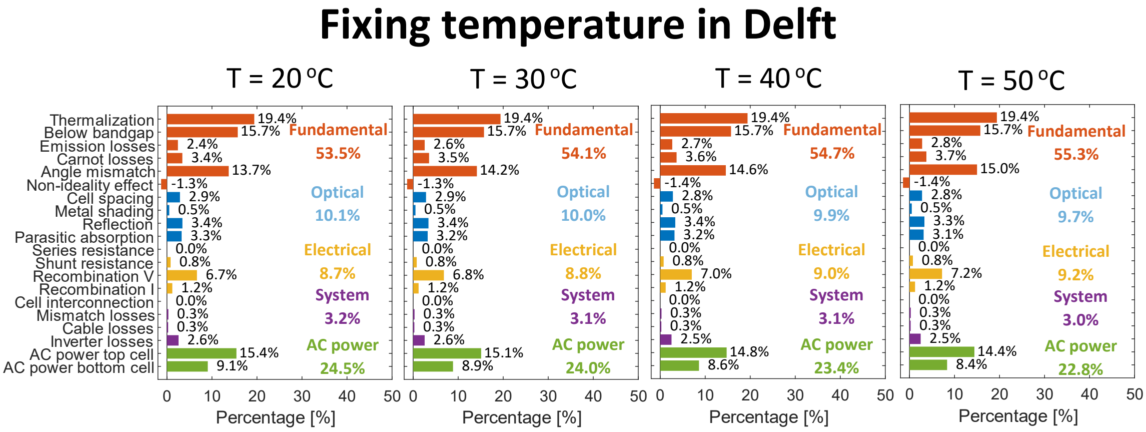

Figure 5.7: The loss distributions for active cooling in Delft. All values are yearly irradiance weighted.

the difference between the optimal voltage and $\frac{E_g}{q}$. Therefore, the Carnot and angle mismatch losses increase.

The voltage recombination losses also increase for larger temperatures. As can be seen in Appendix B.2, the saturation current density increases for larger temperatures. This results in an increase of recombination losses.

It should be noted that the optical losses and system losses decrease for a higher temperature. However, this is the result of more energy being lost in previous steps.

5.3 The thickness of the perovskite layer

The thickness of the perovskite layer affects how much photons are absorbed in the perovskite layer. For the two-terminal cell, the thickness is chosen such that current matching is achieved under STC. However, as the incoming spectral irradiance is different at outdoors conditions, the top and bottom cell become unmatched. Therefore, a different thickness of the perovskite layer may result in a better performance [112].

Another aspect that needs to be considered is that a thicker perovskite layer results in more recombination [113]. This can lead to more electric losses, resulting in a lower efficiency. This is also discussed in the design of the three-terminal cell.

To observe the effect of the perovskite thickness on the loss distributions, different thicknesses are simulated. As the original thickness is 575 nm (which provides current matching at STC), it is expected that the optimal thickness lies within the range 400 nm-700 nm. Therefore, thicknesses within this range will be simulated. All perovskite layers will be simulated in ASA to obtain the electrical characteristics. These simulations are shown in Appendix D.1.

5.3.1 The effect on the loss distribution

To qualitatively understand how the efficiency changes for different thicknesses, the loss distribution can be studied. In Figure 5.8, the loss distributions for the different thicknesses in Delft are shown. Only this location is shown, as the other locations follow a similar trend. The loss distributions for the other locations can be found in Appendix D.4. The losses that vary for different thicknesses are the non-ideality effect, the recombination, and mismatch losses. The main effect is the change in mismatch losses. The thickness of the perovskite layer determines the absorbed current in top cell and is therefore an important parameter for achieving current matching. For the lower thickness (400 nm), the top cell absorbs less current compared to the bottom cell, leading to more mismatch losses. For a greater thickness (700 nm), the top cell has absorbed more current than the bottom cell, also leading to more mismatch losses.

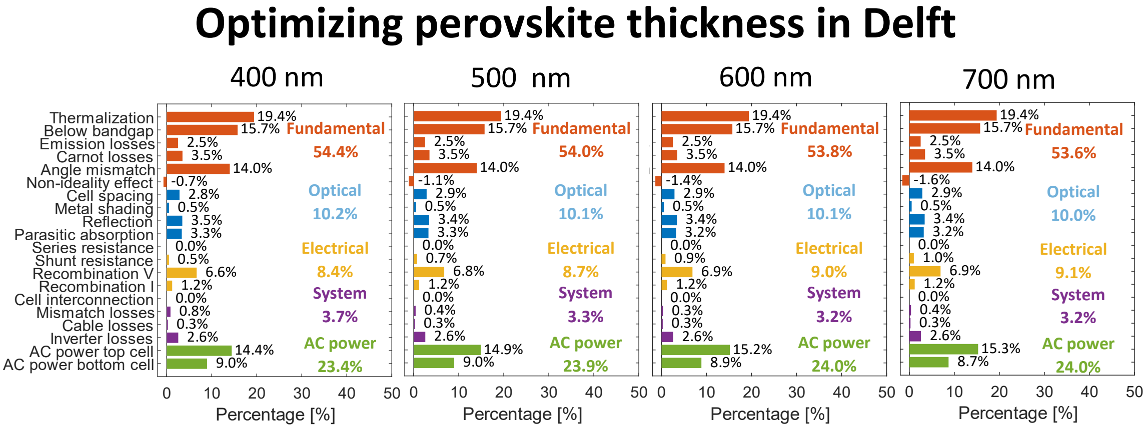

Figure 5.8: The loss distributions for active cooling in Delft. All values are yearly irradiance weighted.

An additional effect is the change of the non-ideality effect. The non-ideality effect accounts for different phenomena, such as an overestimation of emission losses, absorption below the bandgap energy (Urbach's tail), but also for an underestimation of thermalization losses for tandem cells. The latter one means that if photons with a high energy are absorbed in the bottom cell instead of the top cell, the thermalization losses for that photon increase. Note that this only happens for a non-ideal solar cell, due to a non-perfect EQE. For an ideal solar cell, all high energy photons will be absorbed in the top layer. A thicker layer of perovskite will improve the EQE, as more photons can be absorbed. This leads to thermalization losses, making the absolute value of the non-ideality effect increase.

A downside of increasing the perovskite thickness, is that the non-radiative recombination will increase. A larger thickness requires electrons and holes to travel a greater distance, resulting in a greater change of recombining. Overall, this will increase the recombination losses, which results in a voltage loss.

5.3.2 Finding the optimal efficiency

The efficiencies for different thickness at different locations are plotted in Figure Figure 5.9. To find the optimal thickness, an interval step of 25 nm is taken between 500 nm and 600 nm, as it was found that the highest efficiency is in this region. It can be seen that the highest efficiency at every location is achieved at around 575 nm. For Lisbon, Lagos, and Shanghai, the efficiency does not vary much between a 500 and 600 nm, whereas for Delft, a clear peak at 575 nm can be seen.

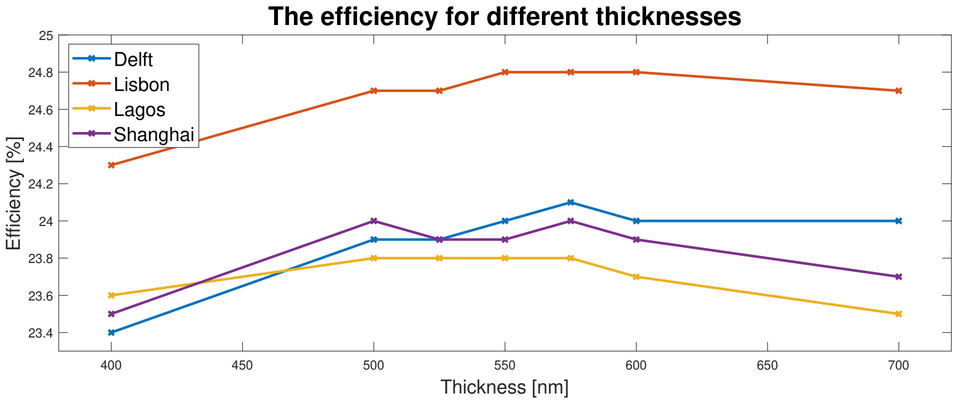

Figure 5.9: The effect of changing the thickness of the perovskite layer. The normal thickness (575 nm) is included as well. It can be seen that the optimal thickness is approximately the same for all locations.

5.4 Different bandgap energies

The fundamental losses in the developed model are determined by the bandgap energies and the incoming spectral irradiance. Based on the fundamental losses, and upper limit can be assigned for a certain location with the equation

$$\eta_{upper} = \frac{P_{in} - (P_{term} + P_{below} + P_{emission} + P_{Carnot} + P_{angle})}{P_{in}}. \tag{5.2}$$

By using the fundamental losses calculated in Chapter 4, the upper limits can be calculated for the different locations. The upper limits for the two-terminal tandem module are presented in Table 5.2. It can be seen that the upper limit varies for the different operating conditions.

Table 5.2: The upper limit for the two-terminal module at the different locations.

	Delft	Lisbon	Lagos	Shanghai	STC
η_{upper} [%]	44.9	44.8	44.1	44.5	44.1

This raises the questions if there are different values for the bandgap energy that maximise the upper limit for the different operating conditions. To find the optimal values for the bandgap energies, different combinations for the top and bottom cell are simulated. For each combination, only the fundamental losses are identified, and its upper limit is calculated. When calculating the optimal voltage, the ambient temperature is used as the cell temperature. This is done, since this temperature can be seen as the ideal temperature without considering active cooling.

The considered values for the bandgap energies range from 1.4 eV to 2.0 eV for the top cell, and 0.8 to 1.3eV for the bottom cell. It should be realised that not all bandgap energies are equally suitable or available in practice. However, this work is done purely on theoretical basis to understand which bandgap energies provide the maximal upper limit for a double junction tandem cell.

5.4.1 The optimal bandgap energies

The upper limits for the different combinations are shown in Figure 5.10. The upper limit is around 46%-47% for each location. The optimal values for the bandgap energies are shown in Table 5.3. In this table, also the optimal values for STC are also included. All locations have the same optimal bandgap energies, which is 1.73 eV for the top cell, and 0.94 eV for the bottom cell.

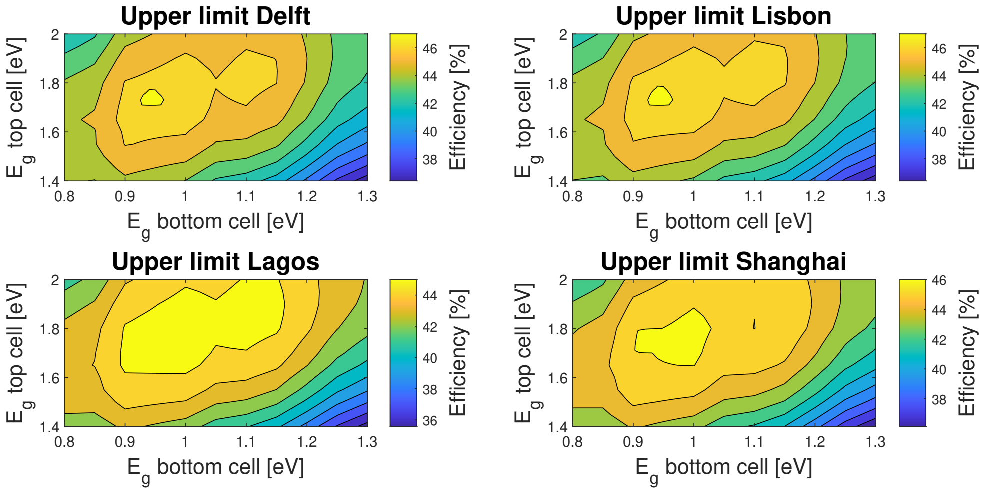

Figure 5.10: The upper limit for different combinations of bandgap energies for all locations.

Table 5.3: The optimal values for the bandgap energies at the different locations.

	Delft	Lisbon	Lagos	Shanghai	STC
Optimal E_{g1} [eV]	1.73	1.73	1.73	1.73	1.73
Optimal E_{g2} [eV]	0.94	0.94	0.94	0.94	0.94
Optimal η_{upper} [%]	47.1	47.1	46.0	46.7	45.2

Suitable materials with the corresponding bandgap energies are a perovskite based on formamidinium (FA), methylammonium (MA), cesium (Cs), and rubium (Rb) [114] (bandgap energy of 1.73 eV), and the conjugated polymer PBTTQ [115] (bandgap energy of 0.94 eV). Both of these materials have been used in a solar cell. However, these materials are only ideal for lowering the fundamental losses. More research is needed to examine the actual efficiency of such a tandem cell and the feasibility of this combination.

Delft and Lisbon have the highest upper limit (both 47.1%), followed by Shanghai (46.0%), and Lagos (46.0%). The differences between the locations are discussed in detail later in this section. An interesting result is that all locations have a higher upper limit compared to STC. Due to a lower irradiance weighted air mass (when simulated in the Toolbox) compared to STC, there is a significant spectral variation between outdoors and test conditions. This leads to more below bandgap losses at STC.

5.4.2 The fundamental losses with optimal bandgap energies

The distribution of the fundamental losses and the upper limit with the optimal bandgap energies are shown in Figure 5.11. Although all locations have the same optimal bandgap energies, there are differences in the fundamental losses.

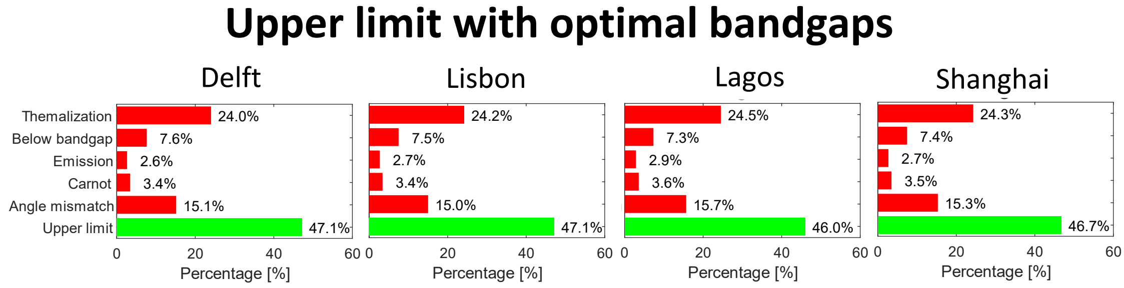

Figure 5.11: The fundamental losses and the upper limit for the optimal bandgap energies at the different locations

Each location has a different irradiance weighted air mas, which leads to spectral variations. These spectral variations cause a difference in the thermalization losses and the below bandgap losses. As Delft has the highest air mass, this location has the lowest thermalization losses and the highest below bandgap losses.

Another difference among the locations is the ambient temperature. Lagos has the highest temperature, resulting in more emission losses. This also accounts for more Carnot and angle mismatch losses, as the optimal voltage is lower. It should be realised that the cell temperature in reality would be higher than simulated. As optimal conditions are simulated, the ambient temperature is used as cell temperature. In practice, the cell temperature would be higher, resulting in more emission losses at all locations.

5.5 Conclusion

This chapter showed the results of different optimizations performed on the PV system, fulfilling the fourth and last sub-goal of this project. It was shown that solar tacking increases the mismatch losses, as the top and bottom cell absorb a different amount of photons. Nevertheless, the angle mismatch, reflection, and inverter losses can decrease for solar tracking. This eventually leads to an increase of efficiency of the PV system. Especially in the morning and evening, azimuth and dual tracking is effective.

Also, the effect of active reducing the temperature of a PV module has been quantified. Both the emission and recombination losses decrease for lower temperatures, improving the efficiency. The increase in efficiency from 50°C to 20°C is around 1.7%-1.8% for all locations. Compared to a PV system without active cooling (the temperature range can be found in Appendix C.7), there is an increase of 0.4% in efficiency. This can lead to a relative increase of 1.7% in the energy yield. These simulations can be used to examine the benefit of active cooling.

Additionally, different thicknesses of the perovskite layer are simulated. An important aspect for finding the optimal thickness is current matching. Furthermore, for lower thicknesses, the non-ideality effect becomes smaller as there are more thermalization losses. On the other hand, the non-radiative recombination increases for larger thicknesses. The results show that for real-world operating conditions, the optimal thickness is approximately the same as the optimal thickness at STC.

Finally, the optimal values of the bandgap energies that maximise the upper limit are found. The simulations show that all locations (including STC) have a maximum upper limit for a bandgap energy of 1.73 eV and 0.94 eV for the top and bottom cell respectively. The highest upper limits are found in Delft and Lisbon, which have an upper limit of 47.1%.

6. Conclusion and Recommendations

This last chapter will give the conclusion of this project and will provide recommendations for future study. First, the conclusion will be presented, and the most important results will be discussed. Then, the recommendations are presented. This includes not only improvements on the developed model or Toolbox, but also new topics that are not studied in this work due to time restrictions.

6.1 Conclusion

This work has presented a model for quantifying the loss distributions for different PV systems. This model is used to calculate the losses for four different modules in four different climates and at standard test conditions. The model is also used to understand how different improvements can increase the efficiency in a PV system.

As stated in Section 1.5, the main goal of this thesis is:

> *Use the energy loss distribution model to analyse improvements for perovskite/silicon tandem systems under realistic operating conditions.*

This goal is divided into four sub-goals, where each sub-goal builds on the results achieved in previous sub-goals and is a step closer to the main goal. For each sub-goal a chapter is dedicated to fulfil its corresponding sub-goal. It should be noted that although the main goal specifically mentions perovskite/silicon tandem systems, some sub-goals are also achieved for other types of modules. However, the final sub-goal only focuses on perovskite/silicon tandem systems.

Sub-goal 1: Development and implementation of a loss analysis model

The first sub-goal is to develop and implement a model for the loss analysis in the PVMD Toolbox. Chapter 2 discusses the implementation and the different equations used for this. In total, 17 losses are defined and divided into four categories (fundamental, optical, electrical, and system losses). Also, a non-ideality effect is included for the fundamental losses, to compensate for the non-idealities of a solar cell, when calculating the fundamental losses.

For the implemented loss analysis model, two types of validation are done. The first one was a mathematical validation, where it was shown that the percentages of all losses and the efficiency add up to 100%. This indicates that all the incoming power has been detected. The second type of validation was a physical validation, where the upper limit is compared to the upper limit derived in literature. The upper limit is defined as the efficiency of an ideal solar cell, which means that only the fundamental losses are considered. For both single junction and tandem cells, it is shown that the upper limit derived by the developed model matches the upper limit in literature (the Shockley-Quisser limit [15] and the limit calculated by De Vos [25] respectively).

Sub-goal 2: Loss analysis of a perovskite/silicon tandem module at STC

Chapter 3 presents the loss distributions for different PV modules under STC, fulfilling the second sub-goal. As a reference, the monolithic perovskite/silicon tandem cell fabricated at HZB [85] is used for the design of four different modules. The simulated modules are a mono-facial crystalline silicon, a bifacial crystalline silicon, a two-terminal perovskite/silicon tandem, and a three-terminal perovskite/silicon tandem module. Additionally, the electrical implementation for the three-terminal module considering end losses is designed, as this was not yet included in the PVMD Toolbox.

The efficiency of the tandem modules is larger than the efficiency of the crystalline silicon modules, which is mostly due to reduction of thermalization losses. However, there are also losses that increase for the tandem modules. The reflection losses increase significantly, since the cells in the tandem modules do not have front texture, whereas the single junction cells are double-textured. Also, the recombination losses increased, as perovskite has more recombination compared to silicon.

Besides comparing single junction modules with tandem modules, also the loss distribution of the two-terminal module was compared with the loss distribution of the three-terminal module. The efficiency of 2T module is larger, mostly due to lower mismatch and recombination losses.

Sub-goal 3: Loss analysis of a perovskite/silicon tandem module at real-world operating conditions

After simulating the loss distribution at STC, the modules are simulated under realistic operating conditions, thereby fulfilling sub-goal 3. This is discussed and explained in Chapter 4. Four different climates are selected for which the simulations are performed, and for each climate a location is selected. These locations are Delft, Lisbon, Lagos, and Shanghai. All four modules from Chapter 3 are simulated for all four locations.

The differences between the locations and STC show a similar trend for all locations. When simulating with SMARTS, there is a blue shift of the spectrum compared to the STC due to a lower (irradiance weighted) air mass. This causes an increase in thermalization losses, and a decrease for below bandgap losses. Also, the reflection losses increase for all modules, due to more oblique angles of incidence. In general, the difference between STC and real-world operating conditions is greater for tandem modules than for c-Si modules. Also, the tropical high irradiance climate provides the lowest efficiency for all modules.

The mismatch losses increase slightly at outdoors conditions, due to spectral variations. However, an important insight of this study is that the fill factor gain partly compensates for a current mismatch. The fill factor gain is the phenomena where the fill factor of a tandem cell increases when there is a current mismatch. This means that a current mismatch of 7.0% can be reduced to a power mismatch loss of 1.2%, due to an increase in the fill factor. Therefore, the power mismatch loss is a better indicator for mismatch losses than the current mismatch.

Sub-goal 4: Simulation of optimisations and improvements to reduce energy losses

The last sub-goal is fulfilled by Chapter 4. In this chapter, different optimisations and improvements are simulated. The simulated optimisations and improvements are solar tracking, active cooling to set the temperature, varying the thickness of perovskite, and varying the bandgap energies. For solar tracking, not only the in-plane irradiance and the energy yield, but also the efficiency of the PV system can increase. One aspect that needs to be considered for solar tracking with tandem PV modules is that the mismatch losses increase with respect to the static situation. This means that there could be a different optimal perovskite thickness for solar tracking. Nevertheless, the angle mismatch, reflection, and inverter losses decrease for solar tracking. This leads to an increase of 0.7% in the efficiency for dual axis tracking.

Additionally, the temperature of the PV module has been fixed at different temperatures. For lower temperatures, the emission and recombination losses decrease, which also lead to lower Carnot and angle mismatch losses. Overall, the increase in efficiency from 50°C to 20°C is around 1.7%-1.8% for all locations. Compared to the PV system without cooling, there is increase of 0.4%, which leads to relative increase of 1.7% in the energy yield. This can be used to examine whether active cooling is beneficial.

The yearly loss analysis is also simulated with different thicknesses for the perovskite layer. An important aspect for this is current matching, as the perovskite thickness affects the EQE of the perovskite cell. Also, it was found that lower thicknesses lead to lower non-radiative recombination losses, whereas a greater thickness leads to a better non-ideality effect. The optimal thickness for all locations is around 575 nm, which is similar to the optimal thickness for STC. Nevertheless, for most locations, there is an optimal range of thicknesses (500 - 600 nm) that provide the maximum efficiency.

Finally, the upper limit at all locations is simulated for different combinations of bandgap energies. For all locations, the optimal combination of bandgap energies are 1.73 eV and 0.94 eV for the top and bottom cell respectively. The upper limit of all locations is higher than the upper limit at STC, which is mostly due to lower below bandgap losses. The highest upper limit can be found in Delft and Lisbon, which have an upper limit of 47.1%.

6.2 Recommendations

As science is never finished, there are still improvements or extensions for this project that can be made. This section will discuss the most important recommendations for using the loss analysis model to its full potential. First, the recommendations regarding the Toolbox are discussed, which is followed by recommendations for the developed model. Then, the recommendations for the performed simulations are discussed, and finally the recommendations for the optimisations are presented.

6.2.1 Recommendations for the Toolbox

The main recommendation for the Toolbox is to consider a different model for the spectral irradiance model. The current version of the Toolbox uses the SMARTS model [101]. However, this model does not consider cloud coverage for calculating the spectral irradiance, which typically affects this. A model that does take the cloud coverage into account, is the SBDart model [116]. The SMARTS model can be replaced with the SBDart model to make the irradiance model more accurate.

Another recommendation is to improve the electrical model for tandem modules. In the current version, the top and bottom cell are simulated independently in ASA. However, especially for three-terminal tandem cells the IV curve of the top and bottom cells are not independent. Additionally, IBC cells cannot be simulated, as both GENPRO and ASA work in one dimension. To realistically simulate an IBC module, the simulation software could be extended to two (or three) dimensions.

The final recommendation for the Toolbox is to include optical effects on module level. GENPRO simulates the optical behaviour on cell level, and these results are used for the module level as well. However, on module level it is possible for light to be reflected from the non-active area to the active area. Also, photons can be reflected from the metallic wires on top of the bottom cell, which is called total reflection. The Toolbox assumes a fixed percentage of shaded area (the shading factor) and uses this for calculating the absorbed current.

6.2.2 Recommendations for the developed model

The first improvement for the developed model is to include photon recycling fundamental losses. Photon recycling is the phenomena that emitted photons can be absorbed again [117–119]. This could be included either in the emission losses or in the non-ideality effect.

Furthermore, the bandgap energies of the top and bottom cell are assumed to be constant for different temperatures. In reality, however, the bandgap energy is generally dependent on the temperature of the cell. This can be included for calculating the fundamental losses. However, this requires accurate data for the temperature dependency, which is currently not available for perovskite.

Another recommendation for the fundamental losses is to include a more accurate division between the Carnot voltage loss and the Angle mismatch loss. For this study, it is assumed that the ratio of these voltage losses is independent of the operating conditions. However, a study performed by P. Isherwood [120] shows that the Carnot limit for diffuse light is lower than for direct light, which is not included for this study. Also, the study of H. Ziar [121] shows that the entropy of lab irradiance has a lower entropy compared to outdoors irradiation, which could also be taken into account in this model.

The last recommendation for the implementation is to include quantification of the different recombination processes. For this study, the type of recombination is not specified, and it is calculated by taking the voltage loss or current loss. However, there are different types of non-radiative recombination such as Auger [122], Shockley-Read-hall, and surface recombination [11]. For the design of the solar cell, it can be useful to know the origin of the non-radiative recombination [123]. However, identifying the type of recombination would also require changes in different parts of the Toolbox, as this information needs to be provided either from the semiconductor model or the electrical model.

6.2.3 Recommendations for the simulations

The first recommendation for the simulations is to improve the design of the three-terminal tandem module. As mentioned in Section 3.1, the 2T tandem cell is used as starting point for the design of the 3T cell, and small adjustments are made. The design of the cell could be improved by considering different materials and different thicknesses. This would also make the comparison between the two-terminal and three-terminal tandem module more fair.

The developed model can also be used to simulate the loss distributions for different two-terminal tandem modules. In this project, only perovskite/silicon tandem cells are considered, as this was the focus of the project. However, this model can be used to compare various tandem cells, such as tandem cells based on CIGS materials or perovskite/perovskite tandem cells.

Another recommendation is to simulate the bifacial module under B-STC more accurately. In this work, this is simulated by multiplying the absorbed current density of the front side with 1.2. It would be more accurate to use the absorbed current density from the rear side, which is also provided by GenPro4. This current density can be multiplied with 0.2 (to make the rear irradiance 200 W/m^2) and add it to the absorbed current density of the front side. However, this requires changes in the implementation, as the calculations need to be calculated separately for both sides.

Finally, the hourly results could also be analysed. The results presented in this chapter are based on annual irradiance weighted results. However, it could also be interesting to analyse the seasonal variations over a year or the hourly variations over a day.

6.2.4 Recommendations for the optimisations/ improvements

The first recommendation is an improvement for the implementation of solar tracking. For dual axis tracking, the altitude and azimuth of the sun are used as the altitude and azimuth of the module. However, it is possible that this does not maximise the incoming irradiance for a large diffuse irradiance. The implementation could be improved by selecting the altitude and azimuth by maximizing the in-plane irradiance, similar to the implementation of single-axis tracking. This was not done, as it would increase the simulation time significantly. However, by improving the code for the implementation, the simulation time could be reduced. This could potentially lead to more accurate results.

Another improvement for the implementation of solar tracking is to use the irradiance model of the Toolbox. However, this requires that the ray tracing module also needs to simulate different orientations of the module, which will also increase the simulation time.

The last recommendation for solar tracking is to simulate altitude tracking for a different fixed azimuth. In the current simulation, the module is facing south (as this is optimal for the static situation). However, it might be more efficient to have the module facing west/east, such that the module can follow the sun in the morning and evening.

For fixing the temperature, more time and effort can be spent on estimating whether it is beneficial to actively cool the PV module. It is shown that the efficiency improves when the temperature is fixed at 20°C compared to the PV system without cooling. This also leads to a larger energy yield. However, the energy needed for cooling the PV modules also needs to be taken into account. By calculating how much energy is needed for cooling, an accurate estimation can be made whether active cooling is beneficial.

Also, more research can be spent on changing the bandgap energies of the top and bottom cell. In this study, only the fundamental losses are calculated for different bandgap energies. The next challenge is to study whether it is feasible to design a tandem cell with these bandgap energies and analyse the non-fundamental losses (i.e., reflection, non-radiative recombination losses). Another approach would be to keep one bandgap energy fixed and optimise the other bandgap energy. Silicon is very popular as bottom cell, as it is very abundant in nature. Therefore, the optimal bandgap energy for the top cell can be found, when considering silicon as bottom cell.

The final recommendation for the optimisations/improvements is to perform optimisations for more parameters. Especially on cell level, there more optimisations are possible. Other thicknesses (besides perovskite) can be varied to observe its effect on the loss distribution. This could be done for the anti reflection coating, but also for hole/electron transport materials. It could be possible that there is a different optimal value for outdoors conditions.

A. Appendix implementation

A.1 Derivation of the optimal voltage

According to [63], the current density in a solar cell under black body radiation can be written as:

$$J = q\int_{E_g}^{\infty} \phi_E\left(E, T_{sun}, 0, \Omega_{abs}\right) dE - q\int_{E_g}^{\infty} \phi_E\left(E, T_{cell}, q\cdot V_{opt}, \Omega_{emit}\right) dE$$

In this equation, ϕ_E is the photon emission flux per unit energy and per unit solid angle, given as

$$\phi_E\left(E, T, \mu, \Omega\right) = \frac{2\cdot\Omega}{c^2\cdot h^3}\cdot\frac{E^2}{e^{\frac{E-\mu}{kT}}-1}$$

. In this equation:

- Ω is the solid angle.
- c is the speed of light.
- h is Planck's constant.
- E is the energy of the emitted photons.
- μ is the chemical potential.
- k is Boltzmann constant's.
- T is the temperature of the emitter.

Substituting this in, results into the following equation:

$$J = q\int_{E_g}^{\infty} \frac{2\cdot\Omega_{abs}}{c^2\cdot h^3}\cdot\frac{E^2}{e^{\frac{E}{kT_{sun}}}-1}dE - q\int_{E_g}^{\infty} \frac{2\cdot\Omega_{emit}}{c^2\cdot h^3}\cdot\frac{E^2}{e^{\frac{E-q\cdot V_{opt}}{kT_{cell}}}-1}dE$$

$$J = \frac{2\cdot q}{c^2\cdot h^3}\left(\Omega_{abs}\int_{E_g}^{\infty}\frac{E^2}{e^{\frac{E}{kT_{sun}}}-1}dE - \Omega_{emit}\int_{E_g}^{\infty}\frac{E^2}{e^{\frac{E-q\cdot V_{opt}}{kT_{cell}}}-1}dE\right)$$

The term $\frac{E^2}{e^{\frac{E-\mu}{kT}}-1}$ can be approximated to $E^2\cdot e^{-\frac{E-\mu}{kT}}$ if $\frac{E\mu}{k\cdot T} > 2$, which is true if $E > 1.12$ eV (the bandgap of silicon). Using this approximation, results in:

$$J \approx \frac{2\cdot q}{c^2\cdot h^3}\left(\Omega_{abs}\int_{E_g}^{\infty} E^2\cdot e^{-\frac{E}{kT_{sun}}}dE - \Omega_{emit}\int_{E_g}^{\infty} E^2\cdot e^{-\frac{E-q\cdot V_{opt}}{kT_{cell}}}dE\right)$$

$$J \approx \frac{2\cdot q}{c^2\cdot h^3}\left(\Omega_{abs}\int_{E_g}^{\infty} E^2\cdot e^{-\frac{E}{kT_{sun}}}dE - \Omega_{emit}\cdot e^{\frac{q\cdot V_{opt}}{k\cdot T}}\int_{E_g}^{\infty} E^2\cdot e^{-\frac{E}{kT_{cell}}}dE\right)$$

By using partial integration twice, the integral $\int_{E_g}^{\infty} E^2\cdot e^{-\frac{E}{kT}}dE$ can be calculated. This gives:

$$\int_{E_g}^{\infty} E^2\cdot e^{-\frac{E}{kT}}dE = e^{-\frac{E_g}{kT}}\cdot\left(E_g^2\cdot kT + 2E_g\cdot\left(kT\right)^2 + 2\cdot\left(kT\right)^3\right)$$

Substituting this into the equation for J, gives:

$$
\begin{aligned}
J \approx \frac{2\cdot q}{c^2\cdot h^3}\Omega_{abs} e^{-\frac{E_g}{kT_{sun}}} \cdot \left(E_g^2 \cdot kT_{sun} + 2E_g\left(kT_{sun}\right)^2 + 2\left(kT_{sun}\right)^3\right) \\
- \frac{2\cdot q}{c^2\cdot h^3}\Omega_{emit}\cdot e^{-\frac{E_g - q\cdot V_{opt}}{k\cdot T}} \cdot \left(E_g^2 \cdot kT_{cell} + 2E_g\left(kT_{cell}\right)^2 + 2\left(kT_{cell}\right)^3\right)
\end{aligned}
$$

The power of the solar cell is given as $P = J \cdot V_{opt}$. This means that the power can be written as:

$$
\begin{aligned}
P = V_{opt}\frac{2\cdot q}{c^2\cdot h^3}\Omega_{abs} e^{-\frac{E_g}{kT_{sun}}} \cdot \left(E_g^2 \cdot kT_{sun} + 2E_g\left(kT_{sun}\right)^2 + 2\left(kT_{sun}\right)^3\right) \\
- V_{opt}\frac{2\cdot q}{c^2\cdot h^3}\Omega_{emit}\cdot e^{-\frac{E_g - q\cdot V_{opt}}{k\cdot T}} \cdot \left(E_g^2 \cdot kT_{cell} + 2E_g\left(kT_{cell}\right)^2 + 2\left(kT_{cell}\right)^3\right)
\end{aligned}
$$

The power depends on the bandgap energy and on the voltage. To maximise the power with respect to the bandgap, $\frac{\partial P}{\partial E_g}$ should be equal to zero.

$$
\frac{\partial P}{\partial E_g} = \frac{2\cdot q}{c^2\cdot h^3}\left(-\Omega_{abs}\cdot V_{opt}\cdot e^{-\frac{E_g}{kT_{sun}}} E_g^2 + \Omega_{emit}\cdot V_{opt}\cdot e^{-\frac{E_g - q\cdot V_{opt}}{kT_{cell}}} E_g^2\right) = 0
$$

$$
\begin{aligned}
\Omega_{abs}\cdot e^{-\frac{E_g}{kT_{sun}}} &= \Omega_{emit}\cdot e^{-\frac{E_g - q\cdot V_{opt}}{kT_{cell}}} \\
q\cdot V_{opt} &= E_g\left(1 - \frac{T_{cell}}{T_{sun}}\right) - k\cdot T_{cell}\ln\left(\frac{\Omega_{emit}}{\Omega_{abs}}\right) \\
V_{opt} &= \frac{E_g}{q} - \frac{E_g}{q}\frac{T_{cell}}{T_{sun}} - \frac{k\cdot T_{cell}}{q}\ln\left(\frac{\Omega_{emit}}{\Omega_{abs}}\right)
\end{aligned}
$$

A.2 Implementation for tandem junction modules

For the implementation of a tandem solar cell, the calculation of the fundamental and the optical losses has to be changed. The electrical and system losses, however, can stay the same. This section will discuss the main differences between the implementation for single junction solar cells and double junction solar cells.

In the rest of this section, three different wavelength ranges are used. They are defined in the following way:

- Wavelength range 1: from 0 to $\lambda_{g,1}$.
- Wavelength range 2: from $\lambda_{g,1}$ to $\lambda_{g,2}$.
- Wavelength range 3: from $\lambda_{g,2}$ to ∞.

A.2.1 The Fundamental losses

In a tandem solar cell there is a top cell and a bottom cell. The top cell has a bandgap energy of $E_{g,1}$ (corresponding to a wavelength of $\lambda_{g,1}$) and and ideal operating voltage of

$$
V_{opt,1} = \frac{E_g, 1}{q} - \frac{E_g, 1}{q}\frac{T_{cell}}{T_{sun}} - \frac{k\cdot T_{cell}}{q}\ln\left(\frac{\Omega_{emit}}{\Omega_{abs}}\right).
$$

The bottom cell has a bandgap energy of $E_{g,2}$ (corresponding to a wavelength of $\lambda_{g,2}$) and and ideal operating voltage of

$$V_{opt,2} = \frac{E_g,2}{q} - \frac{E_g,2}{q}\frac{T_{cell}}{T_{sun}} - \frac{k \cdot T_{cell}}{q}\ln\left(\frac{\Omega_{emit}}{\Omega_{abs}}\right).$$

Both $V_{opt,1}$ and $V_{op,2}$ can be derived in a similar way as shown in Appendix A.1. For each of the five fundamental losses, the equations are shown and a small explanation is given.

Thermalization losses

The thermalization losses are split over the two cells. For the top cell, there are thermalization losses in the first wavelength range and for the bottom cell there are thermalization losses in the second wavelength range. This can be written as

$$P_{term} = A_{mod}\left(\int_0^{\lambda_{g,1}} \phi_{AM1.5}(\lambda)\left(\frac{h \cdot c}{\lambda} - E_{g,1}\right)d\lambda + \int_{\lambda_{g,1}}^{\lambda_{g,2}} \phi_{AM1.5}(\lambda)\left(\frac{h \cdot c}{\lambda} - E_{g,2}\right)d\lambda\right). \quad \text{(A.1)}$$

Below bandgap losses

The below bandgap losses only occur in wavelength range 3. Therefore, the below bandgap losses can be written as

$$P_{below} = A_{mod}\int_{\lambda_{g,2}}^{\infty} I_{AM1.5}(\lambda)d\lambda. \quad \text{(A.2)}$$

Emission losses

Both solar cells will emit photons due to black body radiation. However, the solar cells will only emit photons in the wavelength region in which they absorb photons. For the ideal situation, this means the top cell will emit photons in the first wavelength range and the bottom cell will only emit photons in the second wavelength range. The total emission losses can be calculated with

$$\begin{aligned} P_{emission} = A_{mod}&\int_0^{\lambda_{g,1}} E_{g,1} \cdot \phi_\lambda\left(\lambda, T_{cell}, q \cdot V_{opt,1}, \Omega_{emit}\right)d\lambda \\ +A_{mod}&\int_{\lambda_{g,1}}^{\lambda_{g,2}} E_{g,2} \cdot \phi_\lambda\left(\lambda, T_{cell}, q \cdot V_{opt,2}, \Omega_{emit}\right)d\lambda. \end{aligned} \quad \text{(A.3)}$$

Carnot losses

The Carnot losses can be calculated by multiplying the Carnot voltage of each solar cell with its maximum current. The maximum current for the top cell are all the photons in the first wavelength range excluding the emitted photons. The maximum current for the bottom cell is similar except calculated in the second wavelength range excluding the emitted photons. These maximum currents can be written as

$$\begin{aligned} I_{max,1} &= A_{mod} \cdot q \int_{0}^{\lambda_{g,1}} \phi_{AM1.5}(\lambda) - \phi_{\lambda,emission,1}(\lambda) d\lambda, \\ I_{max,2} &= A_{mod} \cdot q \int_{\lambda_{g,1}}^{\lambda_{g,2}} \phi_{AM1.5}(\lambda) - \phi_{\lambda,emission,2}(\lambda) d\lambda. \end{aligned} \tag{A.4}$$

The total Carnot losses can then be calculated with

$$P_{Carnot} = \frac{E_{g,1}}{q} \frac{T_{cell}}{T_{sun}} \cdot I_{max,1} + \frac{E_{g,2}}{q} \frac{T_{cell}}{T_{sun}} \cdot I_{max,2}. \tag{A.5}$$

Note that these equations only hold for black body radiation, as this gives an analytic expression for the Carnot voltage. For other incoming irradiance, the Carnot voltage needs to be scaled in a similar way as is done for the normal implementation.

Angle mismatch losses

The angle mismatch losses can be calculated in a similar way as the Carnot losses. Since the voltage loss is the same for both solar cells, this voltage loss can be multiplied with the sum of $I_{max,1}$ and $I_{max,2}$, written as

$$P_{angle} = \frac{k \cdot T_{cell}}{q} \ln\left(\frac{\Omega_{emit}}{\Omega_{abs}}\right) \cdot (I_{max,1} + I_{max,2}) \tag{A.6}$$

Note that these equations only hold for black body radiation, as this gives an analytic expression for the angle mismatch voltage. For other incoming irradiance, the angle mismatch voltage needs to be scaled in a similar way as is done for the normal implementation.

The non-ideality effect

The non-ideality effect, which accounts for the overestimation of the fundamental losses, is calculated with a similar equation as the single junction. The only difference is that an additional component is added that accounts for an underestimation of thermalization losses. When a high energy photon is absorbed in the bottom cell instead of the top cell, there are more thermalization losses. This is accounted for with the third non-ideal component.

$$P_{non-ideal} = P_{non-ideal,1} + P_{non-ideal,2} + P_{non-ideal,3} \tag{A.7}$$

The third non-ideal component is calculated with Equation (A.8). It consists of two components, since for some photons the thermalization is underestimated (high energy photons absorbed in the bottom cel), and for some photons the thermalization is overestimated (low energy photons absorbed in the top cell).

$$\begin{aligned} P_{non-ideal,3} = (E_{term,2} - E_{term,1}) \cdot \int_{0}^{\lambda_{g,1}} \phi_{in}(\lambda) \cdot EQE_2(\lambda) d\lambda \\ + (E_{term,1} - E_{term,2}) \cdot \int_{\lambda_{g,1}}^{\lambda_{g,2}} \phi_{in}(\lambda) \cdot EQE_1(\lambda) d\lambda, \end{aligned} \tag{A.8}$$

where $E_{term,i}$ is the energy lost by thermalization per photon for cell i.

A.2.2 Optical losses

The losses due to cell spacing and metallization can still be calculated with Equations (2.23) and (2.24) respectively. The reflection and parasitic absorption losses can be calculated in a similar method.

The reflection and transmission losses

For each wavelength, the reflectivity and transmissivity is given as shown in Figure 2.2b. Therefore, the photon flux can be integrated over the different wavelengths. It should be noted that the photons in the first wavelength range lose an energy of $q \cdot V_{opt,1}$ and the photons in the second wavelength lose an energy of $q \cdot V_{opt,2}$. The total reflection losses are

$$\begin{aligned} P_{ref,trans} = A_{eff} \int_{0}^{\lambda_{g,1}} & (\phi_{AM1.5}(\lambda) - \phi_{\lambda,emission,1}(\lambda)) \cdot (R(\lambda) + T(\lambda)) \cdot q \cdot V_{opt,1} d\lambda \\ + A_{eff} \int_{\lambda_{g,1}}^{\lambda_{g,2}} & (\phi_{AM1.5}(\lambda) - \phi_{\lambda,emission,2}(\lambda)) \cdot (R(\lambda) + T(\lambda)) \cdot q \cdot V_{opt,2} d\lambda. \end{aligned} \tag{A.9}$$

Parasitic absorption

The losses due to parasitic absorption can be calculated in a similar method, written as

$$\begin{aligned} P_{par-abs} = A_{eff} \int_{0}^{\lambda_{g,1}} & (\phi_{AM1.5}(\lambda) - \phi_{\lambda,emission,1}(\lambda)) \cdot \alpha_{par}(\lambda) \cdot q \cdot V_{opt,1} d\lambda \\ + A_{eff} \int_{\lambda_{g,1}}^{\lambda_{g,2}} & (\phi_{AM1.5}(\lambda) - \phi_{\lambda,emission,2}(\lambda)) \cdot \alpha_{par}(\lambda) \cdot q \cdot V_{opt,2} d\lambda. \end{aligned} \tag{A.10}$$

A.3 Results for different methods recombination losses

As described in Section 2.5, there are three different methods to calculate the non-radiative recombination losses. The loss percentages of the electrical losses of the different methods are listed in Table A.1. Also, the sum of all percentages is presented in this table. It can be seen that for method 2 and 3, the final percentages do not add up to 100% exactly. For this reason, method 1 is selected.

Table A.1: The power distribution of the various categories for the different methods. The results are presented as percentage single junction/ percentage tandem junction

Category	Method 1 [%]	Method 2 [%]	Method 3
Series resistance	0.0 / 0.0	0.0 / 0.0	0.0 / 0.0
Shunt resistance	0.0 / 0.8	0.0 / 0.8	0.0 / 0.8
Recombination voltage	5.0 / 6.5	5.0 / 6.5	4.8 / 7.3
Recombination current	1.0 / 1.2	1.0 / 1.2	1.0 / 1.2
Power	19.9 / 26.1	19.9 / 26.1	19.9 / 26.1
Total	100.00 / 100.00	100.00 / 99.98	99.85 / 100.71

A.4 Difference AM1.5 and black body radiation

The AM1.5 spectrum is defined as the typical irradiance on earth on the cloudless day, as discussed in Section 1.1. This spectrum is similar to the black body irradiation received from the earth, as shown in Figure A.1. The difference in the spectra is due to absorption of the atmosphere.

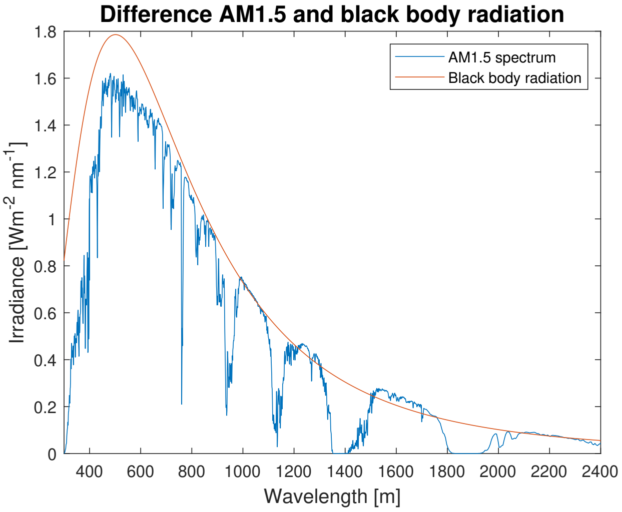

Figure A.1: The difference irradiance spectrum between AM1.5 and black body radiation.

The implementation described in Chapter 2 can also be done under black body radiation. These results are shown in Figure A.2. The upper limit for a single junction solar cell is 30.0% and the upper limit for a tandem junction solar cell is 40.6%.

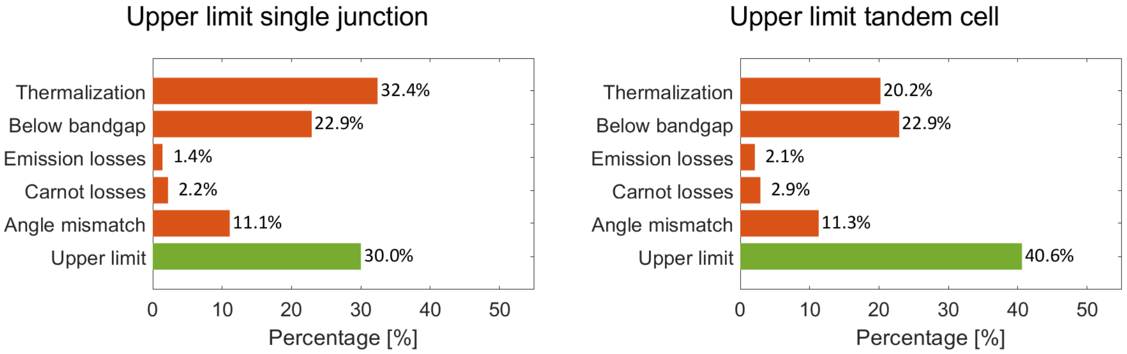

(a) The upper limit for a single junction module. (b) The upper limit for a tandem module.

Figure A.2: The upper limit of a single solar cell and tandem solar cell under black body radiation. For the upper limit, only the fundamental losses are considered.

A.4.1 Upper limit for ideal bandgap energies

As shown in [25], the ideal bandgap energies for a tandem solar cells are 1.0 eV for the bottom cell and 1.9 eV for the top cell. The fundamental losses can be calculated for these bandgap energies as well, as shown in Figure A.3. The other losses can not be calculated, since they depend on the parameters of the solar cell. It can be seen that the fundamental limit for the ideal bandgap energies is 42.0%.

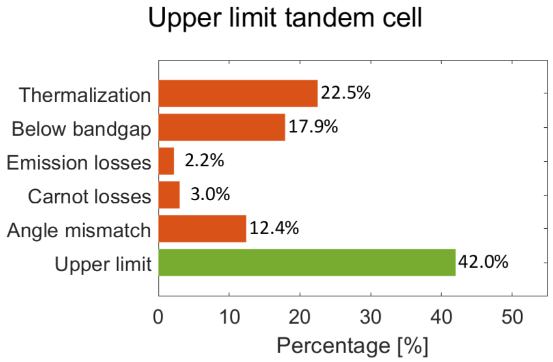

Figure A.3: The fundamental losses with a bandgap energy of 1.0 eV and 1.9 eV for the bottom and top cell respectively. Black body radiation is considered.

B. Appendix losses STC

B.1 The comprehensive model for the reverse connection

The voltages of the middle contacts are calculated by solving a set of equations. Since there are N middle contacts, also N equations need to be defined.

To indicate the voltage of an arbitrary middle point, $V_{middle,x}$ will be used, where x is a number between 1 and N. To indicate the voltage over a single top cell or bottom cell, $V_{top,x}$ and $V_{bottom,x}$ will be used respectively. By looking at Figure 3.10 it can be seen that the voltage of the top cells can be written as for $x \geq m$ holds that

$$\begin{aligned} V_{top,x} &= V_{middle,x} - V_{middle,x-m} && \text{if } x > m \\ V_{top,x} &= V_{middle,x} && \text{if } x \leq m \end{aligned} \tag{B.1}$$

For the voltage over the bottom cells a similar relation can be defined. Since the last n bottom cells are not connected, there voltage will be undefined.

$$\begin{aligned} V_{bottom,x} &= V_{middle,x} - V_{middle,x-n} && \text{if } n < x \leq N - n \\ V_{bottom,x} &= V_{middle,x} && \text{if } x \leq n \end{aligned} \tag{B.2}$$

The current through each cell can be calculated with Equation (1.2), which is discussed in Chapter 1. This equation is obtained by solving the voltage current relationship in the five-parameter model. The current of a top cell and bottom cell, will be indicated with $I_{top,x}\left(V_{top,x}\right)$ and $I_{bottom,x}\left(V_{bottom,x}\right)$ respectively.

At each middle point, current is coming in and current is going out. According to Kirchhoff's current law, the incoming current should equal the outgoing current. This law can be used to create several equations for the system of equations. For $1 \leq x \leq N - m$ the following holds.

$$I_{top,x}\left(V_{top,x}\right) + I_{bottom,x}\left(V_{bottom,x}\right) = I_{top,x+m}\left(V_{top,x+m}\right) + I_{bottom,x+n}\left(V_{bottom,x+n}\right) \tag{B.3}$$

The last m equations that are needed to complete the set of N equations will come from the last m middle points. Since the last m middle points are all connected to the output, it can be defined that for $x > N - m$

$$V_{middle,x} = V_{out} \tag{B.4}$$

V_{out} can then be varied to obtain the IV-curve.

B.2 Dependence parameters on photo generated current and temperature

The values of the parameters in the five parameter model are dependent on both the photo current density and the temperature. The dependencies on these quantities is shown in this section.

B.2.1 Dependence on photo generated current

When calculating the dependence on the photo generated current, the temperature is assumed to be constant at 298.15 K. For each figure, silicon is shown on the left and perovskite is shown on the right.

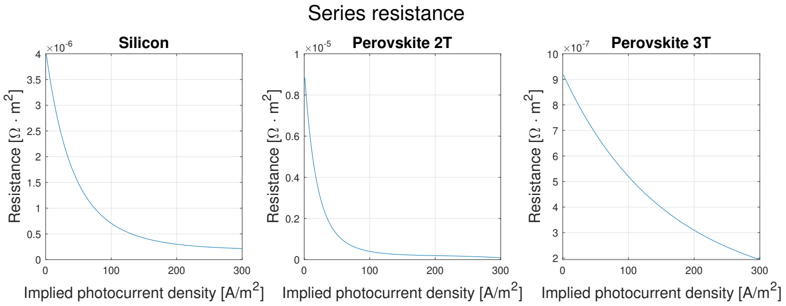

Figure B.1: The effect of the photo generated current on the series resistance.

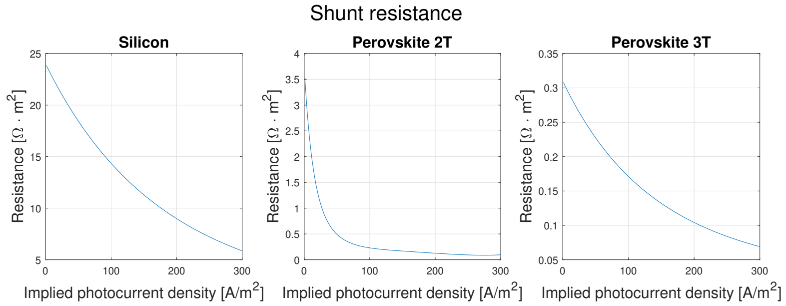

Figure B.2: The effect of the photo generated current on the shunt resistance.

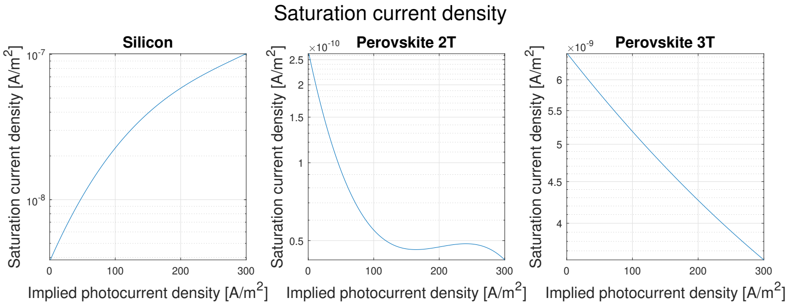

Figure B.3: The effect of the photo generated current on the saturation current density.

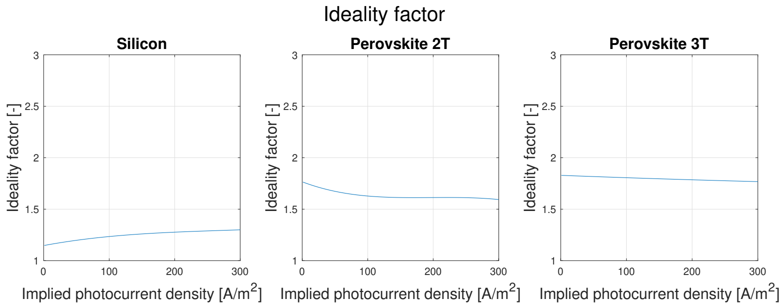

Figure B.4: The effect of the photo generated current on the ideality.

B.2.2 Dependence on the cell temperature

When calculating the dependence on the temperature of the cell, the photo-generated current is assumed to be constant at 150 A/m^2. For each figure, silicon is shown on the left and perovskite is shown on the right.

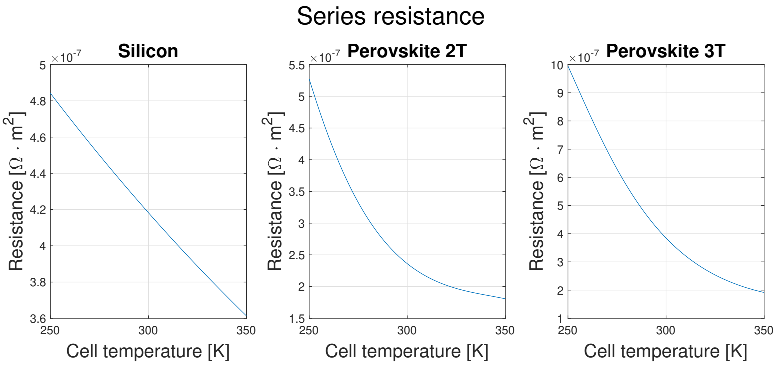

Figure B.5: The effect of the cell temperature on the series resistance.

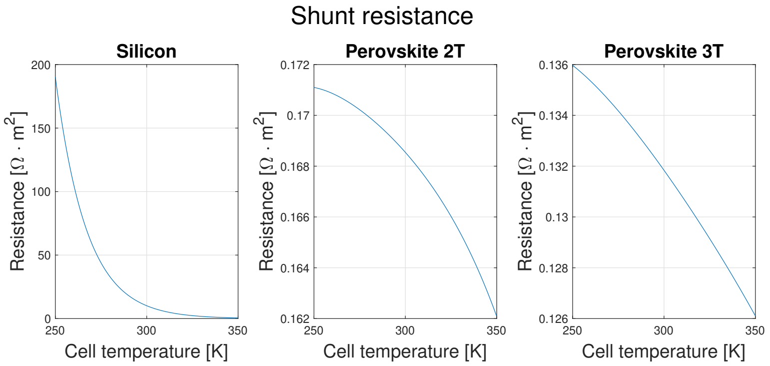

Figure B.6: The effect of the cell temperature on the shunt resistance.

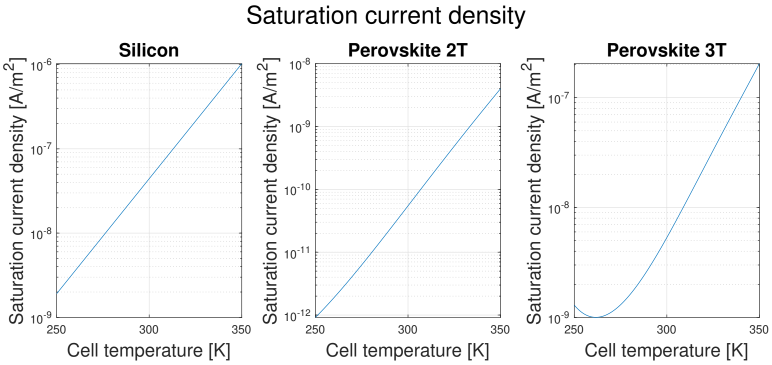

Figure B.7: The effect of the cell temperature on the saturation current density.

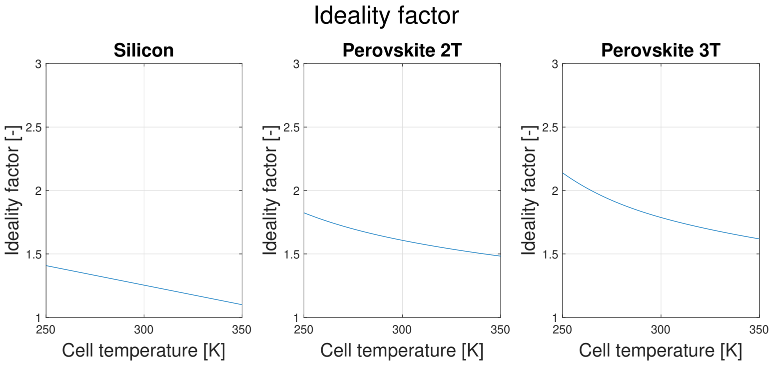

Figure B.8: The effect of the cell temperature on the ideality.

B.3 Optical difference 3T cell

The rear contact of the three-terminal tandem cell is an IBC-contact. In the Toolbox, however, the input is one-dimensional, which makes it impossible to simulate an IBC contact. For the 3T tandem cell, it is therefore assumed that the optical behaviour of both rear contacts is the same. This assumption is tested by simulating the EQE of the cell with the different rear contacts. In Figure B.9, the EQE of the cell with the p-layer at the rear and the EQE of the cell with the n-layer at the rear are simulated. As can be seen, there is no significant difference.

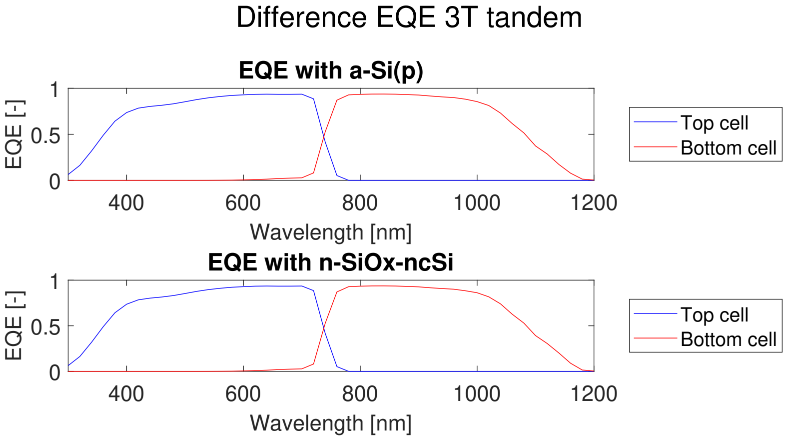
Difference EQE 3T tandem

EQE with a-Si(p)

EQE with n-SiOx-ncSi

Figure B.9: The difference in EQE between the two rear materials.

B.4 Results reverse connection

The results of the series and reverse connected 3T tandem modules are shown in Figure B.10. It can be seen that the series connected module is sightly more efficient, but the loss distribution shows some significant differences. For the reverse connection, there are more reflection losses, whereas there are more mismatch losses for the series connection.

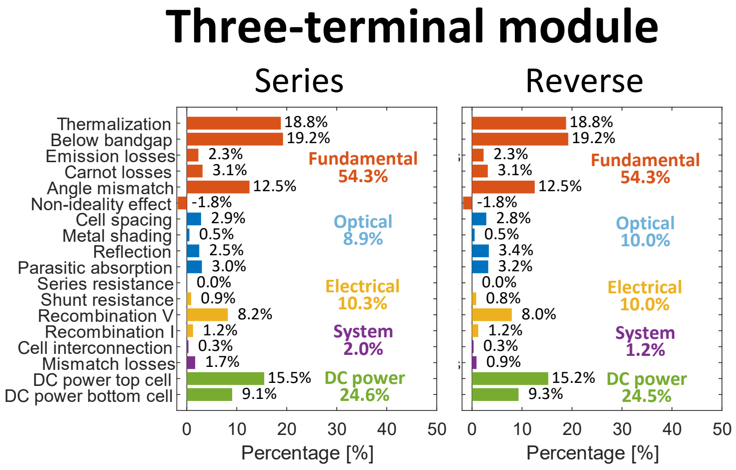
Three-terminal module

Series

Reverse

Figure B.10: The results for the series and reverse connected 3T tandem modules. The series connected module is slightly more efficient.

C. Appendix outdoor losses

C.1 Assuming equal irradiance for every cell

The sensitivity map that is used for calculating the photo generated current uses the software LUX. This software uses a Monte-Carlo ray-tracing method. Because a finite number of rays are used, there will be some randomness involved in this calculation. Due to this randomness, there can be a mismatch of irradiance between the cells. Although it is possible that some cells receive more irradiance than other cells, there is also a difference for the same cell after repeating the simulation. This is shown in Table C.1.

	Cell 1	Cell 2	Cell 3	Cell 4	Cell 5
Simulation 1	244.6 A/m^2	246.4 A/m^2	241.1 A/m^2	244.7 A/m^2	237.2 A/m^2
Simulation 2	244.9 A/m^2	241.5 A/m^2	246.0 A/m^2	243.8 A/m^2	241.1 A/m^2
Simulation 3	240.8 A/m^2	240.5 A/m^2	246.3 A/m^2	244.0 A/m^2	240.9 A/m^2

Table C.1: The received irradiance by the first 5 cells for three identical simulations. The location is Delft and the date is January 20 at 13:00.

It can be seen that the difference between cells has the same order as the difference between simulations. Therefore, it can be argued that the difference between cells is caused partly by randomness. It should also be noted that these simulations used the maximum amount of rays, which is time-consuming. When using the a lower value, this difference can become higher. To reduce the randomness as much as possible, the average is taken over all the cells, resulting in an equal irradiance for every cell.

C.2 The irradiance model for bifacial modules

For bifacial modules, the irradiance can come from both the front and the rear, which makes the irradiance model more complicated. To extend the model described in Section 4.1 for bifacial modules, the irradiance has been split into three components, which can be written as:

$$I_{total} = I_{front,direct} + I_{rear,direct} + I_{rear,albedo} \tag{C.1}$$

In this equation, I_{total} is the total incoming irradiance, $I_{front,direct}$ is the irradiance at the front coming directly from the vertices, $I_{rear,direct}$ is the irradiance at the rear coming directly from the vertices, and $I_{rear,albedo}$ is the irradiance at the rear coming via albedo reflection. It should be noted that the term "direct" does not refer to direct irradiance, since it includes both direct and diffuse radiation.

C.2.1 The irradiance at the front directly from the vertices

The first component of the total irradiance is calculated in the same way as for the mono-facial modules. The irradiance of this component is the sum as the irradiance of the vertices that can reach the front of the module directly, multiplied with the cosine of the Angle of Incidence (AOI). This can be written as:

$$I_{front,direct} = \sum_{i=1}^{160} I_i \cdot \max\left[\cos(AOI_i), 0\right] \tag{C.2}$$

,where I_i is the irradiance coming from vertex i, and the term $\max\left[\cos(AOI_i), 0\right]$ is used to only include vertices that can reach the front of the module.

C.2.2 The irradiance at the rear directly from the vertices

If the module is tilted, some of the vertices might be able to reach the rear of the module directly. This can be calculated in a similar way as the previous component. The only difference is that the normal angle of the rear side should be used. The azimuth and the altitude of the rear side can be calculated with the following equations:

$$\text{Azimuth}_{rear} = \text{Azimuth}_{front} + 180^o \tag{C.3}$$

$$\text{Altitude}_{rear} = -\text{Altitude}_{front} \tag{C.4}$$

The irradiance at the rear directly from the vertices can be calculated by using the following equation:

$$I_{rear,direct} = \sum_{i=1}^{160} I_i \cdot \max\left[\cos(AOI_{rear,i}), 0\right] \tag{C.5}$$

,where $AOI_{rear,i}$ is the angle of incidence for the rear side.

C.2.3 The irradiance at the rear via albedo reflection

This component is the most complicated to calculate, since it is more complicated to determine which vertices can reach the rear side. Also, there might be vertices who can only reach certain cells, but not the whole module. Because the model assumes that every cell receives the same irradiance, it is defined that only the vertices that can reach the middle of the module are included for albedo reflection.

A vertex can reach the module if a straight (reflected) line can be drawn from the vertex to the middle of the rear side with only one reflection. This is done by reflection the PV panel with respect to the ground, as shown in the Figure C.1

(a) This vertex is able to reach the rear side of the PV panel via albedo reflection.

(b) This vertex is not able to reach the rear side of the PV panel via reflection.

Figure C.1: A vertex is able to included for albedo reflection if it is able to reach the middle of the module via one reflection.

To determine whether a vertex should be included for albedo reflection, the altitude of that vertex is compared with a critical angle ϕ_{crit}. The critical angle can be calculated by:

$$\phi_{crit} = 90 - \tan^{-1}\left(\frac{d}{h}\right) \tag{C.6}$$

,where d and h are defined in Figure C.2.

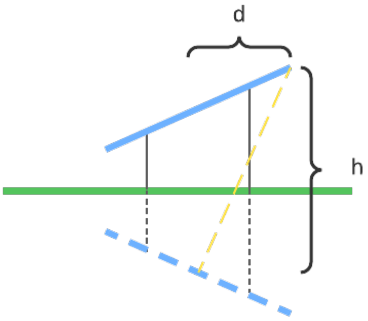

Figure C.2: The horizontal distance between the middle of the mirrored module and the edge (d), and the vertical distance between the edge and the middle of the mirrored module (h) are needed to calculate the critical angle.

The actual value for d or h depends on what the azimuth of the sun is. These values are calculated for the different regions in which the azimuth can be. The equations of l and h are shown in Figure C.3. In the equations shown, the following notations are used:

- H_{mod} is the height of the module.
- L_{mod} is the length of the module.
- W_{mod} is the width of the module.
- θ_{tilt} is the tilt of the module.

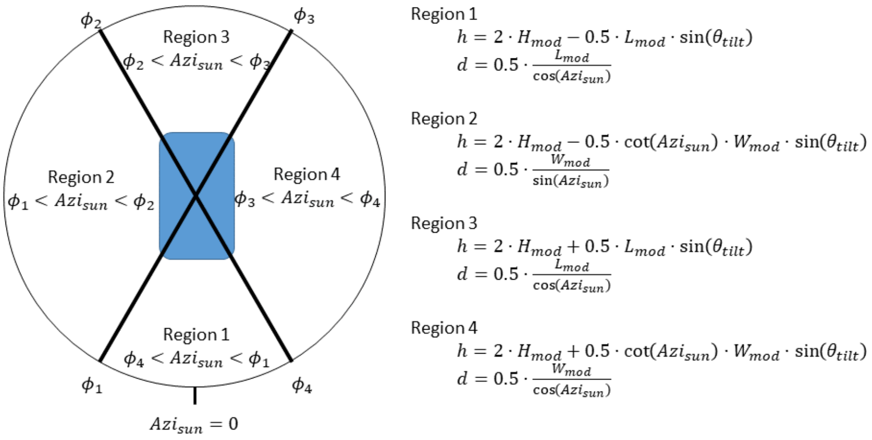

Figure C.3: This vertex is not able to reach the rear side of the PV panel via reflection.

If the altitude of the sun is higher than the critical angle, this vertex is not accounted for albedo reflection. This means that the irradiance via albedo reflection can be calculated as

$$I_{rear,albedo} = \sum_{i=1}^{160} I_i \cdot \cos(AOI_{albedo,i}) \cdot H\left(\phi_{crit} - alti_{sun}\right), \tag{C.7}$$

where $AOI_{albedo,I}$ is the angle of incidence for the albedo reflection, and $H(x)$ is the Heaviside step function [124].

After all components have been calculated, the same correction is applied as for the normal irradiance model.

C.3 A detailed discussion of the mono-facial module

The loss distribution of the mono-facial module is briefly discussed in Section 4.3. Here a detailed discussion is provided. The losses are discussed per category.

C.3.1 The fundamental losses of the mono-facial c-Si module

An overview of the fundamental losses of the mono-facial module is presented in Table C.2. The thermalization and below bandgap losses have increased and decreased respectively compared to STC conditions. This is because the irradiance received outdoors is blue shifted compared to the irradiance at test conditions. The difference is the largest for Lagos and the smallest for Delft, since the blue shift is the greatest in Lagos and the weakest in Delft.

The Carnot and angle mismatch losses depend on the difference between the bandgap energy and the optimal voltage. At real-world operating conditions, there is typically less irradiance than at STC, leading to a decrease of the optimal voltage. This leads to an increase of both the Carnot and angle mismatch losses.

Table C.2: The fundamental losses for the mono-facial crystalline silicon module.

	Delft	Lisbon	Lagos	Shanghai	STC
Thermalization [%]	32.7	33.2	33.8	33.4	31.7
Below bandgap [%]	15.7	15.5	15.1	15.4	19.2
Emission losses [%]	1.7	1.8	1.8	1.8	1.6
Carnot losses [%]	2.7	2.7	2.8	2.7	2.4
Angle mismatch [%]	13.8	13.8	14.1	13.9	12.3
Non-ideality effect [%]	-1.4	-1.4	-1.4	-1.4	-1.3

C.3.2 The optical losses of the mono-facial c-Si module

The optical losses of the mono-facial cell are summarised in Table C.3. The cell spacing and metal shading losses outdoors are close to these losses at test conditions, because the fraction of non-active area remains the same. The small deviations occur due to differences in the fundamental losses. Because both losses are a fraction of the incoming power without the fundamental losses, a change in fundamental losses results in a change of cell spacing or metal shading losses.

The losses due to reflection are larger at outdoors conditions, because the light is not always reaching the module at a normal angle. The reflection typically increases when light enters at an angle, thus increasing the overall reflection at outdoors conditions. The parasitic absorption does not change significantly since this is not as sensitive to the angle-of-incidence.

Table C.3: The optical losses for the mono-facial crystalline silicon module.

	Delft	Lisbon	Lagos	Shanghai	STC
Cell spacing [%]	2.2	2.2	2.1	2.1	2.1
Metal shading [%]	0.4	0.4	0.4	0.4	0.4
Reflection [%]	1.5	1.5	1.6	1.5	0.7
Parasitic absorption [%]	3.8	3.9	3.9	3.9	3.8

C.3.3 The electrical losses of the mono-facial c-Si module

The system losses of the mono-facial cell are presented in Table C.4. The resistance losses are negligible for both test and outdoors conditions. The series resistance and shunt resistance losses are in the order of 0.001% and 0.01% respectively. This is because the values of the series and shunt resistance are respectively small and high enough to make these losses negligible. However, for other modules, these values can be less ideal, making these losses not negligible [125].

The recombination stays approximately constant for the different locations. The reason for this is that the parameters accounting for the recombination (n and I_0) do not change significantly for different irradiances [126], as shown in Appendix B.2.

Table C.4: The electric losses for the mono-facial crystalline silicon module.

	Delft	Lisbon	Lagos	Shanghai	STC
Series resistance [%]	0.0	0.0	0.0	0.0	0.0
Shunt resistance [%]	0.0	0.0	0.0	0.0	0.0
Voltage recombination [%]	5.1	5.1	5.0	5.0	5.0
Current recombination [%]	1.1	1.1	1.1	1.1	1.0

C.3.4 The system losses of the mono-facial c-Si module

The last category is the system losses, which is presented in Table C.5. The interconnection losses are negligible in all situations due to a low connection resistance. Among the locations, there are fluctuations for the inverter losses. This is due to the fact that the efficiency of the inverter is dependent of the input power. Because there is more irradiance for the PV panels in Lisbon and Lagos, the inverter is more efficient at these locations, reducing the inverter losses.

Table C.5: The system losses for the mono-facial crystalline silicon module.

	Delft	Lisbon	Lagos	Shanghai	STC
Cell interconnection [%]	0.0	0.0	0.0	0.0	0.1
Mismatch losses [%]	0.0	0.0	0.0	0.0	0.0
Cable losses [%]	0.2	0.2	0.2	0.2	-
Inverter losses [%]	1.9	1.3	1.5	1.8	-

C.4 A detailed discussion of the bifacial module

The most important results of the bifacial module are discussed in Section 4.4. A detailed discussion of the loss distribution is presented in this section.

C.4.1 The fundamental losses of the bifacial c-Si module

The distribution of the fundamental losses is shown in Table C.6. The thermalization losses and the below bandgap losses are the same as for the mono-facial module and can be explained with a blue-shift of the spectrum. The emission losses are larger at outdoor locations, which is also similar to the mono-facial module.

The emission losses increase with 0.2%/0.3%, which is due to two causes. The first cause is that there is lower incoming irradiance is lower at outdoors conditions, whereas the amount of emission will not decrease as much. This leads to a relative increase of emission. The other cause is the higher module temperature. At outdoors condition, the temperature of the module can be higher than the temperature at STC, which is shown in Appendix C.7. Since a higher temperature increases the emission, the emission losses increase. Also, this explains the fact that Lagos has slightly more emission losses than the other locations.

Both the Carnot and angle mismatch losses are larger at real-world operating conditions than at test conditions. The reason for this is that the optimal voltage decreases at real-world operating conditions, similar to the mono-facial modules.

Table C.6: The fundamental losses for the bifacial crystalline silicon module.

	Delft	Lisbon	Lagos	Shanghai	B-STC
Thermalization [%]	32.7	33.2	33.8	33.4	31.7
Below bandgap [%]	15.7	15.5	15.2	15.4	19.2
Emission losses [%]	1.8	1.8	1.9	1.8	1.6
Carnot losses [%]	2.7	2.7	2.8	2.7	2.4
Angle mismatch [%]	14.5	14.5	14.8	14.6	12.9
Non-ideality effect [%]	-1.3	-1.3	-1.3	-1.3	-1.3

C.4.2 The optical losses of the bifacial c-Si module

The optical losses of the bifacial module are presented in Table C.7. The non-active area losses (cell spacing and metal shading) are all similar since the fraction of non-active area is the same for all situations.

The reflection losses have increased, because the light is not always reaching the cell at the normal angle, similar to the mono-facial module.

Table C.7: The optical losses for the bifacial crystalline silicon module.

	Delft	Lisbon	Lagos	Shanghai	B-STC
Cell spacing [%]	2.1	2.1	2.1	2.1	2.1
Metal shading [%]	0.4	0.4	0.4	0.4	0.4
Reflection [%]	2.1	2.1	2.3	2.3	1.1
Parasitic absorption [%]	3.5	3.5	3.6	3.5	3.4

C.4.3 The electrical losses of the bifacial c-Si module

The electrical losses for the bifacial module (shown in Table C.8) follow the same trend as the mono-facial module. Both resistance losses are negligible, and the recombination losses are similar to the test conditions.

C.4.4 The system losses of the bifacial c-Si module

The system losses of the bifacial module are presented in Table C.9. The cell interconnection losses become negligible at real-world operating conditions (in the range of 0.01%), due to a lower output

Table C.8: The electric losses for the bifacial crystalline silicon module.

	Delft	Lisbon	Lagos	Shanghai	B-STC
Series resistance [%]	0.0	0.0	0.0	0.0	0.0
Shunt resistance [%]	0.0	0.0	0.0	0.0	0.0
Voltage recombination [%]	4.3	4.4	4.3	4.2	4.4
Current recombination [%]	1.1	1.1	1.1	1.1	1.2

current than at STC. Similar to the mono-facial module, the inverter losses are the highest for Delft and Shanghai since they have lower irradiance.

Table C.9: The system losses for the bifacial crystalline silicon module.

	Delft	Lisbon	Lagos	Shanghai	B-STC
Cell interconnection [%]	0.0	0.0	0.0	0.0	0.1
Mismatch losses [%]	0.0	0.0	0.0	0.0	0.0
Cable losses [%]	0.2	0.2	0.2	0.2	-
Inverter losses [%]	1.7	1.2	1.3	1.6	-

C.5 A detailed discussion of the 2T tandem module

The loss distribution of the mono-facial module is shortly discussed in Section 4.5. Here a detailed discussion per category is provided.

C.5.1 The fundamental losses of the 2T tandem module

The fundamental losses of the two-terminal tandem module are shown in Table C.10. At outdoors conditions, the thermalization and below bandgap losses have increased and decreased respectively due to the blue shift, which is similar to the other modules.

The emission losses at outdoors conditions have increased compared to results at test conditions. This is due to a lower incoming irradiance and higher module temperature, as explained in Section 4.4. The emission loss is the largest in Lagos, due to a higher module temperature.

Table C.10: The fundamental losses for the 2T tandem perovskite/silicon module.

	Delft	Lisbon	Lagos	Shanghai	STC
Thermalization [%]	19.4	19.7	20.2	19.9	18.8
Below bandgap [%]	15.7	15.5	15.1	15.4	19.2
Emission losses [%]	2.5	2.6	2.7	2.6	2.3
Carnot losses [%]	3.5	3.5	3.6	3.5	3.1
Angle mismatch [%]	14.0	14.0	14.3	14.1	12.5
Non-ideality effect [%]	-1.3	-1.4	-1.4	-1.4	-1.3

C.5.2 The optical losses of the 2T tandem module

The optical losses (shown in Table C.11) are similar for all locations. The only significant difference are the reflection losses, which increase for real-world operating conditions. This is due to fact that light is not always reaching the module at a normal angle, similar to the other modules.

Table C.11: The optical losses for the 2T tandem perovskite/silicon module.

	Delft	Lisbon	Lagos	Shanghai	STC
Cell spacing [%]	2.9	2.9	2.8	2.9	2.8
Metal shading [%]	0.5	0.5	0.5	0.5	0.5
Reflection [%]	3.4	3.4	3.6	3.5	2.5
Parasitic absorption [%]	3.2	3.3	3.3	3.3	3.1

C.5.3 The electrical losses of the 2T tandem module

The distribution of the electrical losses for the two-terminal tandem module are presented in Table C.12. The resistance losses are the same at each location. Also, the shunt resistance losses are higher for the two-terminal tandem module than for the crystalline silicon modules, due to a lower shunt resistance of perovskite.

The voltage recombination losses increase at outdoors conditions, whereas this remained constant for the crystalline silicon modules. The reason for this is that the perovskite used has a different irradiance dependence. Both the ideality factor and the saturation current density increase for a lower implied photo-current density (shown in Appendix B.2. This leads to a higher voltage loss, which explains the increase in voltage recombination.

Table C.12: The electric losses for the 2T tandem perovskite/silicon module.

	Delft	Lisbon	Lagos	Shanghai	STC
Series resistance [%]	0.0	0.0	0.0	0.0	0.0
Shunt resistance [%]	0.8	0.8	0.8	0.8	0.8
Voltage recombination [%]	6.8	6.9	7.0	6.9	6.5
Current recombination [%]	1.2	1.1	1.2	1.2	1.2

C.5.4 The system losses of the 2T tandem module

The system losses are shown in Table C.13. For the locations with a lower energy yield, the inverter losses are larger. This is in line with the inverter losses for other modules. Furthermore, the inverter losses for the tandem module are larger than for the c-Si modules. The reason for this, is that tandem modules have in general a lower output current, which lowers the efficiency.

C.6 A detailed discussion of the 3T tandem module

The most important results of the three terminal tandem module is discussed in Section 4.6. Here, a detailed discussion is given on all results.

Table C.13: The system losses for the 2T tandem perovskite/silicon module.

	Delft	Lisbon	Lagos	Shanghai	STC
Cell interconnection [%]	0.0	0.0	0.0	0.0	0.0
Mismatch losses [%]	0.3	0.2	0.2	0.2	0.0
Cable losses [%]	0.3	0.3	0.3	0.3	-
Inverter losses [%]	2.6	1.8	2.0	2.4	-

C.6.1 The fundamental losses of the 3T tandem module

The fundamental losses of the 3T tandem modules are shown in Table C.14. The blue-shift in the spectrum (as discussed for the other modules) has an impact on the thermalization and the below bandgap losses. Also, it can be seen that there is more emission outdoors, as described before. It is also the highest in Lagos since this location has the highest temperature.

Another significant difference is that both the Carnot and Angle mismatch losses increase compared to test conditions. The reason for this, is that the optimal voltage is lower for real-world operating conditions, than at test conditions. This leads to an increase of the Carnot voltage and the angle mismatch voltage, as discussed in Appendix C.8.

Table C.14: The fundamental losses for the 3T tandem perovskite/silicon module.

	Delft	Lisbon	Lagos	Shanghai	STC
Thermalization [%]	19.4	19.7	20.2	19.9	18.8
Below bandgap [%]	15.7	15.5	15.1	15.4	19.2
Emission losses [%]	2.5	2.6	2.7	2.6	2.3
Carnot losses [%]	3.5	3.5	3.6	3.5	3.1
Angle mismatch [%]	14.0	14.0	14.3	14.1	12.5
Non-ideality effect [%]	-1.9	-1.9	-2.0	-1.9	-1.8

C.6.2 The optical losses of the 3T tandem module

The optical losses are summarised in Table C.15. The non-active area losses are similar for all locations. The reflection increases when the module is located outdoors, which is due to more oblique angles of the incoming light. This is similar to the reflection losses for other modules.

Table C.15: The optical losses for the 3T tandem perovskite/silicon module.

	Delft	Lisbon	Lagos	Shanghai	STC
Cell spacing [%]	2.9	2.9	2.9	2.9	2.9
Metal shading [%]	0.5	0.5	0.5	0.5	0.5
Reflection [%]	3.4	3.4	3.5	3.5	2.5
Parasitic absorption [%]	3.2	3.2	3.3	3.2	3.0

C.6.3 The electrical losses of the 3T tandem module

The electrical losses for the different locations are shown in Table C.16. It can be seen that the resistance losses are approximately the same for all locations.

The voltage recombination loss is 0.6%-0.7% higher for real-world operating conditions. The reason for this, is that the maximum power point decreases more than the optimal voltage with respect to test conditions, shown in Appendix C.8. This leads to an increase of the non-radiative recombination.

Table C.16: The electric losses for the 3T tandem perovskite/silicon module.

	Delft	Lisbon	Lagos	Shanghai	STC
Series resistance [%]	0.0	0.0	0.0	0.0	0.0
Shunt resistance [%]	1.3	1.0	1.1	1.2	0.9
Voltage recombination [%]	8.8	8.8	8.9	8.8	8.2
Current recombination [%]	1.2	1.3	1.2	1.2	1.2

C.6.4 The system losses of the 3T tandem module

The system losses of the three-terminal tandem modules are shown in Figure C.17. The cell interconnection, the mismatch and the cable losses are all similar for the different locations. The only significant difference is the variation in the inverter losses. This is because inverters are less efficient at a lower power, which is similar to the other modules.

Table C.17: The system losses for the 3T tandem perovskite/silicon module.

	Delft	Lisbon	Lagos	Shanghai	STC
Cell interconnection [%]	0.2	0.2	0.2	0.2	0.3
Mismatch losses [%]	1.5	1.6	1.5	1.5	1.7
Cable losses [%]	0.2	0.2	0.2	0.2	-
Inverter losses [%]	1.8	1.2	1.4	1.6	-

C.7 The module temperature at different locations

The temperature of the module affects the performance. Therefore it is important to know the temperature of the different modules at the different locations. The temperature of the mono-facial, bifacial, 2T tandem, and 3T tandem are shown in Figure C.4, C.5, C.6, and C.7

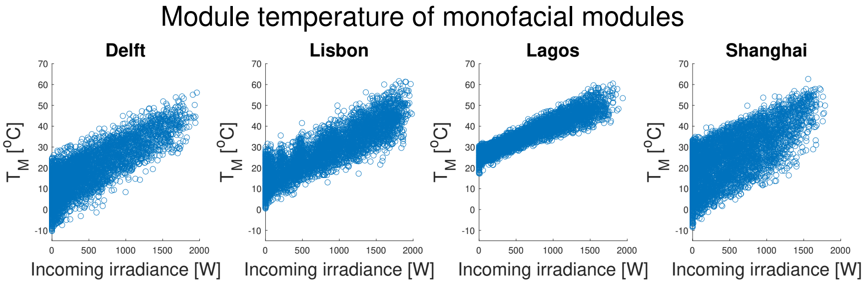

Figure C.4: The module temperature of the mono-facial module at the four different locations.

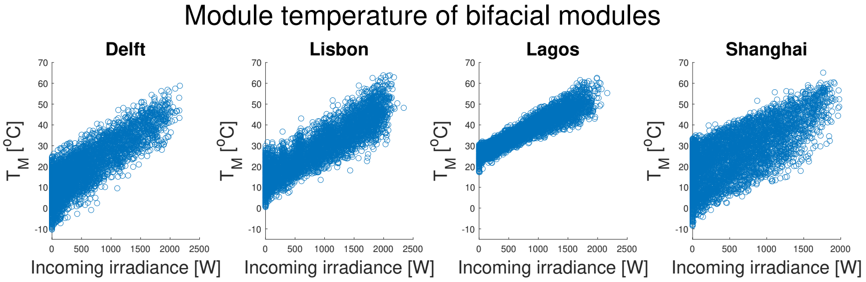

Figure C.5: The module temperature of the bifacial module at the four different locations.

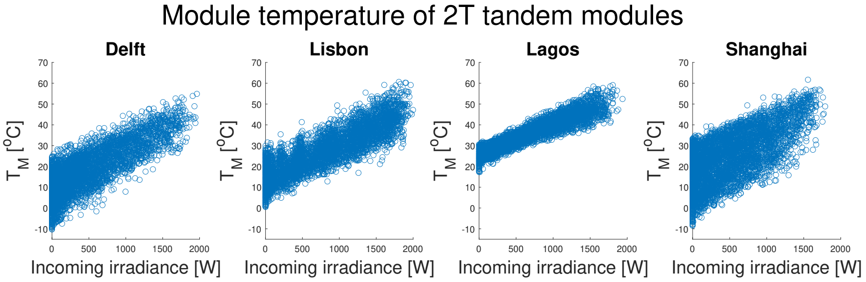

Figure C.6: The module temperature of the 2T tandem module at the four different locations.

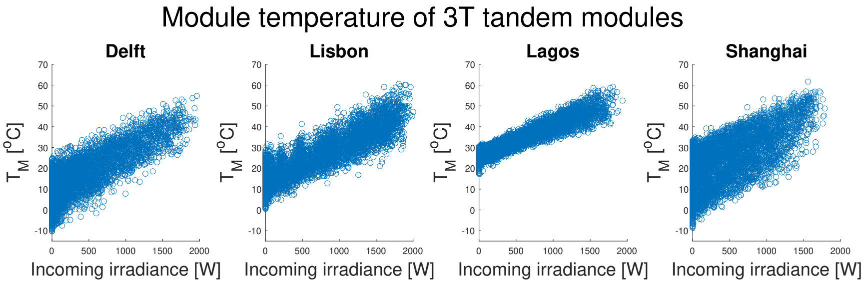

Figure C.7: The module temperature of the 3T tandem module at the four different locations.

C.8 The optimal voltage at outdoors conditions

The optimal voltage is defined as the voltage that maximises the following equations:

$$P = V_{opt} \cdot q \left(\int_{E_g}^{\infty} \phi_{in}(E) dE - \int_{E_g}^{\infty} \phi_E \left(E, T_{cell}, q \cdot V_{opt}, \Omega_{emit} \right) dE \right) \tag{C.8}$$

Because the irradiance varies at different locations, the optimum voltage is also different. The values of the optimum voltage and maximum power point voltage of used materials in the modules are shown in Table C.18.

Table C.18: The values of the optimal voltage and maximum power point voltage of the different material used. The values are irradiance weighted.

	Delft	Lisbon	Lagos	Shanghai	STC
c-Si mono-facial V_{opt} [V]	0.75	0.75	0.74	0.74	0.77
c-Si mono-facial V_{mpp} [V]	0.61	0.61	0.59	0.60	0.63
c-Si bifacial V_{opt} [V]	0.73	0.73	0.72	0.73	0.76
c-Si bifacial V_{mpp} [V]	0.61	0.61	0.59	0.60	0.63
c-Si 2T V_{opt} [V]	0.75	0.75	0.74	0.74	0.77
c-Si 2T V_{mpp} [V]	0.61	0.60	0.59	0.60	0.62
Perovskite 2T V_{opt} [V]	1.26	1.26	1.24	1.25	1.28
Perovskite 2T V_{mpp} [V]	1.03	1.03	1.01	1.02	1.06
c-Si 3T V_{opt} [V]	0.75	0.75	0.74	0.74	0.77
c-Si 3T V_{mpp} [V]	0.60	0.59	0.58	0.59	0.62
Perovskite 3T V_{opt} [V]	1.26	1.26	1.24	1.25	1.28
Perovskite 3T V_{mpp} [V]	0.96	0.96	0.94	0.95	1.00

D. Appendix optimisations

D.1 The ASA simulations for a different perovskite thickness

In section 5.3, it is discussed that the thickness of perovskite will be varied to observe the effect on the loss distribution. This requires simulations in the Advanced Semiconductor Simulator (ASA) to model the electrical behaviour. The ASA simulations of the different thicknesses are shown in Figure D.1, D.2, D.3, and D.4.

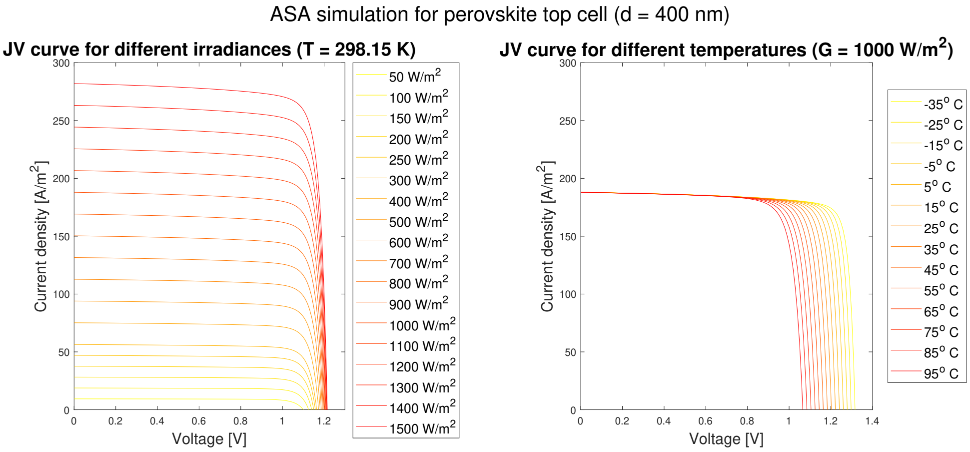

Figure D.1: The ASA simulation of the perovskite top cell with a thickness of 400 nm.

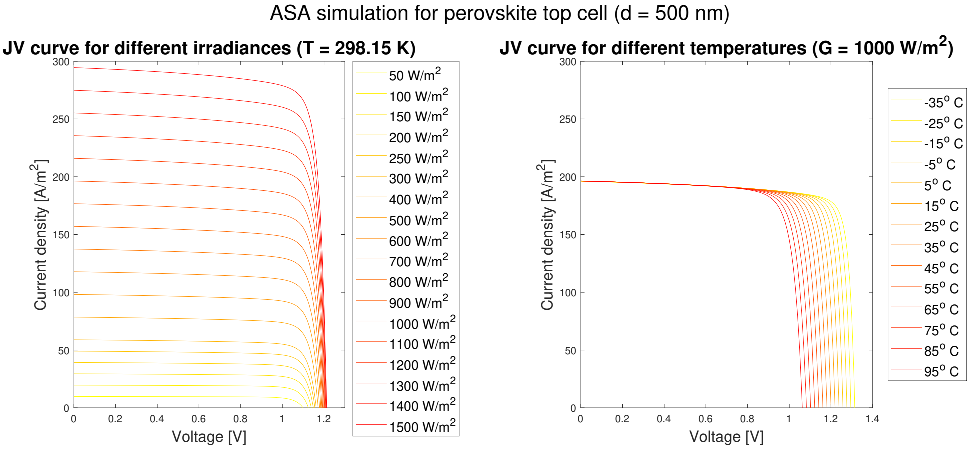

Figure D.2: The ASA simulation of the perovskite top cell with a thickness of 500 nm.

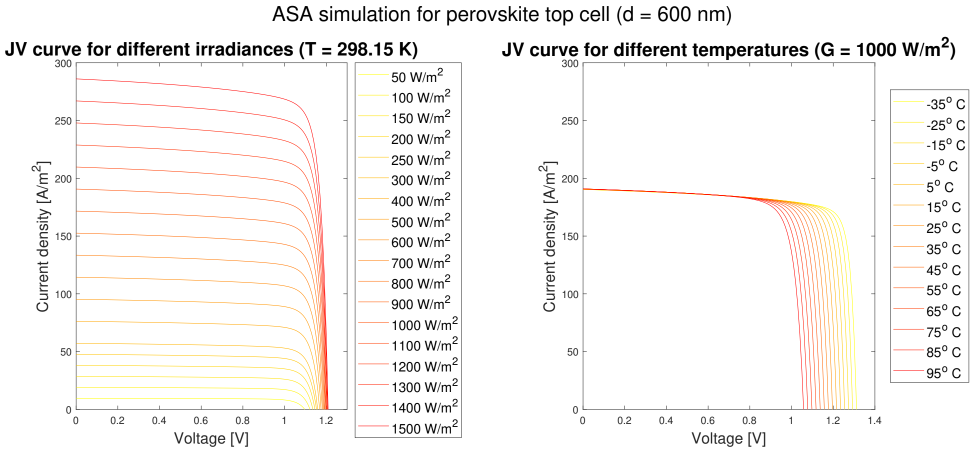

Figure D.3: The ASA simulation of the perovskite top cell with a thickness of 600 nm.

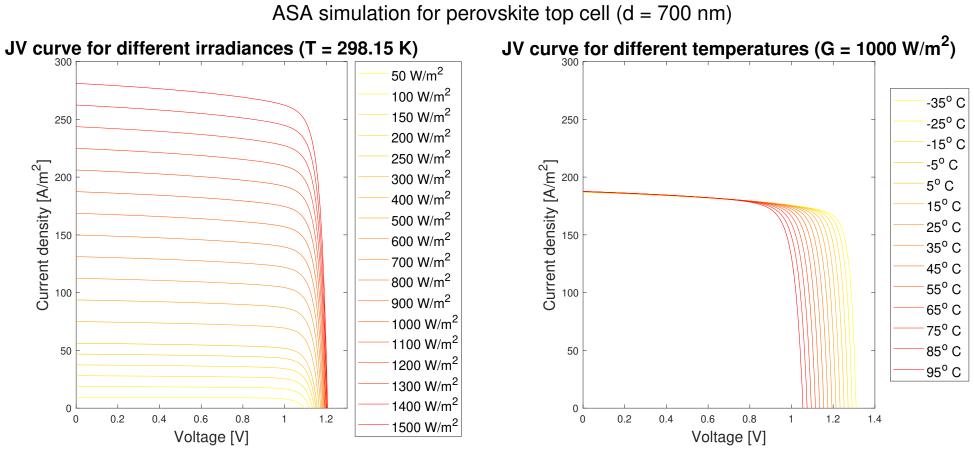

Figure D.4: The ASA simulation of the perovskite top cell with a thickness of 700 nm.

D.2 The results for tracking

In Section 5.1, only the results of Delft are shown. The loss distributions of the other locations with tracking are shown in Figure D.5, D.6, and D.7.

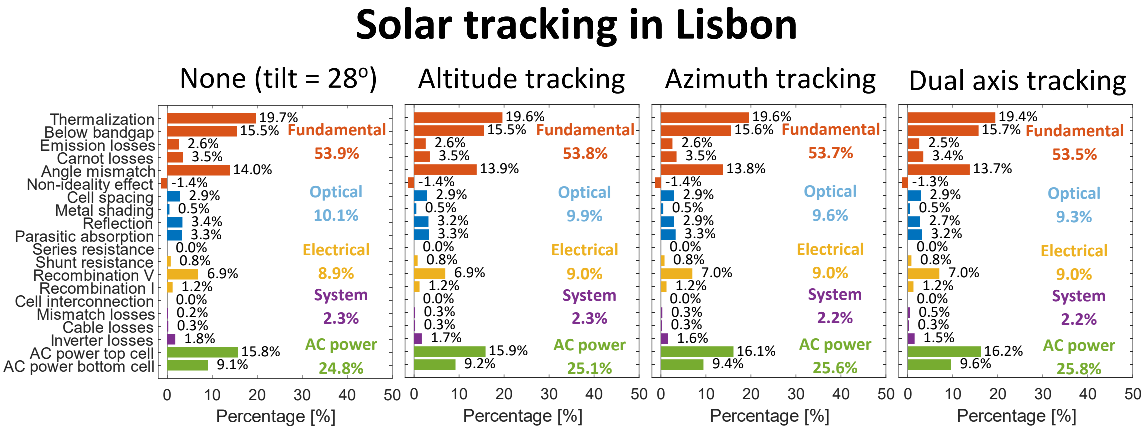

Figure D.5: The loss distributions for the tracking systems in Lisbon. All values are yearly irradiance weighted.

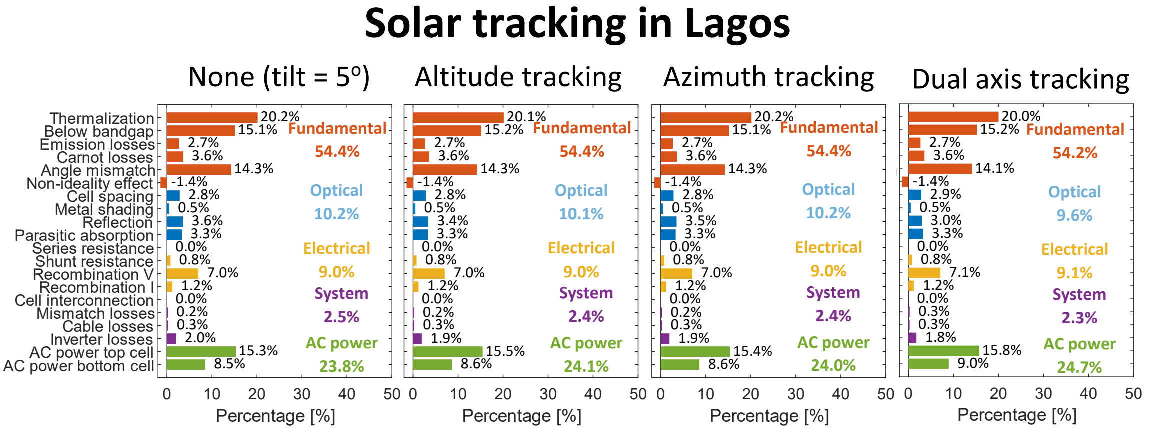

Figure D.6: The loss distributions for the tracking systems in Lagos. All values are yearly irradiance weighted.

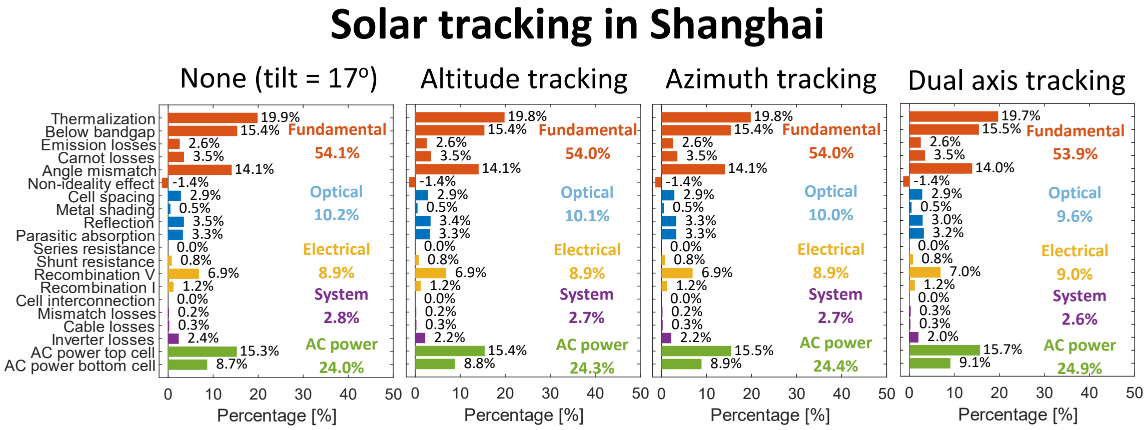

Figure D.7: The loss distributions for the tracking systems in Shanghai. All values are yearly irradiance weighted.

D.3 The results for active cooling

In Section 5.2, the loss distributions for Delft are presented with different temperatures. The results of the other locations are shown in Figure D.8, D.9, and D.10.

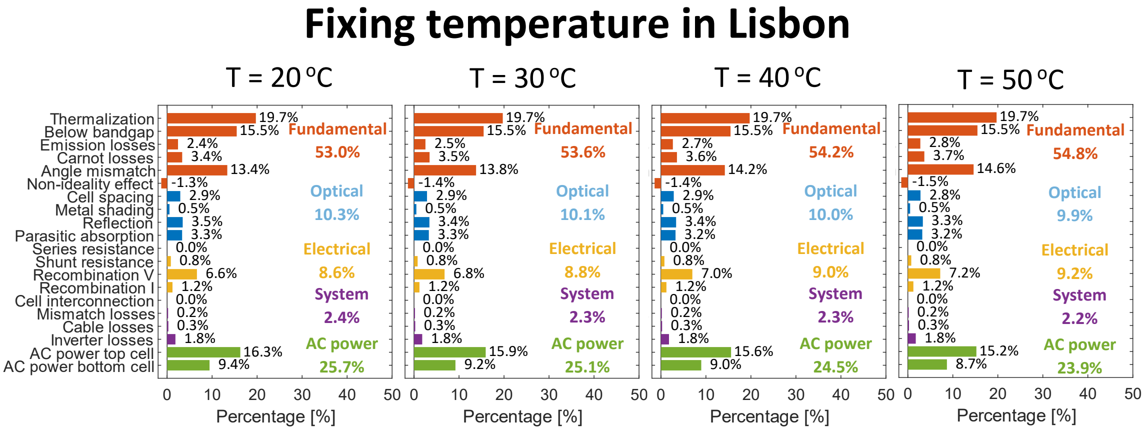

Figure D.8: The loss distributions for active cooling in Lisbon. All values are yearly irradiance weighted.

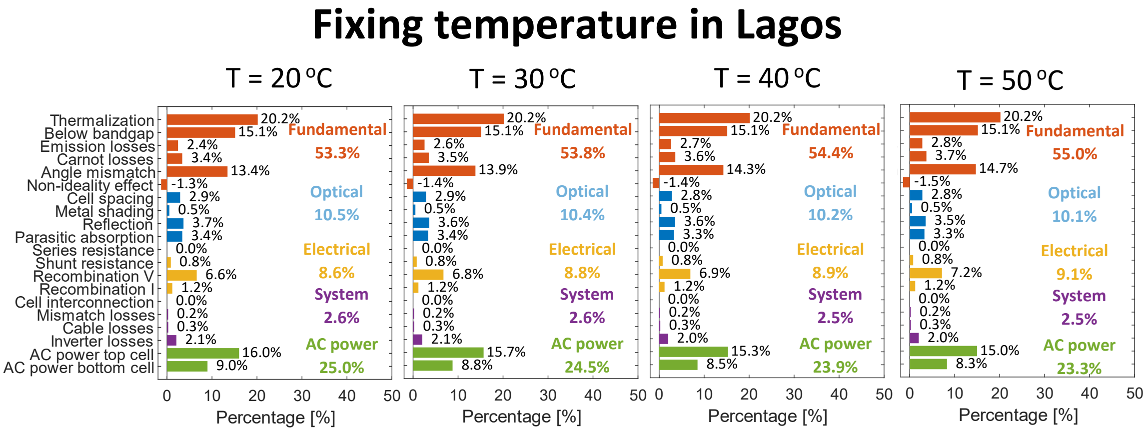

Figure D.9: The loss distributions for active cooling in Lagos. All values are yearly irradiance weighted.

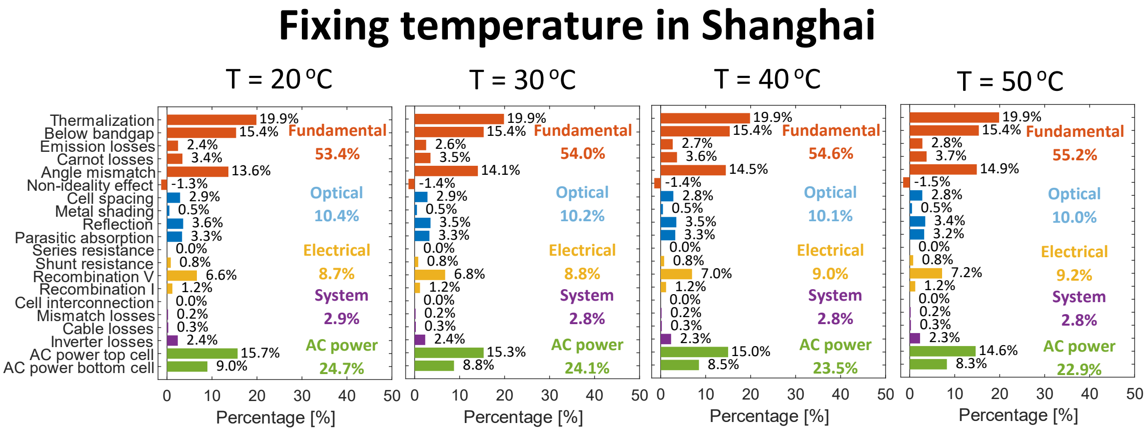

Figure D.10: The loss distributions for active cooling in Shanghai. All values are yearly irradiance weighted.

D.4 The results for changing the perovskite thickness

In Section 5.3, the loss distributions for Delft are presented with different perovskite thicknesses. The results of the other locations are shown in Figure D.11, D.12, and D.13.

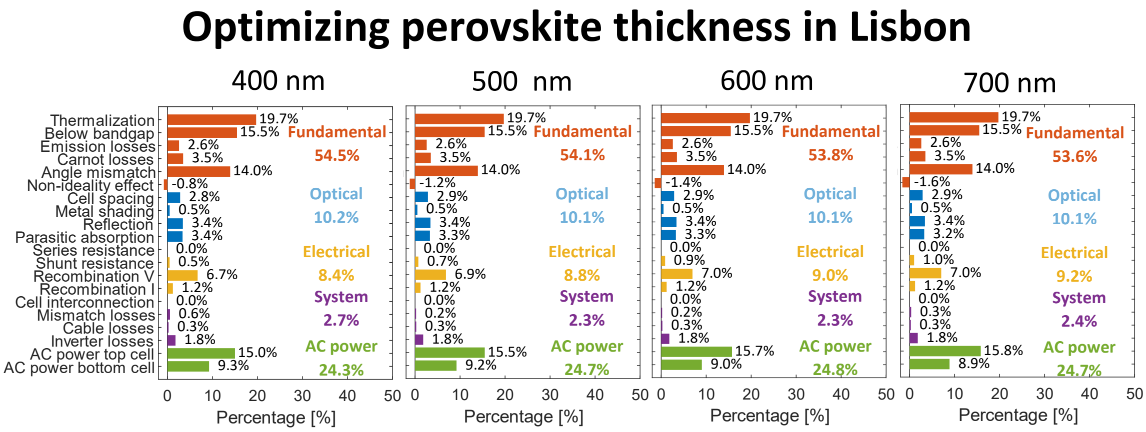

Figure D.11: The loss distributions for increasing the perovskite thickness in Lisbon. All values are yearly irradiance weighted.

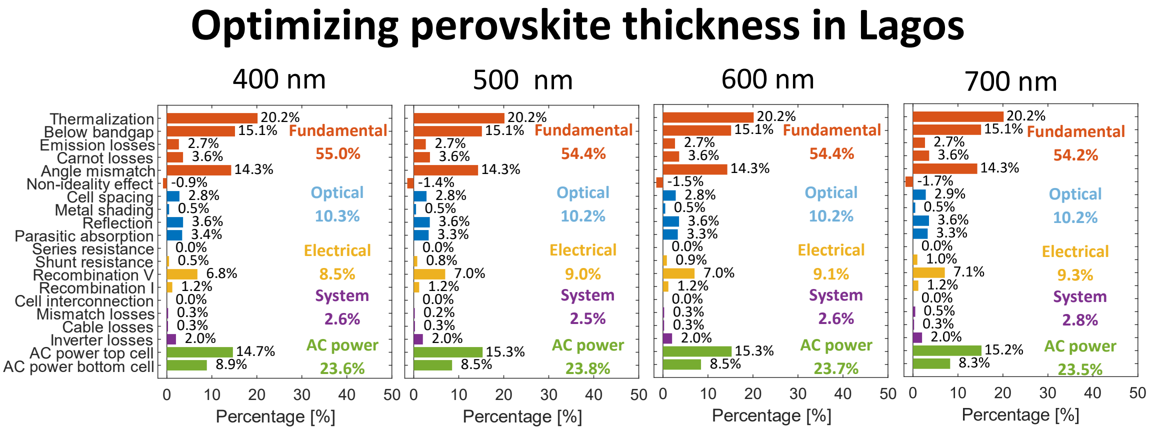

Figure D.12: The loss distributions for increasing the perovskite thickness in Lagos. All values are yearly irradiance weighted.

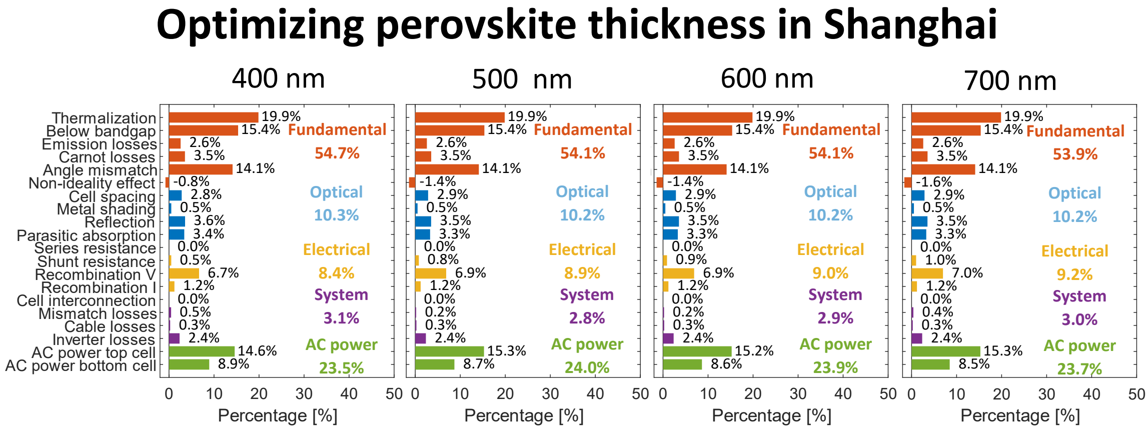

Figure D.13: The loss distributions for increasing the perovskite thickness in Shanghai. All values are yearly irradiance weighted.

Bibliography

[1] European Commission, “Communication from the comission to the European parliament, the European council, the council, the European economic and social committee and the committee of the regions,” European Commission, Brussel, Tech. Rep., 12 2019.

[2] United Nations Framework Convention on Climate Change(UNFCCC), “The Paris Agreement,” UNFCCC, Paris, Tech. Rep., 11 2018.

[3] IRENA, “Renewable capacity statistics 2021 International Renewable Energy Agency (IRENA),” Abu Dhabi, Tech. Rep., 2021.

[4] A. G. Aberle, W. Zhang, and B. Hoex, “Advanced loss analysis method for silicon wafer solar cells,” *Energy Procedia*, vol. 8, pp. 244–249, 1 2011.

[5] I. Haedrich, D. C. Jordan, and M. Ernst, “Methodology to predict annual yield losses and gains caused by solar module design and materials under field exposure,” *Solar Energy Materials and Solar Cells*, vol. 202, 11 2019.

[6] S. Agarwal and P. R. Nair, “Performance loss analysis and design space optimization of perovskite solar cells,” *Journal of Applied Physics*, vol. 124, no. 18, 11 2018.

[7] H. Liu, C. D. Rodríguez-Gallegos, Z. Liu, T. Buonassisi, T. Reindl, and I. M. Peters, “A Worldwide Theoretical Comparison of Outdoor Potential for Various Silicon-Based Tandem Module Architecture,” *Cell Reports Physical Science*, vol. 1, no. 4, 4 2020.

[8] B. F. Towler, “Solar Power,” in *The Future of Energy*. Elsevier, 2014, pp. 161–185.

[9] N. Sönnichsen, “Primary energy consumption worldwide from 2000 to 2020,” 8 2021. [Online]. Available: https://www.statista.com/statistics/265598/consumption-of-primary-energy-worldwide/

[10] A. Khaligh and O. C. Onar, “Energy Sources,” in *Power Electronics Handbook*. Elsevier, 2018, pp. 725–765.

[11] A. Smets, K. Jäger, O. Isabella, R. Van Swaaij, and M. Zeman, *Solar Energy*. Cambridge: UIT Cambridge Limited, 2016.

[12] “Standard Solar Spectra — PVEducation.” [Online]. Available: https://www.pveducation.org/pvcdrom/appendices/standard-solar-spectra

[13] D. A. Neamen, *Semiconductor Physics and Devices*, 4th ed. New York: McGraw-Hill Education, 2012.

[14] T. Ma, Z. Guo, L. Shen, X. Liu, Z. Chen, Y. Zhou, and X. Zhang, “Performance modelling of photovoltaic modules under actual operating conditions considering loss mechanism and energy distribution,” *Applied Energy*, vol. 298, 9 2021.

[15] W. Shockley and H. J. Queisser, “Detailed Balance Limit of Efficiency of p-n Junction Solar Cells,” *Journal of Applied Physics*, vol. 32, no. 3, pp. 510–519, 3 1961.

[16] A. Richter, M. Hermle, and S. W. Glunz, “Reassessment of the Limiting Efficiency for Crystalline Silicon Solar Cells,” *IEEE Journal of Photovoltaics*, vol. 3, no. 4, pp. 1184–1191, 10 2013.

[17] T. Ma, H. Yang, and L. Lu, "Development of a model to simulate the performance characteristics of crystalline silicon photovoltaic modules/strings/arrays," *Solar Energy*, vol. 100, pp. 31–41, 2 2014.

[18] A. Chouder, S. Silvestre, B. Taghezouit, and E. Karatepe, "Monitoring, modelling and simulation of PV systems using LabVIEW," *Solar Energy*, vol. 91, pp. 337–349, 5 2013.

[19] K. Ramalingam and C. Indulkar, "Solar Energy and Photovoltaic Technology," in *Distributed Generation Systems.* Elsevier, 2017, pp. 69–147.

[20] H. Plagwitz and R. Brendel, "Analytical model for the diode saturation current of point-contacted solar cells," *Progress in Photovoltaics: Research and Applications*, vol. 14, no. 1, pp. 1–12, 1 2006.

[21] M. Leilaeioun and Z. C. Holman, "Accuracy of expressions for the fill factor of a solar cell in terms of open-circuit voltage and ideality factor," *Journal of Applied Physics*, vol. 120, no. 12, p. 123111, 9 2016.

[22] R. J. Handy, "Theoretical analysis of the series resistance of a solar cell," *Solid-State Electronics*, vol. 10, no. 8, pp. 765–775, 8 1967.

[23] C. M. Proctor and T.-Q. Nguyen, "Effect of leakage current and shunt resistance on the light intensity dependence of organic solar cells," *Applied Physics Letters*, vol. 106, no. 8, p. 083301, 2 2015.

[24] A. Jain, "Exact analytical solutions of the parameters of real solar cells using Lambert W-function," *Solar Energy Materials and Solar Cells*, vol. 81, no. 2, pp. 269–277, 2 2004.

[25] A. De Vos, "Detailed balance limit of the efficiency of tandem solar cells," *J. Phys. D: Appl. Phys*, vol. 13, 1980.

[26] O. Dupré, B. Niesen, S. De Wolf, and C. Ballif, "Field Performance versus Standard Test Condition Efficiency of Tandem Solar Cells and the Singular Case of Perovskites/Silicon Devices," *Journal of Physical Chemistry Letters*, vol. 9, no. 2, pp. 446–458, 1 2018.

[27] Y. Jiang, I. Almansouri, S. Huang, T. Young, Y. Li, Y. Peng, Q. Hou, L. Spiccia, U. Bach, Y.-B. Cheng, M. A. Green, and A. Ho-Baillie, "Optical analysis of perovskite/silicon tandem solar cells," *Journal of Materials Chemistry C*, vol. 4, no. 24, 2016.

[28] Z. Wang, Z. Song, Y. Yan, S. F. Liu, and D. Yang, "Perovskite—a Perfect Top Cell for Tandem Devices to Break the S–Q Limit," *Advanced Science*, vol. 6, no. 7, p. 1801704, 4 2019.

[29] S. R. Kurtz, P. Faine, and J. M. Olson, "Modeling of two-junction, series-connected tandem solar cells using top-cell thickness as an adjustable parameter," *Journal of Applied Physics*, vol. 68, no. 4, pp. 1890–1895, 8 1990.

[30] E. L. Warren, W. E. Mcmahon, M. Rienäcker, K. T. Vansant, R. C. Whitehead, R. Peibst, and A. C. Tamboli, "A Taxonomy for Three-Terminal Tandem Solar Cells," pp. 1233–1242, 4 2020.

[31] J. Lehr, M. Langenhorst, R. Schmager, S. Kirner, U. Lemmer, B. S. Richards, C. Case, and U. W. Paetzold, "Energy yield modelling of perovskite/silicon two-terminal tandem PV modules with flat and textured interfaces," *Sustainable Energy & Fuels*, vol. 2, no. 12, 2018.

[32] N.-G. Park, "Perovskite solar cells: an emerging photovoltaic technology," *Materials Today*, vol. 18, no. 2, 3 2015.

[33] A. Julien, J.-B. Puel, P. Lopez-Varo, J.-F. Guillemoles, and S. Collin, "Backside light management of 4-terminal bifacial perovskite/silicon tandem PV modules evaluated under realistic conditions," *Optics Express*, vol. 28, no. 25, p. 37487, 12 2020.

[34] R. Fan, N. Zhou, L. Zhang, R. Yang, Y. Meng, L. Li, T. Guo, Y. Chen, Z. Xu, G. Zheng, Y. Huang, L. Li, L. Qin, X. Qiu, Q. Chen, and H. Zhou, "Toward Full Solution Processed Perovskite/Si Monolithic Tandem Solar Device With PCE Exceeding 20%," *Solar RRL*, vol. 1, no. 11, p. 1700149, 11 2017.

[35] M. A. Green, A. Ho-Baillie, and H. J. Snaith, "The emergence of perovskite solar cells," *Nature Photonics*, vol. 8, no. 7, pp. 506–514, 7 2014.

[36] "Best Research-Cell Efficiency Chart — Photovoltaic Research — NREL." [Online]. Available: https://www.nrel.gov/pv/cell-efficiency.html

[37] A. Purkayastha and A. T. Mallajosyula, "Optical modelling of tandem solar cells using hybrid organic-inorganic tin perovskite bottom sub-cell," *Solar Energy*, vol. 218, 4 2021.

[38] J.-P. Correa-Baena, M. Saliba, T. Buonassisi, M. Grätzel, A. Abate, W. Tress, and A. Hagfeldt, "Promises and challenges of perovskite solar cells," *Science*, vol. 358, no. 6364, pp. 739–744, 11 2017.

[39] S. Philipps, "Photovoltaics Report," Fraunhofer Institute for Solar Energy Systems, Freiburg, Tech. Rep., 7 2021. [Online]. Available: www.ise.fraunhofer.de

[40] S. Taylor, "Abundance of chemical elements in the continental crust: a new table," *Geochimica et Cosmochimica Acta*, vol. 28, no. 8, pp. 1273–1285, 8 1964.

[41] M. R. Vogt, C. Ruiz Tobon, A. Alcañiz, P. Procel, A. Nour El Din, T. Stark, Z. Wang, E. Garcia Goma, J. G. Etxebarria, H. Ziar, M. Zeman, R. Santbergen, and O. Isabella, "Modelling the future's PV Systems using the PVMD Toolbox," Delft University of Technology, Delft, Tech. Rep.

[42] P. Singh and N. Ravindra, "Temperature dependence of solar cell performance—an analysis," *Solar Energy Materials and Solar Cells*, vol. 101, pp. 36–45, 6 2012.

[43] J. C. Fan, "Theoretical temperature dependence of solar cell parameters," *Solar Cells*, vol. 17, no. 2-3, pp. 309–315, 4 1986.

[44] S. Chander, A. Purohit, A. Sharma, Arvind, S. Nehra, and M. Dhaka, "A study on photovoltaic parameters of mono-crystalline silicon solar cell with cell temperature," *Energy Reports*, vol. 1, pp. 104–109, 11 2015.

[45] D. King, J. Kratochvil, and W. Boyson, "Measuring solar spectral and angle-of-incidence effects on photovoltaic modules and solar irradiance sensors," in *Conference Record of the Twenty Sixth IEEE Photovoltaic Specialists Conference - 1997.* IEEE, 1997, pp. 1113–1116.

[46] I. M. Peters, Y. S. Khoo, and T. M. Walsh, "Detailed Current Loss Analysis for a PV Module Made With Textured Multicrystalline Silicon Wafer Solar Cells," *IEEE Journal of Photovoltaics*, vol. 4, no. 2, pp. 585–593, 3 2014.

[47] A. Khanna, T. Mueller, R. A. Stangl, B. Hoex, P. K. Basu, and A. G. Aberle, "A fill factor loss analysis method for silicon wafer solar cells," *IEEE Journal of Photovoltaics*, vol. 3, no. 4, pp. 1170–1177, 2013.

[48] L. Shen, Z. Li, and T. Ma, "Analysis of the power loss and quantification of the energy distribution in PV module," *Applied Energy*, vol. 260, p. 114333, 2 2020.

[49] A. Wang and Y. Xuan, "A detailed study on loss processes in solar cells," *Energy*, vol. 144, pp. 490–500, 2 2018.

[50] C. U. Kim, E. D. Jung, Y. W. Noh, S. K. Seo, Y. Choi, H. Park, M. H. Song, and K. J. Choi, "Strategy for large-scale monolithic Perovskite/Silicon tandem solar cell: A review of recent progress," *EcoMat*, vol. 3, no. 2, 4 2021.

[51] A. Nour El Din, "Improved Electrical Model and Experimental Validation of the PVMD Toolbox Extending the Energy Yield Prediction Model to Tandem PV Modules," Delft University of Technology, Delft, Tech. Rep., 7 2020. [Online]. Available: http://resolver.tudelft.nl/uuid:0cc6ae16-9501-419b-b70a-7a7987c38350

[52] Z. Wang, "Improvements and Experimental Validation of the PVMD Toolbox-an Energy Yield Prediction Model for PV Systems," Delft University of Technology, Delft, Tech. Rep., 6 2019. [Online]. Available: http://repository.tudelft.nl/.

[53] R. Santbergen, T. Meguro, T. Suezaki, G. Koizumi, K. Yamamoto, and M. Zeman, "GenPro4 Optical Model for Solar Cell Simulation and Its Application to Multijunction Solar Cells," *IEEE Journal of Photovoltaics*, vol. 7, no. 3, pp. 919–926, 5 2017.

[54] R. Siegel, "Net radiation method for transmission through partially transparent plates," *Solar Energy*, vol. 15, no. 3, pp. 273–276, 1973.

[55] R. Santbergen, V. Muthukumar, R. Valckenborg, W. van de Wall, A. Smets, and M. Zeman, "Calculation of irradiance distribution on PV modules by combining sky and sensitivity maps," *Solar Energy*, vol. 150, pp. 49–54, 7 2017.

[56] M. Zeman, J. Van Den Heuvel, M. Kroon, J. Willemen, B. Pieters, J. Krč, and S. Solntsev, "Advanced Semiconductor Analysis opto-electronic simulator for amorphous and crystalline semiconductor devices User's Manual," Delft University of Technology, Delft, Tech. Rep., 8 2019.

[57] R. Perez, R. Seals, and J. Michalsky, "All-weather model for sky luminance distribution—Preliminary configuration and validation," *Solar Energy*, vol. 50, no. 3, pp. 235–245, 3 1993.

[58] C. A. Gueymard, "Parameterized transmittance model for direct beam and circumsolar spectral irradiance," *Solar Energy*, vol. 71, no. 5, pp. 325–346, 11 2001.

[59] M. K. Fuentes, "A Simplified Thermal Model for Flat-Plate Photovoltaic Arrays," *Sandia Report*, 1987.

[60] S. R. Valluri, D. J. Jeffrey, and R. M. Corless, "Some applications of the Lambert W function to physics," *Canadian Journal of Physics*, vol. 78, no. 9, pp. 823–831, 9 2000.

[61] J. J. Shynk, “Mathematical Foundations for Linear Circuits and Systems in Engineering,” *Mathematical Foundations for Linear Circuits and Systems in Engineering*, pp. 1–624, 2 2016.

[62] W. Boyson, G. Galbraith, D. King, and S. Gonzalez, “Performance model for grid-connected photovoltaic inverters,” Sandia National Laboratories (SNL), Albuquerque, NM, and Livermore, CA (United States), Tech. Rep., 9 2007.

[63] L. C. Hirst and N. J. Ekins-Daukes, “Fundamental losses in solar cells,” *Progress in Photovoltaics: Research and Applications*, vol. 19, no. 3, pp. 286–293, 5 2011.

[64] O. Dupré, R. Vaillon, and M. Green, “Physics of the temperature coefficients of solar cells,” *Solar Energy Materials and Solar Cells*, vol. 140, pp. 92–100, 9 2015.

[65] W. Bludau, A. Onton, and W. Heinke, “Temperature dependence of the band gap of silicon,” *Journal of Applied Physics*, vol. 45, no. 4, pp. 1846–1848, 4 1974.

[66] T. Dittrich, C. Awino, P. Prajongtat, B. Rech, and M. C. Lux-Steiner, “Temperature Dependence of the Band Gap of CH3NH3PbI3 Stabilized with PMMA: A Modulated Surface Photovoltage Study,” *Journal of Physical Chemistry C*, vol. 119, no. 42, pp. 23 968–23 972, 10 2015. [Online]. Available: https://pubs-acs-org.tudelft.idm.oclc.org/doi/full/10.1021/acs.jpcc.5b07132

[67] W. Ruppel and P. Wurfel, “Upper limit for the conversion of solar energy,” *IEEE Transactions on Electron Devices*, vol. 27, no. 4, pp. 877–882, 4 1980.

[68] M. Robledo, T. R. Rodríguez, R. R. Rodríguez-Guzmán, C. Lévêque, and L. Bojer Madsen, “Carnot factor in solar cell efficiencies,” *Journal of Physics D: Applied Physics*, vol. 33, no. 22, p. 3004, 11 2000. [Online]. Available: https://iopscience.iop.org/article/10.1088/0022-3727/33/22/320https://iopscience.iop.org/article/10.1088/0022-3727/33/22/320/meta

[69] T. Markvart, “Solar cell as a heat engine: energy-entropy analysis of photovoltaic conversion,” *physica status solidi (a)*, vol. 205, no. 12, pp. 2752–2756, 12 2008.

[70] M. A. Alam and M. R. Khan, “Thermodynamic efficiency limits of classical and bifacial multijunction tandem solar cells: An analytical approach,” *Applied Physics Letters*, vol. 109, no. 17, p. 173504, 10 2016.

[71] M. Ryyan Khan and M. A. Alam, “Thermodynamic limit of bifacial double-junction tandem solar cells,” *Applied Physics Letters*, vol. 107, no. 22, p. 223502, 11 2015.

[72] M. A. Alam and M. R. Khan, “Shockley–Queisser triangle predicts the thermodynamic efficiency limits of arbitrarily complex multijunction bifacial solar cells,” *Proceedings of the National Academy of Sciences*, vol. 116, no. 48, pp. 23 966–23 971, 11 2019.

[73] T. Trupke, M. A. Green, and P. Würfel, “Improving solar cell efficiencies by up-conversion of sub-band-gap light,” *Journal of Applied Physics*, vol. 92, no. 7, pp. 4117–4122, 10 2002.

[74] F. Urbach, “The Long-Wavelength Edge of Photographic Sensitivity and of the Electronic Absorption of Solids,” *Physical Review*, vol. 92, no. 5, pp. 1324–1324, 12 1953.

[75] J. D. Dow and D. Redfield, “Toward a Unified Theory of Urbach’s Rule and Exponential Absorption Edges,” *Physical Review B*, vol. 5, no. 2, pp. 594–610, 1 1972.

[76] I. Haedrich, U. Eitner, M. Wiese, and H. Wirth, "Unified methodology for determining CTM ratios: Systematic prediction of module power," *Solar Energy Materials and Solar Cells*, vol. 131, pp. 14–23, 2014.

[77] M. Köntges, H. Schulte-Huxel, S. Blankemeyer, M. R. Vogt, H. Holst, and R. Reineke-Koch, "Measuring the light recovery factor of backsheets in photovoltaic modules," *Solar Energy Materials and Solar Cells*, vol. 186, pp. 175–183, 11 2018.

[78] F. T. Ulaby and U. Ravaioli, *Fundamentals of applied electromagnetics*, 7th ed. Harlow, Essex: Pearson Education Limited, 2015.

[79] M. Stuckings and A. Blakers, "A study of shading and resistive loss from the fingers of encapsulated solar cells," *Solar Energy Materials and Solar Cells*, vol. 59, no. 3, pp. 233–242, 10 1999.

[80] M. A. Green, "Radiative efficiency of state-of-the-art photovoltaic cells," *Progress in Photovoltaics: Research and Applications*, vol. 20, no. 4, pp. 472–476, 6 2012.

[81] M. Green, "Limits on the open-circuit voltage and efficiency of silicon solar cells imposed by intrinsic Auger processes," *IEEE Transactions on Electron Devices*, vol. 31, no. 5, pp. 671–678, 5 1984.

[82] P. J. Davis and P. Rabinowitz, *Methods of numerical integration*, 2nd ed. Mineola: Dover Publications, 1984.

[83] K. C. Yeh and K. C. Kwan, "A comparison of numerical integrating algorithms by trapezoidal, Lagrange, and spline approximation," *Journal of Pharmacokinetics and Biopharmaceutics*, vol. 6, no. 1, pp. 79–98, 2 1978.

[84] C. Faria Lopes Junior, G. Soares Da Silva, P. Sousa Nilo Mendes, P. Sousa Nilo Mendes, J. H. Brandenburger Hoppe, and B. Nunes Myrrha Ribeiro, "Development Of An Application Through Computational Modeling For The Implementation Of The Riemann Sum Method And Trapezoid Rule To Obtain The Approximation Of Areas Under Curves," *IOSR Journal of Research & Method in Education*, 7 2018.

[85] A. Al-Ashouri, E. Köhnen, B. Li, A. Magomedov, H. Hempel, P. Caprioglio, J. A. Márquez, A. B. Morales Vilches, E. Kasparavicius, J. A. Smith, N. Phung, D. Menzel, M. Grischek, L. Kegelmann, D. Skroblin, C. Gollwitzer, T. Malinauskas, M. Jošt, G. Matič, B. Rech, R. Schlatmann, M. Topič, L. Korte, A. Abate, B. Stannowski, D. Neher, M. Stolterfoht, T. Unold, V. Getautis, and S. Albrecht, "Monolithic perovskite/silicon tandem solar cell with 29% efficiency by enhanced hole extraction," *Science*, vol. 370, no. 6522, pp. 1300–1309, 12 2020.

[86] M. K. Yang, "Optical properties of Teflon AF amorphous fluoropolymers," *Journal of Micro/Nanolithography, MEMS, and MOEMS*, vol. 7, no. 3, p. 033010, 7 2008.

[87] M. R. Vogt, "Development of Physical Models for the Simulation of Optical Properties of Solar Cell Modules," Gottfried Wilhelm Leibniz Universität, Hannover, Tech. Rep., 2015.

[88] M. R. Vogt, H. Hahn, H. Holst, M. Winter, C. Schinke, M. Kontges, R. Brendel, and P. P. Altermatt, "Measurement of the Optical Constants of Soda-Lime Glasses in Dependence of Iron Content and Modeling of Iron-Related Power Losses in Crystalline Si Solar Cell Modules," *IEEE Journal of Photovoltaics*, vol. 6, no. 1, pp. 111–118, 1 2016.

[89] D. Zhang, I. Digdaya, R. Santbergen, R. van Swaaij, P. Bronsveld, M. Zeman, J. van Roosmalen, and A. Weeber, "Design and fabrication of a SiOx/ITO double-layer anti-reflective coating for heterojunction silicon solar cells," *Solar Energy Materials and Solar Cells*, vol. 117, pp. 132–138, 10 2013.

[90] P. B. Johnson and R. W. Christy, "Optical Constants of the Noble Metals," *Physical Review B*, vol. 6, no. 12, pp. 4370–4379, 12 1972.

[91] C. Monokroussos, Q. Gao, X. Zhang, E. Lee, Y. Wang, C. Zou, L. Rimmelspacher, J. B. Castro, M. Schweiger, and W. Herrmann, "Rear-side spectral irradiance at 1 sun and application to bifacial module power rating," *Progress in Photovoltaics: Research and Applications*, vol. 28, no. 8, pp. 755–766, 8 2020.

[92] H. Schulte-Huxel, R. Witteck, M. Ruben Vogt, F. Kiefer, S. Blankemeyer, M. R. Vogt, M. Köntges, R. Brendel, J. Krügener, and R. Peibst, "FLIP-FLOP CELL INTERCONNECTION ENABLED BY AN EXTREMELY HIGH BIFACIAL FACTOR OF SCREEN-PRINTED ION IMPLANTED N-PERT SI SOLAR CELLS," in *32nd European Photovoltaic Solar Energy Conference and Exhibition*, 2016, pp. 407–412. [Online]. Available: https://www.researchgate.net/publication/306038942

[93] J. Werner, G. Dubuis, A. Walter, P. Löper, S.-J. Moon, S. Nicolay, M. Morales-Masis, S. De Wolf, B. Niesen, and C. Ballif, "Sputtered rear electrode with broadband transparency for perovskite solar cells," *Solar Energy Materials and Solar Cells*, vol. 141, pp. 407–413, 10 2015.

[94] M. A. Green, "Self-consistent optical parameters of intrinsic silicon at 300 K including temperature coefficients," *Solar Energy Materials and Solar Cells*, vol. 92, no. 11, pp. 1305–1310, 2008.

[95] S. Manzoor, J. Häusele, K. A. Bush, A. F. Palmstrom, J. Carpenter, Z. J. Yu, S. F. Bent, M. D. Mcgehee, and Z. C. Holman, "Optical modeling of wide-bandgap perovskite and perovskite/silicon tandem solar cells using complex refractive indices for arbitrary-bandgap perovskite absorbers," *Optics Express*, vol. 26, no. 21, p. 27441, 10 2018.

[96] R. Santbergen, H. Uzu, K. Yamamoto, and M. Zeman, "Optimization of Three-Terminal Perovskite/Silicon Tandem Solar Cells," *IEEE Journal of Photovoltaics*, vol. 9, no. 2, pp. 446–451, 3 2019.

[97] M. Rienäcker, E. L. Warren, M. Schnabel, H. Schulte-Huxel, R. Niepelt, R. Brendel, P. Stradins, A. C. Tamboli, and R. Peibst, "Back-contacted bottom cells with three terminals: Maximizing power extraction from current-mismatched tandem cells," *Progress in Photovoltaics: Research and Applications*, vol. 27, no. 5, pp. 410–423, 5 2019.

[98] W. McMahon, H. Schulte-Huxel, J. Buencuerpo, J. Geisz, M. Young, T. Klein, A. Tamboli, and E. Warren, "Homogenous Voltage-Matched Strings Using Three-Terminal Tandem Solar Cells: Fundamentals and End Losses," *IEEE Journal of Photovoltaics*, vol. 11, no. 4, pp. 1078–1086, 7 2021.

[99] W.-J. Yin, T. Shi, and Y. Yan, "Unique Properties of Halide Perovskites as Possible Origins of the Superior Solar Cell Performance," *Advanced Materials*, vol. 26, no. 27, pp. 4653–4658, 7 2014.

[100] MathWorks, “vpasolve,” 2022. [Online]. Available: https://nl.mathworks.com/help/symbolic/sym.vpasolve.html

[101] C. A. Gueymard, “The SMARTS spectral irradiance model after 25 years: New developments and validation of reference spectra,” *Solar Energy*, vol. 187, pp. 233–253, 7 2019.

[102] R. Schmager, M. Langenhorst, J. Lehr, U. Lemmer, B. S. Richards, and U. W. Paetzold, “Methodology of energy yield modelling of perovskite-based multi-junction photovoltaics,” *Optics Express*, vol. 27, no. 8, p. A507, 4 2019.

[103] J. Remund, S. Müller, M. Schmutz, and P. Graf, “Meteonorm Software,” 9 2020.

[104] J. Ascencio-Vásquez, K. Brecl, and M. Topič, “Methodology of Köppen-Geiger-Photovoltaic climate classification and implications to worldwide mapping of PV system performance,” *Solar Energy*, vol. 191, pp. 672–685, 10 2019.

[105] M. C. Peel, B. L. Finlayson, and T. A. McMahon, “Updated world map of the Köppen-Geiger climate classification,” *Hydrology and Earth System Sciences*, vol. 11, no. 5, pp. 1633–1644, 10 2007.

[106] E. Aydin, T. G. Allen, M. De Bastiani, L. Xu, J. Ávila, M. Salvador, E. Van Kerschaver, and S. De Wolf, “Interplay between temperature and bandgap energies on the outdoor performance of perovskite/silicon tandem solar cells,” *Nature Energy*, vol. 5, no. 11, pp. 851–859, 11 2020.

[107] A. Meyer and H. Ade, “The effect of angle of incidence on the optical field distribution within thin film organic solar cells,” *Journal of Applied Physics*, vol. 106, no. 11, p. 113101, 12 2009.

[108] T.-S. Zhan, W.-M. Lin, M.-H. Tsai, and G.-S. Wang, “Design and Implementation of the Dual-Axis Solar Tracking System,” in *2013 IEEE 37th Annual Computer Software and Applications Conference*. IEEE, 7 2013, pp. 276–277.

[109] V. Sumathi, R. Jayapragash, A. Bakshi, and P. Kumar Akella, “Solar tracking methods to maximize PV system output – A review of the methods adopted in recent decade,” *Renewable and Sustainable Energy Reviews*, vol. 74, pp. 130–138, 7 2017.

[110] H. Teo, P. Lee, and M. Hawlader, “An active cooling system for photovoltaic modules,” *Applied Energy*, vol. 90, no. 1, pp. 309–315, 2 2012.

[111] A. Kane, V. Verma, and B. Singh, “Optimization of thermoelectric cooling technology for an active cooling of photovoltaic panel,” *Renewable and Sustainable Energy Reviews*, vol. 75, pp. 1295–1305, 8 2017.

[112] D. C. Nguyen, K. Sato, M. Hamada, F. Murata, and Y. Ishikawa, “Annual output energy harvested by building-integrated photovoltaics based on the optimized structure of 2-terminal perovskite/silicon tandem cells under realistic conditions,” *Solar Energy*, vol. 241, pp. 452–459, 7 2022.

[113] T. Du, W. Xu, S. Xu, S. R. Ratnasingham, C.-T. Lin, J. Kim, J. Briscoe, M. A. McLachlan, and J. R. Durrant, “Light-intensity and thickness dependent efficiency of planar perovskite solar cells: charge recombination versus extraction,” *Journal of Materials Chemistry C*, vol. 8, no. 36, pp. 12 648–12 655, 2020.

[114] T. Duong, Y. Wu, H. Shen, J. Peng, X. Fu, D. Jacobs, E.-C. Wang, T. C. Kho, K. C. Fong, M. Stocks, E. Franklin, A. Blakers, N. Zin, K. McIntosh, W. Li, Y.-B. Cheng, T. P. White, K. Weber, and K. Catchpole, “Rubidium Multication Perovskite with Optimized Bandgap for Perovskite-Silicon Tandem with over 26% Efficiency,” *Advanced Energy Materials*, vol. 7, no. 14, p. 1700228, 7 2017.

[115] A. P. Zoombelt, M. Fonrodona, M. M. Wienk, A. B. Sieval, J. C. Hummelen, and R. A. J. Janssen, “Photovoltaic Performance of an Ultrasmall Band Gap Polymer,” *Organic Letters*, vol. 11, no. 4, pp. 903–906, 2 2009.

[116] P. Ricchiazzi, S. Yang, C. Gautier, and D. Sowle, “SBDART: A Research and Teaching Software Tool for Plane-Parallel Radiative Transfer in the Earth’s Atmosphere,” *Bulletin of the American Meteorological Society*, vol. 79, no. 10, pp. 2101–2114, 10 1998.

[117] W. Raja, M. De Bastiani, T. G. Allen, E. Aydin, A. Razzaq, A. u. Rehman, E. Ugur, A. Babayigit, A. S. Subbiah, F. H. Isikgor, and S. De Wolf, “Photon recycling in perovskite solar cells and its impact on device design,” *Nanophotonics*, vol. 10, no. 8, pp. 2023–2042, 6 2021.

[118] F. Stern and J. M. Woodall, “Photon recycling in semiconductor lasers,” *Journal of Applied Physics*, vol. 45, no. 9, pp. 3904–3906, 9 1974.

[119] S. Durbin and J. Gray, “Numerical modeling of photon recycling in solar cells,” *IEEE Transactions on Electron Devices*, vol. 41, no. 2, pp. 239–245, 1994.

[120] P. J. Isherwood, I. R. Cole, A. Smith, and T. R. Betts, “The impact of spectral variation on the thermodynamic limits to photovoltaic energy conversion,” *Solar Energy*, vol. 221, pp. 131–139, 6 2021.

[121] H. Ziar, “Effect of thermal radiation entropy on the outdoor efficiency limit of single-junction silicon solar cells,” *Solar Energy Materials and Solar Cells*, vol. 242, p. 111763, 8 2022.

[122] A. Richter, S. W. Glunz, F. Werner, J. Schmidt, and A. Cuevas, “Improved quantitative description of Auger recombination in crystalline silicon,” *Physical Review B*, vol. 86, no. 16, p. 165202, 10 2012.

[123] C. M. Wolff, P. Caprioglio, M. Stolterfoht, and D. Neher, “Nonradiative Recombination in Perovskite Solar Cells: The Role of Interfaces,” *Advanced Materials*, vol. 31, no. 52, p. 1902762, 12 2019.

[124] E. W. Weisstein, “Heaviside Step Function,” 5 2022.

[125] C. W. Hansen and B. H. King, “Determining Series Resistance for Equivalent Circuit Models of a PV Module,” *IEEE Journal of Photovoltaics*, vol. 9, no. 2, pp. 538–543, 3 2019.

[126] D. Fébba, R. Rubinger, A. Oliveira, and E. Bortoni, “Impacts of temperature and irradiance on polycrystalline silicon solar cells parameters,” *Solar Energy*, vol. 174, pp. 628–639, 11 2018.